

Copyright
by
Minkyu Kim
2007

The Dissertation Committee for Minkyu Kim
certifies that this is the approved version of the following dissertation:

ECE Radiation Analysis of the Hall Thruster

Committee:

Gary A. Hallock, Supervisor

Edward J. Powers

Hao Ling

James C. Wiley

Perry Phillips

Boris Breizman

ECE Radiation Analysis of the Hall Thruster

by

Minkyu Kim, B.S., M.S.

DISSERTATION

Presented to the Faculty of the Graduate School of
The University of Texas at Austin
in Partial Fulfillment
of the Requirements
for the Degree of

DOCTOR OF PHILOSOPHY

THE UNIVERSITY OF TEXAS AT AUSTIN

December 2007

Dedicated to Jiyoung and Michelle Bokyoung.

Acknowledgments

I would like to thank my supervisor, Professor Gary A. Hallock. He gave me the opportunity to work on a wide range of very interesting topics and guided me over the last five years.

I am also grateful for the help of the other members of my committee, Professor Edward J. Powers, Professor ao Ling, Dr. James C. Wiley, Dr. Perry Phillips and Dr. Boris Breizman. This work would not make progress without their insight and comments.

I would also like to thank Dr Robert E. Hebner. He introduced me to a very interesting topic, dielectric breakdown in liquids. His experience, insight and enthusiasm are still shaping me. My friends Alvaro Garcia, Charles Lee and Theresa Cailouet made my life more interesting. They always tried to help me and wanted to share my good and bad stories.

Most of all, my deepest gratitude goes to my wife Jiyoung and my daughter Michelle Bokyoung. I could not even start this study without Jiyoung's dedicated support, and Michelle let me know what is the most important thing in my life. Both of them are also the reasons that I am.

ECE Radiation Analysis of the Hall Thruster

Publication No. _____

Minkyu Kim, Ph.D.

The University of Texas at Austin, 2007

Supervisor: Gary A. Hallock

In this study, we developed three computational techniques for the ECE radiation analysis of the Hall thruster.

The first one is the single particle approximation analysis. This is the simplest one among the approaches. We modeled the plasma region of the Hall thruster with three parameters, the magnetic field, electron temperature, and electron density distributions. These parameters are constant in a cell. We calculated the radiation with the parameter distributions according to the observation angle. The frequency of a cell is determined by the magnetic field of the cell. This analysis is easy to approach and does not require a high computing performance. However, the results of this analysis don't have detail results. The radiated electric field is derived from the power, so there is no polarization information on the electric field. We moved on more sophisticated analysis.

The next one is the Particle-In-Cell (PIC) analysis. PIC is for analysis of microscopic phenomena. Particle motions in the thruster channel region

is simulated with the PIC method. We selected electrons from the Maxwell-Boltzmann distribution for the speed of electrons. The Monte Carlo method was adopted in this selection. We solved the Lorentz force equation to get the motion data of the electrons and analyzed the radiated electric field with the particle motions. Then, we took the Fourier transform of the electric field to consider the radiation in the frequency domain. This approach is from definition, the radiation is from charge acceleration. It is more realistic approach to the plasma. It uses same parameter distributions, but the parameters in a cell is not constant any more because of adopting the Monte Carlo method. It also shows the polarization information of the radiation. However, we assume in this analysis that the radiation is in free space. The channel plasma is considered as current sources for radiation. The material constants of the plasma is concerned as free space.

The last approach adopted is to consider the non free space and inhomogeneous media. The hybrid FEM/MoM (hybrid element method) was suggested to exploit advantages of finite element method (FEM) and method of moment (MoM), the representative methods for the radiation analysis, and to compensate their disadvantages. The hybrid element method was introduced to analyze the ECE radiation by using EMAP5. In this analysis, the plasma was considered as dielectrics, and the source currents were from the plasma parameters.

Table of Contents

Acknowledgments	v
Abstract	vi
List of Tables	xii
List of Figures	xiii
Chapter 1. Introduction	1
1.1 Electric Propulsion System	3
1.1.1 Resistojet	6
1.1.2 Arcjet	7
1.1.3 Ion Thruster	7
1.1.4 Field Emission Electric Propulsion	9
1.1.5 Electromagnetic Propulsion	10
1.2 Hall Thrusters	11
1.2.1 SPT Series	13
1.2.2 BPT-4000	14
1.2.3 BHT-200	14
1.2.4 SMART-1 Mission	15
1.3 Motivation	16
Chapter 2. Theory	21
2.1 Particle Motion In Fields	21
2.1.1 Constant Electric Field	21
2.1.2 Constant Magnetic Field	22
2.1.3 $\vec{E} \times \vec{B}$ Drifts	23
2.1.4 ∇B Drifts	25

2.2	Electron Cyclotron Emission	27
2.2.1	Electron Cyclotron Emission in a Static Magnetic Field	27
2.2.2	Radiation by Nonrelativistic Electron	30
2.2.3	Radiation of an Accelerated Charge	33
2.2.4	Optical Depth	35
2.3	Dielectric Constant of a plasma	37
2.3.1	DC Conductivity	37
2.3.1.1	Isotropic Plasma	37
2.3.1.2	Anisotropic Magnetoplasma	38
2.3.2	AC Conductivity	40
2.3.3	The Plasma as a Dielectric Medium	41
Chapter 3.	Numerical Method	43
3.1	Plasma Parameter Modeling for BPT-4000 class Hall thrusters	44
3.1.1	1D Modeling	44
3.1.2	2D Modeling	49
3.1.3	Magnetic Field Model	49
3.1.4	Electron Temperature Model	51
3.1.5	Electron Density Model	54
3.2	Plasma Parameters for SPT100 class Hall thrusters	57
3.2.1	Electron Density and Electron Temperature	57
3.2.2	Magnetic Field	59
3.3	The Monte Carlo Method	61
3.3.1	Numerical Applications	63
3.4	Particle-In-Cell	70
3.4.1	Selecting Electrons	70
3.4.1.1	Maxwell-Boltzmann Distribution of Speed	70
3.4.1.2	Isotropic Velocity	71
3.4.2	Time Scale	73
3.4.2.1	Fourier Transform Point of view	73
3.4.2.2	Magnetic field Point of view	74
3.4.3	Collision Frequency	74

3.5	Numerical Modeling of Electromagnetic Radiation	79
3.5.1	Hybrid Element Method	79
3.5.2	Near & Far Fields	80
Chapter 4.	Code Validation	81
4.1	Particle-In-Cell Analysis	82
4.1.1	Constant Magnetic Field	82
4.1.2	$\vec{E} \times \vec{B}$ Drifts	84
4.1.3	∇B Drifts	85
4.2	Hybrid Moment Method	92
4.2.1	Two Dipoles	92
4.2.2	Modified Length of Infinitesimal Dipoles	95
Chapter 5.	Results	99
5.1	Single Particle Approximation Results	102
5.1.1	BPT-4000 Class	103
5.1.1.1	1D Results	103
5.1.1.2	2D Results	106
5.1.1.3	Comparison to Experiment	110
5.1.2	SPT100 Class	115
5.1.2.1	2D Results	115
5.1.2.2	Comparison to Experiment	117
5.2	Particle-In-Cell Results	121
5.2.1	BPT-4000 Class	122
5.2.1.1	Numerical Analysis Results	122
5.2.1.2	Comparison to Experiment	122
5.2.2	SPT100 Class	128
5.2.2.1	Numerical Analysis Results	128
5.2.2.2	Comparison to Experiment	131
5.3	Hybrid Element Method Results	138
5.3.1	BPT-4000 Class	140
5.3.1.1	Numerical Analysis Results	141

5.3.1.2	Comparison to Experiment	142
5.3.2	SPT100 Class	144
5.3.2.1	Numerical Analysis Results	145
5.3.2.2	Comparison to Experiment	146
Chapter 6.	Discussion	149
6.1	Comparison of Results	149
6.1.1	BPT-4000 Class	149
6.1.2	SPT100 Class	152
6.2	Differences between Numerical Results and Experiments	156
6.3	Comparison of Three Numerical Approaches	157
6.4	Harmonics	159
Chapter 7.	Conclusion and Suggested Future Works	161
7.1	Conclusion	161
7.2	Future Work	164
	Appendices	165
Appendix A.	Fourier Transform	166
A.1	Continuous-Time time Fourier Series	166
A.2	Continuous-Time Fourier Transform	167
A.3	Discrete-Time Fourier Transform	167
Appendix B.	The Monte Carlo Method	170
B.1	Random Variables	171
B.2	Probability Density Function	172
B.3	Cumulative Distribution Function	173
B.4	Transformation of PDFs	173
B.5	Sampling Using Inversion of the CDF	175
Appendix C.	Equivalence / Huygens' Principle	176
	Bibliography	179
	Vita	191

List of Tables

1.1	Thrust systems and their specific impulse [75]	11
1.2	SPT specifications	14
4.1	Lamor radius [mm] (from Figure 4.1 / analytic)	82
5.1	Plasma parameter distributions for the hybrid element method analysis.	140
5.2	Plasma parameter distributions for the hybrid element method analysis.	144

List of Figures

1.1	The Hall thruster diagram [9]. 1) Magnetic system; 2) insulator; 3) anode; 4) cathode; 5) gas inlet.	12
1.2	The PPS-1350 thruster [62]	16
1.3	Emission spectrum of experimental measurement in [43].	17
1.4	Electric field emission measurement for SPT-140 at 4.5 kW [30].	18
1.5	Emission from the SPT-140 operating at 300 V [66].	19
1.6	Emission spectrum in [16].	20
2.1	Drift of a particle in a nonuniform magnetic field [20].	27
2.2	Radiation scheme.	34
3.1	Hall thruster model	45
3.2	Radial magnetic flux density [T] along the normalized z axis for the 1D model.	46
3.3	Electron temperature [eV] along the normalized z axis for the 1D model.	47
3.4	Electron density [$\# / m^3$] along the normalized z axis for the 1D model.	48
3.5	The measurements of the magnetic field from a) [69] and b) [60].	50
3.6	a) Magnetic field profiles of the model. b) The magnitude of magnetic field distribution of the model.	52
3.7	Electron temperature measurement from a) [9] and b) [29].	53
3.8	Electron temperature [eV] profiles of the model.	54
3.9	Electron density measurement from a) [9] and b) [29].	55
3.10	The electron density [$\# / m^3$] profiles of the model	56
3.11	Electron density distributions.	57
3.12	Electron temperature distributions.	58
3.13	Electron temperature distribution a) from [9] b) from [21] c) reconstructed.	58
3.14	Contour plot of magnetic field a) from [9] b) from [60]	60

3.15	Radial magnetic field distribution at the center line a) from [9] b) from [11].	60
3.16	a) Generated field contour and b) radial field distributions at center lines in magnetic field modeling for PIC	62
3.17	Monte Carlo on the normal distribution. The graphs in the left column are PDFs and in the right column are CDFs.	66
3.18	Monte Carlo on the log normal distribution. The graphs in the left column are PDFs and in the right column are CDFs. . . .	67
3.19	Monte Carlo on the exponential distribution. The graphs in the left column are PDFs and in the right column are CDFs. . . .	68
3.20	Monte Carlo on the Maxwell-Boltzmann distribution of speeds. The graphs in the left column are PDFs and in the right column are CDFs.	69
3.21	Isotropic velocity on the unit sphere from 3.23. a) top view b) side view	72
3.22	Isotropic velocity on the unit sphere from 3.24. a) top view b) side view	72
3.23	Cross section of Xe for high-energy region. Dababneh [72, 73], Register [79], Nickel [36], Wagenaar [80], and Ramsauer 23 [63]	76
3.24	Cross section of Xe for low-energy region. Hunter [18], Koizumi [70], McEachran [52], Sinfailam [71], and Ramsauer 29 [64] . .	77
3.25	Collision frequency of Xe Dababneh [72, 73], Register [79], Nickel [36], Wagenaar [80], Ramsauer 23 [63], Hunter [18], Koizumi [70], McEachran [52] Sinfailam [71], and Ramsauer 29 [64] . .	78
4.1	Gyration motions in magnetic fields. \square is analytic results. a) $B = 100$ G and $T_e = 1$ eV b) $B = 100$ G and $T_e = 10$ eV c) B $= 500$ G and $T_e = 1$ eV d) $B = 500$ G and $T_e = 10$ eV e) $B =$ 1550 G and $T_e = 1$ eV f) $B = 1550$ G and $T_e = 10$ eV	83
4.2	$\vec{E} \times \vec{B}$ drifts. a) $B = 100$ G and $E = 1$ kV/m b) $B = 100$ G and $E = 10$ kV/m c) $B = 500$ G and $E = 1$ kV/m d) $B = 500$ G and $E = 10$ kV/m e) $B = 1550$ G and $E = 1$ kV/m f) $B =$ 1550 G and $E = 10$ kV/m	86
4.3	∇B drift with the electric field of 10 kV/m and the magnetic field $\vec{B} = 100G \cdot 35/r\hat{r}$. a) 4 eV b) 8 eV c) 12 eV	89
4.4	∇B drift with the electric field of 10 kV/m and the magnetic field $\vec{B} = 500G \cdot 35/r\hat{r}$. a) 4 eV b) 8 eV c) 12 eV	90

4.5	∇B drift with the electric field of 10 kV/m and the magnetic field $\vec{B} = 1550G \cdot 35/r\hat{r}$. a) 4 eV b) 8 eV c) 12 eV	91
4.6	Radiation pattern of electric field a) from the linear sum of 2 dipoles b) from 2 dipoles with 90° phase difference.	93
4.7	Radiation pattern of electric fields in the polar coordinates, $E_\phi(+)$ and $E_\theta(\times)$, a) from the linear sum of 2 dipoles b) from 2 dipoles with 90° phase difference.	94
4.8	Radiation pattern of power from 2 dipoles.	95
4.9	Radiation patterns of a dipole with original length and current (+), fixed length of 1 mm and compromised current (\times), and analytic calculation (-). a) $f = 0.28$ GHz, $l = 0.68$ mm b) $f = 0.28$ GHz, $l = 2.4$ mm c) $f = 1.4$ GHz, $l = 128 \mu\text{m}$ d) $f = 1.4$ GHz, $l = 472 \mu\text{m}$ e) $f = 5.6$ GHz, $l = 34 \mu\text{m}$ f) $f = 5.6$ GHz, $l = 108 \mu\text{m}$	97
4.10	Radiation patterns with two dipoles. The currents are a) x - 1 A, y - 0 A, $\phi = 0^\circ$ b) x - 0.866 A, y - 0.5 A, $\phi = 30^\circ$ c) x - 0.5 A, y - 0.866 A, $\phi = 60^\circ$ d) x - 0 A, y - 1 A, $\phi = 90^\circ$	98
5.1	Hall Thruster computation configuration.	103
5.2	Hall Thruster 1D computation configuration.	104
5.3	Power per steradian as a function of angle calculated from thruster axis in the 1D model (all frequencies).	105
5.4	Electric field as a function of frequency in the 1D model.	106
5.5	Hall Thruster 2D computation configuration.	107
5.6	Power per steradian as a function of angle calculated from thruster axis in the 2D model of the BPT-4000 class Hall thruster (all frequencies).	108
5.7	Electric field as a function of frequency in the 2D model of the BPT-4000 class Hall thruster.	109
5.8	Vertically polarized emission spectrum from ref. [43]	111
5.9	Horizontally polarized emission spectrum from ref. [43]	111
5.10	Comparison of the simulation result ($\theta = 0^\circ$) to the measured data with background (vertical polarization).	112
5.11	Comparison of the simulation result ($\theta = 0^\circ$) to the measured data with background (horizontal polarization).	113
5.12	Comparison of the simulation result ($\theta = 0^\circ$) to the measured data with background subtracted (vertical polarization).	114

5.13	Comparison of the simulation result ($\theta = 0^\circ$) to the measured data with background subtracted (horizontal polarization). . .	114
5.14	Power per steradian as a function of angle calculated from thruster axis in the 2D model of the SPT100 class Hall thruster (all frequencies).	115
5.15	Electric field as a function of frequency in the 2D model of the SPT100 class Hall thruster.	116
5.16	Emission spectrum from ref. [16]	117
5.17	Measurement comparison over age and production variation [16]	118
5.18	Comparison of the simulation result ($\theta = 0^\circ$) to the measured data with background.	119
5.19	Comparison of the simulation result ($\theta = 0^\circ$) to the measured data with background subtracted (vertical polarization). . . .	120
5.20	Comparison of the simulation result ($\theta = 0^\circ$) to the measured data with background subtracted (horizontal polarization). . .	120
5.21	Electric field as a function of frequency at the observation point (PIC analysis with the BPT-4000 class Hall thruster).	123
5.22	Comparison of the PIC analysis result with the BPT-4000 class Hall thruster to the measured data (vertical polarization). . .	124
5.23	Comparison of the PIC analysis result with the BPT-4000 class Hall thruster to the measured data (horizontal polarization). .	125
5.24	Radiation from each fourth of the Hall thruster (vertical polarization of the BPT-4000 class Hall thruster).	126
5.25	Radiation from each fourth of the Hall thruster (horizontal polarization of the BPT-4000 class Hall thruster).	127
5.26	Radiation from each 1/8 of the Hall thruster (vertical polarization of the BPT-4000 class Hall thruster).	129
5.27	Radiation from each 1/8 of the Hall thruster (horizontal polarization of the BPT-4000 class Hall thruster).	130
5.28	Electric field as a function of frequency at the observation point (experimental data of the SPT100 class Hallthrusters from literature).	131
5.29	Comparison of the PIC result to the SPT100 measurement data.	132
5.30	Comparison of the PIC result of SPT100 to the BPT-4000 measured data (vertical polarization).	133
5.31	Comparison of the PIC result of SPT100 to the BPT-4000 measured data (horizontal polarization).	134

5.32	Radiation from each fourth of the Hall thruster (vertical polarization of the SPT100 class Hall thruster).	136
5.33	Radiation from each fourth of the Hall thruster (horizontal polarization of the SPT100 class Hall thruster).	137
5.34	Configuration for the hybrid element analysis. a) front view b) side view	139
5.35	Electric field as a function of frequency of the hybrid element method analysis with the 2D magnetic field.	141
5.36	Comparison of the 2D hybrid element analysis result using the 2D magnetic field distribution to the experimental data (vertical polarization).	143
5.37	Comparison of the 2D hybrid element analysis result using the 2D magnetic field distribution to the experimental data (horizontal polarization).	143
5.38	Electric field as a function of frequency of the hybrid element method analysis with the 2D magnetic field.	145
5.39	Comparison of the SPT100 hybrid element analysis result using the 2D magnetic field distribution to the experimental data.	147
5.40	Comparison of the SPT100 hybrid element analysis result using the 2D magnetic field distribution to the BPT-4000 measured data (vertical polarization).	148
5.41	Comparison of the SPT100 hybrid element analysis result using the 2D magnetic field distribution to the BPT-4000 measured data (horizontal polarization).	148
6.1	Comparison of the BPT-4000 experimental data to all three approaches: the single particle approximation analysis (SPA), the particle-in-cell analysis (PIC) and the hybrid element analysis (HEA). (vertical polarization).	150
6.2	Comparison of the BPT-4000 experimental data to all three approaches: the single particle approximation analysis (SPA), the particle-in-cell analysis (PIC) and the hybrid element analysis (HEA). (horizontal polarization).	150
6.3	Comparison of the SPT100 experimental data to all three approaches: the single particle approximation analysis (SPA), the particle-in-cell analysis (PIC) and the hybrid element analysis (HEA). (vertical polarization).	152
6.4	Comparison of the SPT100 experimental data to all three approaches: the single particle approximation analysis (SPA), the particle-in-cell analysis (PIC) and the hybrid element analysis (HEA). (horizontal polarization).	153

6.5	Comparison of the BPT-4000 experimental data to all three approaches: the single particle approximation analysis (SPA), the particle-in-cell analysis (PIC) and the hybrid element analysis (HEA). (vertical polarization).	154
6.6	Comparison of the BPT-4000 experimental data to all three approaches: the single particle approximation analysis (SPA), the particle-in-cell analysis (PIC) and the hybrid element analysis (HEA). (horizontal polarization).	155
6.7	The spectrum of cyclotron radiation be a nearly nonrelativistic electron ($\beta_{\parallel}=0.1$) [6].	160
C.1	a) Actual and b) equivalent problem models [4].	178

Chapter 1

Introduction

The subject of this thesis is a numerical analysis of electron cyclotron emission (ECE) radiation from a Hall thruster. The radiation is analyzed by using three approaches: the single particle approximation analysis, the Particle-In-Cell/Monte Carlo analysis, and the hybrid element method analysis.

The first one is the single particle approximation analysis. This is the simplest one among the approaches. We divide the plasma in the Hall thruster channel region into small dices, called cells, and model it with three parameters, the magnetic field, electron temperature, and electron density distributions. These parameters are constant in a cell. We plug the parameter distributions into a formula of the ECE radiation and calculate the radiation according to the observation angle. The frequency of a cell is determined by the magnetic field of the cell. This analysis is easy to approach and does not require a high computing performance. However, the results of this analysis are not highly detailed. The formula used in this analysis is radiated power per steradian. The radiated electric field is derived from the power, so there is no polarization information on the electric field.

The next one is the Particle-In-Cell/Monte carlo (PIC/MC) analysis. PIC is for analysis of microscopic phenomena. Particle motions in the thruster channel region are simulated with the PIC method. We select electrons from the Maxwell-Boltzmann distribution for the speed of electrons. The Monte Carlo method is adopted in this selection. We launch the selected electrons in the channel region and solve the Lorentz force equation to get the motion data of the electrons. The radiated electric field is analyzed from the particle motions. Then, we take the Fourier transform of the electric field to see the radiation in the frequency domain. This is a fundamental approach as the radiation is from charge acceleration. It is more realistic approach to the plasma. It uses the same parameter distributions, but the parameters in a cell are not constant any more because of adopting the Monte Carlo method. It also gives the polarization information of the radiation. However, we assume in this analysis that the radiation is in free space. The channel plasma is considered as current sources for radiation. The material constants of the plasma is assumed as free space.

Plasmas in Hall thrusters are generally not well modeled as free space. The last approach adopted is to consider the non free space and inhomogeneous media. General numerical methods for the electromagnetic emission analysis are finite element method (FEM) and method of moment (MoM). These methods have their own advantages and disadvantages. FEM is more accurate especially for near fields, and can analyze inhomogeneous media. However, according to the increasing of the number of elements, the computational burden is

significantly increasing. If the target volume is increased in 3D analysis, it gets severely worse. MoM is basically a 3D analysis method. Increasing distance from observation points does not affect the computation burden. However, it is hard to analyze scattering problems with inhomogeneous media. To exploit their advantages and to compensate their disadvantages, hybrid FEM/MoM (hybrid element method) was suggested [34, 39, 47, 88]. A new approach of ECE analysis with the hybrid element method is introduced. In this analysis, the plasma is considered as dielectrics, and the source currents are from the plasma parameters.

We compare the results of all approaches each other and also compare the numerical results to experimental data [43].

This work can be extended to predict the effect of the plume on the various subsystems and mitigate risk associated with the introduction of the Hall thruster.

1.1 Electric Propulsion System

More than three hundred electric propulsion thrusters have flown on over 100 spacecraft over the last thirty five years and a significant increase in usage is expected over the next decade. The 1990s have been described as the ‘era of application [27]’ because the benefits of electric propulsion are being realized on numerous commercial satellite missions and there has been an increase in flight activity for a broad spectrum of electric propulsion devices. Advancements in electric propulsion related technologies and thruster design

improvements, based on extensive ground and flight test results, have brought some electric propulsion devices to a high level of technological maturity. The risk of employing electric thrusters on spacecraft has diminished in recent years due to an increase in the number of successful electric thruster missions, improvements in thruster materials and designs, and an improved understanding of fundamental thruster operating principles and spacecraft integration issues.

With the increasing emphasis on lowering the mass of spacecraft propulsion systems, increasing spacecraft orbiting lifetimes, and reducing overall costs, together with greater amounts of electric power now available on-board spacecraft, the applications for electric propulsion systems will certainly continue to grow. Electric propulsion technology has matured to a point where its expanded use for select space missions is justified from both a technological and an economic standpoint.

Electric thrusters can outperform conventional chemical (liquid and solid propellant) propulsion systems for certain space missions because of their generally higher specific impulse values. For select missions, replacing current chemical propulsion systems with high performance electric propulsion systems can provide substantial mass and cost savings, increased orbiting lifetimes, and increased mission capabilities.

The current and likely near-term electric thruster missions include station keeping, drag compensation, attitude control, station repositioning, orbit raising or lowering, orbit repositioning, and maneuvering of interplanetary spacecraft [49].

Electric propulsion is the acceleration of propellant gases by any of electrical heating, electric or magnetic, or both of field forces to provide propulsive thrust to a vehicle. It involves the conversion of electrical energy into kinetic energy of the exhaust gases. There are numerous electric propulsion devices described in the literature, which can be grouped into at least one of three fundamental categories.

- Electrothermal Propulsion - the propellant is heated using electrical energy, and the hot propellant gas is then thermodynamically expanded and accelerated through an exhaust nozzle, e.g. resistojets and arcjet thrusters.
- Electrostatic Propulsion - the propellant atoms are ionized and accelerated out of the thruster by electrostatic field forces. The exhausted propellant ions are neutralized by electrons emitted from an external cathode, e.g. ion thruster and field emission electric propulsion thruster
- Electromagnetic Propulsion - the propellant is ionized and accelerated by the combined interaction of electric and magnetic field forces on the resultant propellant plasma, e.g. Hall thruster, pulsed plasma thruster, and magnetoplasmadynamic thrusters

New electric propulsion technologies designed to operate at higher power (5 – 50 kW) for future long range planetary exploration and large velocity change maneuvers are under study. This effort has in part been a response

to NASA's Project Prometheus [42], a technology program to develop safe, efficient high power sources for solar system exploration. In primary propulsion on microspacecraft or fine position control of conventional spacecraft has driven the interest in subkilowatt thrusters [10].

1.1.1 Resistojet

A resistojet is a device that heats a propellant stream by passing it through an ohmically heated chamber before the propellant is expanded through a downstream nozzle. In resistojets, the propellant is fed into the thruster and heated while flowing over an immersed resistance heater or over thruster chamber surfaces heated by radiation from an isolated resistance heater [27, 38].

Resistojets (MR-501, MR-502A, HiPEHT, etc.) have accumulated a substantial flight history onboard at least 75 spacecraft since 1965 [27], mainly performing north-south station keeping (NSSK) and some attitude control, east-west station keeping (EWSK), on-orbit maneuvering, and limited on-orbit boosting. Future resistojet missions include station keeping, orbit insertion, and de-orbit functions. Resistojets have been used on Lockheed Martin Astro Space (LMAS) Series 4000 and 5000 satellites and recently on Iridium satellites.

1.1.2 Arcjet

An arcjet is a device that heats a propellant stream by passing a high current electrical arc through it, before the propellant is expanded through a downstream nozzle [38]. In arcjets, an electrical arc discharge is initiated between a central cathode and a coaxial anode, which also acts as the thruster's nozzle. The propellant is fed into the thruster and heated while flowing through and around the arc discharge.

A research group from the Kharkov Aviation Institute (KhAI), which was established with Russian industrial companies and still keeps working relations with them, has presented an analytical study of gas acceleration in the supersonic nozzle of the arcjet thruster [68]. The heat transfer in supersonic flow under electrical discharge results in significant displacement of the critical throat comparing with classic adiabatic flow. Key parameters like an expansion angle and throat position were presented as functions of arc parameters.

Since 1993, arcjets (MR-508, MR-509, and MR-510) have been used for NSSK on at least six LMAS Series 7000 and A-2100 satellites and are baselined for several future satellites. In 1997-1998, arcjets were used on both an experimental USAF orbit raising mission (26-kW ESEX arcjet) and an orbit insertion/maintenance mission (ATOS arcjet).

1.1.3 Ion Thruster

An ion thruster is a device that accelerates propellant ions by an electrostatic field [38]. In ion thrusters, neutral propellant atoms are fed into a

discharge chamber and ionized by bombardment with electrons emitted from a cathode in a low voltage electrical discharge.

Since 1962, ion thrusters have flown on about eleven experimental spacecraft. Several ion thrusters (XIPS-13, XIPS-25, IES, and UK-10) and a radiofrequency ion thruster (RIT-10) were launched to provide NSSK for several operational satellites. Hughes used their XIPS-13 ion thruster on HS-601, PAS-5, and Galaxt 8-i satellites and their XIPS-25 ion thruster on HS-702 and Galaxy 10 satellites [27, 49].

Keldysh Research Center presented results of numerical simulation of a low-power Xe-ion thruster with an advanced, slit-type accelerating system. Experiments were carried out for the power range of 50-150 W and specific impulse values of 2500 – 3500 s were achieved. Highest values of thruster efficiency were about 65 % [68].

The NSTAR electron bombardment ion thruster was provided primary propulsion for the Deep Space-1 spacecraft on the first flight of NASA's New Millennium program in 1998. The success of the Deep Space 1 technology demonstration has led to the planned use of three NSTAR ion thrusters for the DAWN mission to explore Ceres and Vesta, two protoplanets between the orbits of Mars and Jupiter [10]. DAWN, rescheduled for launch in September 2007, would be the first NASA space science mission to implement electric propulsion. Boeing Electron Dynamics Division (EDD) is developing the 30 cm ion thrusters for this Discovery-class mission. The NSTAR thruster extended life test ended this year after more than 30,300 hr of operation, having

processed over 230 kg of xenon. The NSTAR program far exceeded its original goals of 8,000 hr of operation with a total xenon throughput of 83 kg.

The NASA Evolutionary Xenon Thruster (NEXT) is designed to deliver a throttleable 7 kW, 40 cm ion thruster with a xenon throughput capability of over 400 kg, a specific impulse (I_{sp}) of 2,200 – 4,120 sec, and a thrust of 50 – 210 mN. Two NASA-led teams continued work toward the development of a long-life engine system for power levels greater than 20 kW and I_{sp} in the 6,000-8,000-sec range. The High Power Ion Propulsion team, led by NASA-Glenn is developing an 8,000 sec, 25 kW gridded ion thruster using a microwave ionization source and neutralizer in a rectangular geometry. The JPL-led team is developing the nuclear electric xenon ion system, which will include advanced carbon-carbon grids and a reservoir hollow cathode, in an effort to develop a 20 kW, 7,500 sec I_{sp} thruster with high propellant throughput capability.

On January 31, 2003, ESA's latest telecommunication technology demonstration satellite, Artemis, reached its assigned geostationary orbit after an 18 month transfer. The spacecraft had used its experimental ion propulsion system, consisting of two RIT-10 and T5 thrusters, to complete the maneuver.

1.1.4 Field Emission Electric Propulsion

In field emission electric propulsion (FEEP) thrusters, the liquid propellant is fed to the tip of a needle-like emitter and intense local electric fields cause charged liquid droplets to spontaneously form. The charged liquid droplets are extracted away from the liquid surface and accelerated by the

electrostatic fields.

1.1.5 Electromagnetic Propulsion

A magneto plasma dynamic thruster is a device that accelerates a propellant plasma by an internal or external magnetic field acting on an internal arc current [38].

Magneto plasma dynamic (MPD) thrusters frequently use similar electrode geometries as arcjets and also use an electrical arc discharge. However, the majority of thrust generated in MPDTs is due to electromagnetic forces exerted on the propellant plasma by interaction with the arc and the self-induced magnetic field.

In pulsed plasma, a portion of the propellant feedstock (typically solid Teflon) is ablated and ionized by an electrical arc discharge sheet initiated between two electrodes by a discharging capacitor. The resultant propellant plasma is accelerated by interaction with the arc and the self-induced magnetic field.

Table 1.1: Thrust systems and their specific impulse [75]

Engine	Effective Exhaust Velocity (m/s)	I_{sp} (s)	Thrust (N)	Duration
Solid rocket	1,000 - 4,000	100	$10^3 - 10^7$	minutes
Resistojet rocket	2,000 - 6,000		$10^{-2} - 10$	minutes
Arcjet rocket	4,000 - 12,000		$10^{-2} - 10$	minutes
Hall thruster	8,000 - 50,000	1,500	$10^{-3} - 10$	months
Ion thruster	15,000 - 80,000	5,000	$10^{-3} - 10$	months
VASIMR	10,000 - 300,000	30,000	40 - 1,200	days - months

1.2 Hall Thrusters

The Hall thruster is a plasma propulsion device designed in the 1960s. The inventor is A. I. Morozov. They are mostly known as electric propulsion thrusters for spacecraft, and are also called stationary plasma thrusters (SPTs). The advantages of the Hall thruster are higher thrust densities and specific impulses between 1 and 2000 sec. These advantages promise to increase operating lifetime and payload mass. Because of these advantages, the Hall thrusters are considered ideal for many on-orbit applications including station keeping, orbit re-phasing, and orbit transfer of geosynchronous communication satellites.

It has become clear that the physical processes in the Hall thrusters are extremely complicated, despite the simple construction of the devices. The discharge in the Hall thrusters is unlike any other known discharge. It is characterized by the spatial separation of the ionization and acceleration zones.

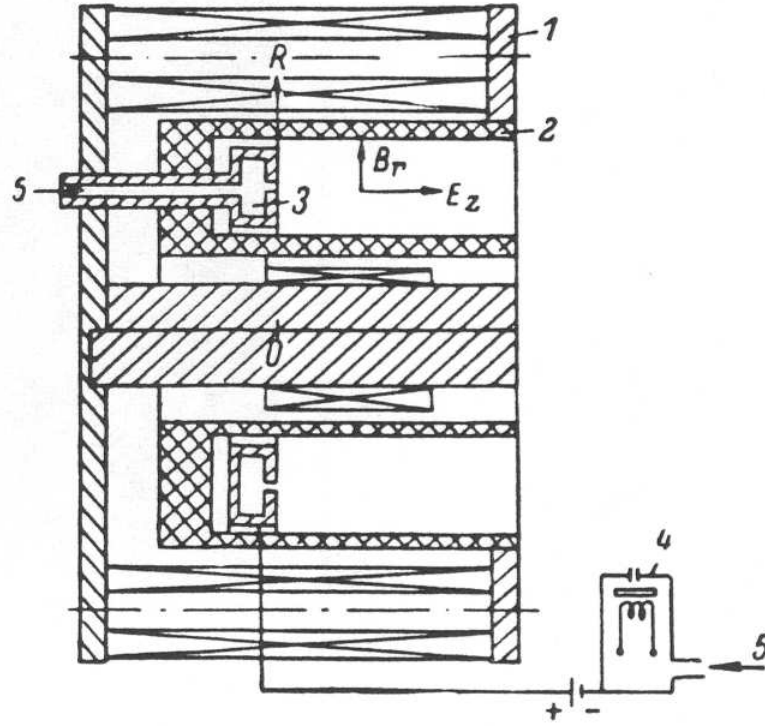


Figure 1.1: The Hall thruster diagram [9]. 1) Magnetic system; 2) insulator; 3) anode; 4) cathode; 5) gas inlet.

In the ionization zone, crossed electric and magnetic fields are present with the radial directional magnetic field crossing the wall while the axial directional electric field is tangential to them. A free path length of charged particles much higher than the size of system, and the drift of electrons is closed.

Electrons emitted from an external hollow cathode are hindered from directly reaching the anode by the radial magnetic field increasing to the outlet of thruster and become magnetized and confined in an azimuthal $\vec{E} \times \vec{B}$ drift

motion. The neutral propellant atoms are fed into the discharge chamber and ionized by bombardment with the electrons. The radial magnetic field is not strong enough to make the ions magnetized, because the Larmor radius of the ions is much bigger than the thruster size. The ions are accelerated axially by the electric field, and the thrust is produced by momentum imparted to the ions. Plasma is created with a very high electron temperature of up to 20 eV within the discharge [55].

1.2.1 SPT Series

Hall thrusters (SPT-50, SPT-70, SPT-100, etc.) have an extensive flight history on-board Russian spacecraft for NSSK, EWSK, attitude control, orbit injection and repositioning applications on more than 50 Russian satellite since 1971 [27, 55]. Hall thrusters have continued to accumulate flight time on Russian satellites. Since 1994, more than eight geostationary satellites equipped with SPT-100-type thrusters have been launched. The total number of SPT-100 thrusters operated onboard these satellites is more than 64. The maximum operation time on a single SPT-100 has exceeded 1,500 hr (on Express 11). Stationary plasma thrusters (SPT) were developed and qualified at DB Fakel. Main functional specifications of SPT thrusters are listed in Table 1.2.

Table 1.2: SPT specifications

	Thrust mN	Power kW	I_{sp} sec	Efficiency %	Life time hrs
SPT-35 ^a	1 - 10	0.2	1100	35	2000
SPT-50 ^a	20	0.35	1250	35	2250
SPT-70 ^a	40	0.65	1450	48	3100
SPT-100 ^a	83	1.35	1550	52	8000
SPT-140 ^b	290	4.5	1800	51	7000
PPS-1350 ^c	92	1.5	1800	52	8000

^a [68], ^b [12], ^c [5]

1.2.2 BPT-4000

The Aerojet BPT-4000 Hall thruster underwent qualification tests [31, 43, 46, 83]. Thruster performance was verified for multimode operation at 3.0 and 4.5 kW (high thrust mode at a discharge voltage of 300 V and high I_{sp} mode at 400 V). The target performance ranges for the thruster are I_{sp} of 1,844 – 2,076 sec and thrust of 168 – 294 mN [10]. The flight qualification test program, including an approximately 6,000-hr life test, was completed by the end of 2004.

1.2.3 BHT-200

The BHT-200 Hall thruster [19, 40, 41, 50, 59] originally developed for the TechSat 21 mission by Busek, is undergoing life tests at the Air Force Research Lab. NASA-Glenn and Aerojet were selected to begin the Hi-Voltage Hall Accelerator program to develop a Hall thruster targeting the 6 – 8 kW power, 2,200 – 2,800 sec I_{sp} performance range. Preliminary testing of the

NASA-457M Hall thruster operating on xenon propellant at power levels up to 96 kW demonstrated thrust, I_{sp} , and efficiency of 3.3 N, 3,500 sec, and 58%, respectively.

1.2.4 SMART-1 Mission

In September 2003, ESA launched its SMART-1 mission to explore the Moon. SMART stands for Small Missions for Advanced Research in Technology. SMART-1 is the first European spacecraft to travel to and orbit around the Moon. It travelled to the Moon using solar-electric propulsion with the PPS-1350 Hall thrusters developed at Snecma and carrying a battery of miniaturized instruments. Figure 1.2 shows PPS-1350. Its use of solar electric propulsion as its primary drive mechanism will be a first for Europe and is essential in paving the way for future ESA projects with large velocity requirements, such as the Mercury Cornerstone mission [82]. As well as testing new technology, SMART-1 is making the first comprehensive inventory of key chemical elements in the lunar surface [74].



Figure 1.2: The PPS-1350 thruster [62]

1.3 Motivation

Former investigators have carried out detailed measurements and indicated that oscillations play a major part in the closed-drift accelerators with an extended acceleration zone (CDAE) [69], and verified that high-frequency (up to 20 MHz) azimuthal waves (electron drift waves) are excited in a Hall-current plasma accelerator [26]. Two instabilities, an ionization instability and a transit-time instability have been found [77], and the relationship between the amplitude and spectrum of the high-frequency waves (20 - 400 MHz) on the discharge have been revealed [76].

In 2003, measurements of radiated electric fields from 10 kHz to 18 GHz on a BPT-4000 Hall thruster being qualified for flight identified many types of emission, including strong electromagnetic emission in the 1-5 GHz range [43].

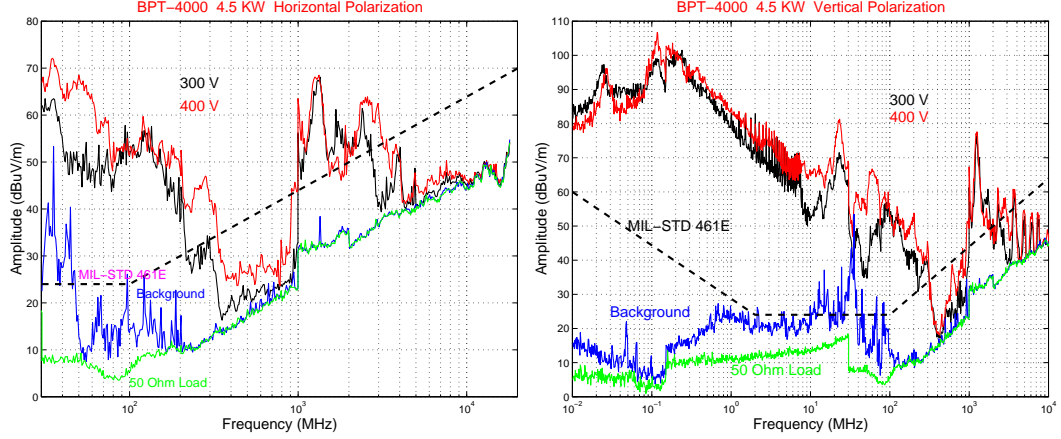


Figure 1.3: Emission spectrum of experimental measurement in [43].

The spectrum of the emission is shown in Figure 1.3. The frequency is similar to satellite communication frequencies (1-20 GHz), so it is of significant concern. The BPT-4000 is a 4.5 kW class thruster. The BPT-4000 Hall thrusters were tested to see the effect of a plasma plume on reflector antennas [46, 83]. The purpose of this test was to gain quantitative information on the effects of the thruster on various spacecraft subsystems and to help mitigate the risk associated with the introduction of this new propulsion technology on future spacecraft. Several broad harmonic peaks have been observed as one can see in Figure 1.3 [43]. These emissions are more than 20 dB above MIL-STD 461E, and 40 dB above spacecraft designers limits. MIL-STD 416E is the requirements of the United States department of defense [1]. The requirements are for the control of electromagnetic interference characteristics of subsystems and equipment.

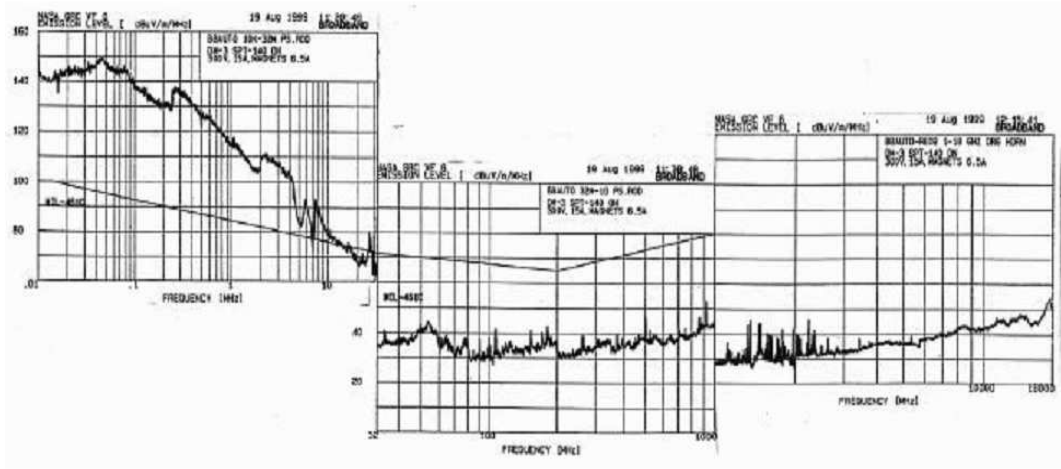


Figure 1.4: Electric field emission measurement for SPT-140 at 4.5 kW [30].

Ground tests of SPT-140 Hall thrusters were presented in [30, 66]. The SPT-140 is a 4.5 kW class thruster, which is similar to BPT-4000. Performances of the thruster are 1800 sec of I_{sp} , 51% of overall system efficiency, and 7200 hrs of lifetime. EMI tests found very little emission in the traditional RF communication bands [30], and the emission of the tests is shown in Figure 1.4. At the lowest frequencies (10 kHz to 20 MHz), E-field emission exceeded the MIL-STD-461C specification by up to 53 dB. The SPT-140 was found to emit aperiodic broadband emissions at levels above the detection threshold from 1 to 3 GHz.

An engineering model SPT-140 Hall thruster was evaluated with respect to thrust and radiated electromagnetic interference [66], shown in Figure 1.5. The broadband electromagnetic emission spectra generated by the engine was measured for a range of frequencies from 10kHz to 18 GHz. These results were

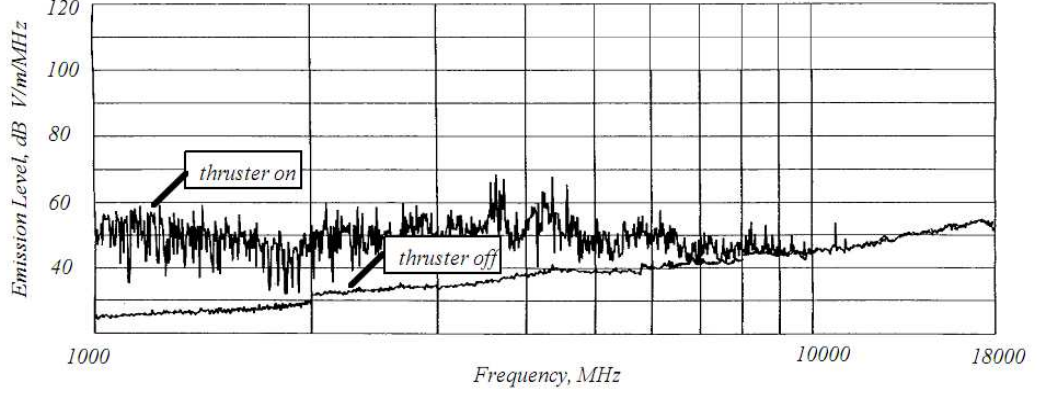


Figure 1.5: Emission from the SPT-140 operating at 300 V [66].

also compared to the noise threshold of the measurement system and MIL-STD-461C. The emissions at frequencies above 100 MHz were below MIL-STD-461C and approached the minimum detectable values at frequencies in excess of 1000 MHz. The different trend from the work at Beiting et al [43] was shown in the above two measurements, which demonstrates consistency.

Another intensive measurement of emission is reported [16]. Space Systems/Loral (SS/L) characterized the emissions of SPT-100 thrusters developed by Design Bureau Fakel, and the are shown in Figure 1.6. The parameters characterized include emissions polarization, directivity, magnitude, burstiness, and coherency. In this paper, strong radiation was shown again in high frequency range (1 – 7 GHz). About 30 dB higher emission was shown at the peak around 1.4 – 2 GHz. This trend is similar to the trend of BPT-4000.

To confirm that the measured radiation is indeed ECE, a simple 2D model was developed for the radiation of a Hall thruster [32]. The analysis

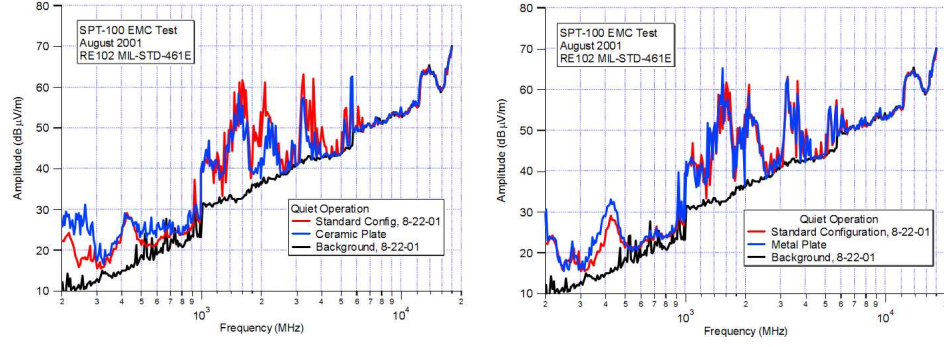


Figure 1.6: Emission spectrum in [16].

of ECE radiation is performed with the magnetic field, plasma density, and plasma electron temperature distributions in a typical Hall thruster. Parameters for the models were obtained from the literature [21, 65].

Chapter 2

Theory

2.1 Particle Motion In Fields

The equations of motion for a particle acted on by electric and magnetic fields are

$$\vec{F} = m \frac{d\vec{v}}{dt} = q[\vec{E}(\vec{r}, t) + \vec{v} \times \vec{B}(\vec{r}, t)] \quad (2.1)$$

$$\frac{d\vec{r}}{dt} = \vec{v}(t) \quad (2.2)$$

where (2.1) is the Lorentz force equation. These equations cannot be solved for the general case where the force is a nonlinear function of \vec{r} , but solutions for various special cases can be found [44].

2.1.1 Constant Electric Field

For a constant electric field $\vec{E} = \vec{E}_0$ with $\vec{B} \equiv 0$, the particle moves with a constant acceleration along \vec{E}_0

$$\vec{F} = m \frac{d\vec{v}}{dt} = q\vec{E}(\vec{r}, t) \quad (2.3)$$

Therefore, the particle position is given by

$$\vec{r}(t) = \vec{r}_0 + \vec{v}_0 t + \frac{1}{2} \vec{a}_0 t^2 \quad (2.4)$$

where \vec{r}_0 and \vec{v}_0 are the particle position and velocity at $t = 0$ and $a_0 = q\vec{E}_0/m$ [44].

2.1.2 Constant Magnetic Field

For a constant magnetic field $\vec{B} = \hat{z}B_0$ with $\vec{E} = 0$, (2.1) can be written [20]

$$F_x = m \frac{dv_x}{dt} = qv_y B_0 \quad (2.5)$$

$$F_y = m \frac{dv_y}{dt} = -qv_x B_0 \quad (2.6)$$

$$F_z = m \frac{dv_z}{dt} = 0 \quad (2.7)$$

The z motion is decoupled from x and y motion. With the other two equations (2.5) and (2.6), we obtain

$$\frac{d^2 v_x}{dt^2} = -\omega_c^2 v_x \quad (2.8)$$

where

$$\omega_c = e \frac{B_0}{m} \quad (2.9)$$

is the gyration frequency or cyclotron frequency. Solving (2.8) and using (2.5), we find

$$v_x = v_{\perp 0} \cos(\omega_c t + \phi_0) \quad (2.10)$$

$$v_y = -v_{\perp 0} \sin(\omega_c t + \phi_0) \quad (2.11)$$

$$v_z = v_{z0} \quad (2.12)$$

where $v_{\perp 0}$ is the speed perpendicular to B_0 and ϕ is an arbitrary phase. Integrating yields the particle position

$$x = r_c \sin(\omega_c t + \phi_0) + (x_0 - r_c \sin \phi_0) \quad (2.13)$$

$$y = r_c \cos(\omega_c t + \phi_0) + (y_0 - r_c \cos \phi_0) \quad (2.14)$$

$$z = z_0 + v_{z0} t \quad (2.15)$$

r_c is the gyration radius, which is called the Lamor radius. The Lamor radius is given by

$$\begin{aligned} r_c &= v_{\perp 0} / \omega_c \\ &= \frac{v_{\perp 0} m}{q B_0} \end{aligned} \quad (2.16)$$

Equations (2.10) to (2.15) show that the particle moves in a circular orbit perpendicular to B having frequency ω_c and radius r_c . We can understand the motion by equating the inward Lorentz force to the outward centrifugal force

$$| q v_{\perp 0} B_0 | = \frac{m v_{\perp 0}^2}{r_c} \quad (2.17)$$

2.1.3 $\vec{E} \times \vec{B}$ Drifts

We take $\vec{B} = \hat{z} B_0$ and $\vec{E} = \hat{y} E_{\perp 0} + \hat{z} E_{z0}$. Letting $\vec{v} = \hat{z} v_z(t) + \vec{v}_{\perp}(t)$, we obtain the equation for the transverse motion [20, 44]

$$\vec{F} = m \frac{d\vec{v}_{\perp}}{dt} = q(\hat{y} E_{\perp 0} + \vec{v}_{\perp} \times \hat{z} B_0) \quad (2.18)$$

We let $\vec{v}_\perp(t) = \vec{v}_E + \vec{v}_c(t)$ where \vec{v}_E and $\vec{v}_c(t)$ are a constant velocity and a cyclotron velocity, respectively. Using this,

$$\vec{F} = m \frac{d\vec{v}_c}{dt} = q(\hat{y}E_{\perp 0} + \vec{v}_E \times \hat{z}B_0 + \vec{v}_c \times \hat{z}B_0) \quad (2.19)$$

$[\vec{E} + \vec{v} \times \vec{B}]_\perp = 0$, since $m d\vec{v}_c/dt$ gives only the circular motion at ω_c . Then

$$[\vec{E} + \vec{v} \times \vec{B}]_\perp \times \vec{B} = \vec{E} \times \vec{B} + (\vec{v} \cdot \vec{B})\vec{B} - B^2\vec{v} = 0 \quad (2.20)$$

From (2.20) and (2.19) the drift velocity in the electric and magnetic fields,

$$\vec{v}_E = \frac{\hat{y}E_{\perp 0} \times \hat{z}B_0}{B_0^2} \quad (2.21)$$

can be generalized to

$$\vec{v}_{gc} = \frac{\vec{E} \times \vec{B}}{B^2} = \frac{1}{q} \frac{\vec{F} \times \vec{B}}{B^2} \quad (2.22)$$

because $\hat{y}E_{\perp 0} \times \vec{B} \equiv 0$. \vec{v}_{gc} is the guiding center drift velocity. From (2.20) and (2.19) we also find

$$\vec{F} = m \frac{d\vec{v}_c}{dt} = q\vec{v}_c \times \hat{z}B_0 \quad (2.23)$$

We have seen that the solution of (2.23) is particle gyration at frequency ω_c with gyration radius r_c . Hence the transverse motion is the sum of a guiding center drift v_E and a gyration motion

$$\vec{v}_\perp(t) = \vec{v}_E + Re(v_{c0} e^{j\omega_c t}) \quad (2.24)$$

We note from (2.21) that \vec{v}_E is perpendicular to both \vec{E} and \vec{B} and is independent of the mass and charge of the particles. Therefore electrons and ions

drift with the same speed in the same direction. Integrating (2.24) with initial position $\vec{r}_{\perp 0}$, we obtain

$$\vec{r}_{\perp}(t) = \vec{r}_{\perp 0} + \vec{v}_E t + Re \left(\frac{1}{j\omega_c} v_{c0} e^{j\omega_c t} \right) \quad (2.25)$$

for the particle position.

2.1.4 ∇B Drifts

Assume the magnetic field lines are straight, in the z direction, but their density increases in the y direction. This configuration is shown in Fig. 2.1. The gradient in $|B|$ causes the Lamor radius to be larger at the bottom of the orbit than at the top. This leads to a drift, in opposite directions for ions and electrons, perpendicular to both \vec{B} and ∇B [20]. The drift velocity is proportional to r_c/L and v_{\perp} , where L is the scale length. Consider the Lorentz force (2.1), averaged over a gyration. Since the particle spends as much time moving up as down F_x is clearly equal to 0. We will calculate F_y , in an approximate way, by using the undisturbed orbit given by (2.10)-(2.12), and (2.13)-(2.15) for a uniform magnetic field. We make a Taylor expansion of the magnetic field about the point $x_0 = 0, y_0 = 0$.

$$\begin{aligned} \vec{B} &= \vec{B}_0 + (\vec{r} \cdot \nabla) \vec{B} + \dots \\ B_z &= B_0 + y(\partial B_z / \partial y) + \dots \end{aligned} \quad (2.26)$$

This expansion requires $r_c/L \ll 1$, where L is the scale length of

$\partial B_z / \partial y$. Taking (2.10) and (2.26), we have

$$\begin{aligned}
F_y &= -qv_\perp B_z(y) \\
&= -qv_\perp \cos(\omega_c t) \left[B_0 \pm r_c \cos(\omega_c t) \frac{\partial B}{\partial y} \right] \\
&= -qv_\perp \left[B_0 \cos(\omega_c t) \pm r_c \cos^2(\omega_c t) \frac{\partial B}{\partial y} \right]
\end{aligned} \tag{2.27}$$

Using a standard trigonometric identity, $\cos^2(\omega) = \frac{1}{2}\{1 + \cos(2\omega)\}$, (2.27) can be rewritten as

$$F_y = -qv_\perp \left[\pm \frac{1}{2} r_c \frac{\partial B}{\partial y} + B_0 \cos(\omega_c t) \pm \frac{1}{2} r_c \cos(2\omega_c t) \frac{\partial B}{\partial y} \right] \tag{2.28}$$

The third term on the right hand side in (2.28) indicates that the second harmonics can be produced by a gradient of the magnetic field. From this, we can expect that a complicated magnetic field can produce harmonics. The first term of (2.27) averages to zero over a gyration, and the time average of $\cos^2(\omega_c t)$ is 1/2, so that

$$\langle F_y \rangle = \mp qv_\perp r_c \frac{1}{2} \frac{\partial B}{\partial y} \tag{2.29}$$

where $\langle F \rangle$ is the time average force. The guiding center drift velocity (2.22) is then

$$v_{gc} = \frac{1}{q} \frac{\vec{F} \times \vec{B}}{B^2} = \frac{1}{q} \frac{\langle F_y \rangle}{|B|} \hat{x} = \mp \frac{v_\perp r_c}{B} \frac{1}{2} \frac{\partial B}{\partial y} \hat{x} \tag{2.30}$$

Equation (2.30) can be generalized to

$$v_{\nabla B} = \pm \frac{1}{2} v_\perp r_c \frac{\vec{B} \times \nabla B}{B^2} \tag{2.31}$$

$v_{\nabla B}$ is called the “grad-B drift”.

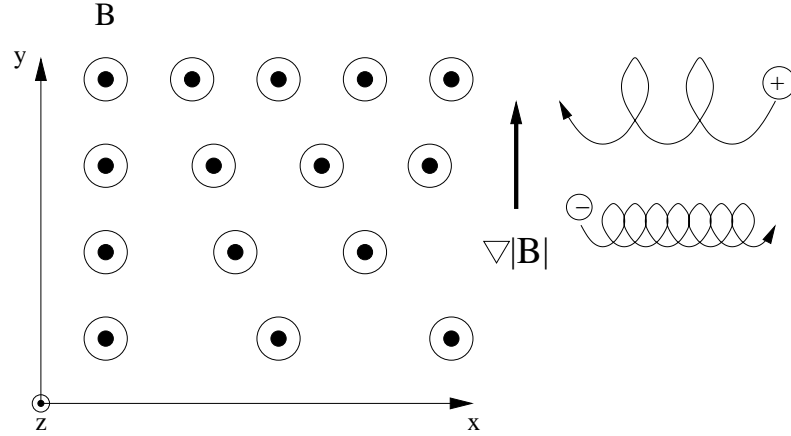


Figure 2.1: Drift of a particle in a nonuniform magnetic field [20].

2.2 Electron Cyclotron Emission

A plasma immersed in a magnetic field radiates as the result of the acceleration of the charges in their orbit motions around the magnetic lines of force. The frequency and angular distribution of the radiation undergoes dramatic changes as the electron energy is increased from nonrelativistic to extreme relativistic energies [6].

2.2.1 Electron Cyclotron Emission in a Static Magnetic Field

The equation of motion of a particle of charge e and mass m in a uniform static magnetic field B_0 is

$$\frac{dP}{dt} = e(v \times B_0) \quad (2.32)$$

where

$$P = \frac{\varepsilon}{c^2} v \quad (2.33)$$

$$\varepsilon = \frac{m_0 c^2}{\sqrt{1 - \beta^2}} \equiv \gamma m_0 c^2 \quad (2.34)$$

$$\beta^2 = \left(\frac{v_{\parallel}}{c}\right)^2 + \left(\frac{v_{\perp}}{c}\right)^2 \quad (2.35)$$

$$\gamma = (1 - \beta^2)^{-1/2} \quad (2.36)$$

P is the particle momentum, and v_{\parallel} and v_{\perp} are the instantaneous particle velocities along and perpendicular to B_0 . Although the particle radiates, the energy loss per cycle is so small that the energy ε can be taken as constant [6]. The solution of (2.32) for the particle velocity v and displacement ρ gives

$$v = \hat{x} v_{\perp} \cos \omega_0 t + \hat{y} v_{\perp} \sin \omega_0 t + \hat{z} v_{\parallel} \quad (2.37)$$

$$\rho = \hat{x} \frac{v_{\perp}}{\omega_0} \sin \omega_0 t - \hat{y} \frac{v_{\perp}}{\omega_0} \cos \omega_0 t + \hat{z} v_{\parallel} t \quad (2.38)$$

where

$$\omega_0 = \left| \frac{e B_0}{m_0} \right| \sqrt{1 - \beta^2}, \quad \omega_b = \left| \frac{e B_0}{m_0} \right|$$

ω_0 , the cyclotron frequency, takes account of the relativistic mass change, and ω_b is its value in the limit of zero particle speed. In the zero particle speed case, we can get the equations (2.37) and (2.38) from the equations (2.10), (2.11) and (2.12) and from (2.13), (2.14) and (2.15) with $q = -e$ and $\phi = 0$.

The energy $W(\omega, \Omega)$ emitted per unit solid angle per frequency interval $d\omega$ is given by [6]

$$W(\omega, \Omega) = \frac{e^2 \omega^2}{16 \pi^3 \varepsilon_0 c^3} \left| \int_{-\infty}^{\infty} e^{-j\omega(t' - \hat{q} \cdot \rho / c)} [\hat{q} \times (\hat{q} \times v)] dt' \right|^2 \quad (2.39)$$

To evaluate the exponent appearing in the equation we assume that the particle propagation vector lies in the $x - z$ plane. Thus

$$\hat{q} = \hat{x} \sin \theta + \hat{y}(0) + \hat{z} \cos \theta \quad (2.40)$$

This leads the integral part of (2.39) to the form

$$\int_{-\infty}^{\infty} \{1; \sin \omega_0 t; \cos \omega_0 t\} \exp [j(x \sin \omega_0 t + \omega t \beta_{\parallel} \cos \theta - \omega t)] dt \quad (2.41)$$

whose solution is, respectively,

$$2\pi \sum_{m=-\infty}^{\infty} \left[J_m(x); -j \frac{dJ_m(x)}{dx}; \frac{1 - \beta_{\parallel} \cos \theta}{\beta_{\perp} \sin \theta} J_m(x) \right] \delta(y) \quad (2.42)$$

where $\delta(y)$ is the Dirac delta function, and the arguments of the Bessel function and the δ function are given by

$$x = \frac{\omega}{\omega_0} \beta_{\perp} \sin \theta \quad (2.43)$$

$$y = m\omega_0 - \omega(1 - \beta_{\parallel} \cos \theta) \quad (2.44)$$

Because of the $\delta(y)$, $y = 0$, from (2.44) the radiation spectrum consists of spectral lines occurring at frequencies

$$\omega = \frac{m\omega_0}{1 - \beta_{\parallel} \cos \theta} = \frac{m\omega_b \sqrt{1 - \beta_{\parallel}^2 - \beta_{\perp}^2}}{1 - \beta_{\parallel} \cos \theta} \quad (2.45)$$

The emitted power η is found by dividing W by the total time of radiation given by $2\pi \delta(y)$.

$$\eta = \frac{W}{2\pi \delta(y)} \quad (2.46)$$

The quantity obtained is the coefficient of spontaneous emission η_ω . Taking the magnitude gives [6]

$$\eta_\omega(\omega, v, \theta) = \frac{e^2 \omega^2}{8\pi^2 \varepsilon_0 c} \left[\sum_{m=1}^{\infty} \left(\frac{\cos \theta - \beta_{\parallel}}{\sin \theta} \right)^2 J_m^2(x) + \beta_{\perp}^2 J_m'^2(x) \right] \delta(y) \quad (2.47)$$

where $J_m' \equiv dJ_m(x)/dx$.

The total radiation in a given harmonic m is obtained by integrating a single term of the right-hand side of (2.47) over frequency ω and solid angle $d\Omega = 2\pi \sin \theta d\theta$. The result is

$$\eta_m^T = \frac{e^2 \omega_b^2}{2\pi \varepsilon_0 c} \frac{1 - \beta_0^2}{\beta_0} \left[m \beta_0^2 J_{2m}'(2m\beta_0) - m^2 (1 - \beta_0^2) \int_0^{\beta_0} J_{2m}(2mt) dt \right] \quad (2.48)$$

where $\beta_0 \equiv \beta_{\perp} / \sqrt{1 - \beta_{\perp}^2}$

The total power radiated over all harmonics is obtained by summing (2.48) over all m 's:

$$\eta^T = \frac{e^2 \omega_b^2}{6\pi \varepsilon_0 c^3} \frac{v_{\perp}^2}{1 - \beta^2} = \frac{e^2 \omega_b^2}{6\pi \varepsilon_0 c^3} \left[(1 - \beta_{\parallel}^2) \left(\frac{\varepsilon}{m_0 c^2} \right)^2 - 1 \right] \quad (2.49)$$

2.2.2 Radiation by Nonrelativistic Electron

When the energy of an electron is such that $m\beta \ll 1$ ($m = 1, 2, \dots$, and $\beta = v/c$), the Bessel functions can be replaced by their asymptotic series expansions for small arguments. Thus, (2.48) for $\beta_{\parallel} = 0$, $m\beta \ll 1$, and $1 - \beta^2 \rightarrow 1$ is

$$\eta_m^T = \frac{e^2 \omega_b^2}{2\pi \varepsilon_0 c} \frac{(m+1)(m^{2m+1})}{(2m+1)!} \beta^{2m} \quad (2.50)$$

From this we see that the spectrum consists of a series of discrete lines of rapidly decreasing intensity ($\eta_m^T / \eta_{m+1}^T \sim 1/\beta^2 = (c/v)^2$).

For electron energies equal or less than 250 eV, $\beta^2 \leq 10^{-3}$ and emission at any but the fundamental frequency $m = 1$ can be neglected. In this case the differential emissivity given by (2.47) reduces to

$$\eta_\omega(\theta) = \frac{e^2 \omega^2}{32\pi^2 \varepsilon_0 c^3} v_\perp^2 (1 + \cos^2 \theta) \delta[\omega_b - \omega(1 - \beta_\parallel \cos \theta)] \quad (2.51)$$

The equation indicates that twice as much radiation is emitted per unit solid angle along the direction of the magnetic field ($\theta = 0$) as perpendicular to it.

We have considered periodic motions of the charge extending over infinite time and radiating infinitely long wave trains. This gave rise to infinitely narrow spectral lines. Collisions of the radiating charges with other species give the spectral lines a finite width. To calculate the line shape and width we assume that a particle radiates unhindered during a finite time interval. It stops abruptly at the end of this interval and then starts radiating once more, and the probability of occurrence of the interval is a Gaussian. For low collision frequencies $\nu(v) \ll \omega$ the only modification is to replace the δ function in (2.51) by

$$\frac{1}{\pi} \frac{\nu(v)}{[\omega_b - \omega(1 - \beta_\parallel \cos \theta)]^2 + \nu^2(v)} \quad (2.52)$$

so that

$$\eta_\omega(\theta) = \frac{e^2 \omega^2}{32\pi^3 \varepsilon_0 c^3} \frac{\nu(v)}{[\omega_b - \omega(1 - \beta_\parallel \cos \theta)]^2 + \nu^2(v)} \quad (2.53)$$

where $\nu(v)$ is the collision frequency. The line shape of the differential emissivity with respect to frequency is Lorentzian with respect to frequency. Neglecting bremsstrahlung is justified near the line center in which cyclotron emission predominates.

The emission coefficient j_ω is obtained by summing η_ω over the distribution of particle velocities. Here we consider a Maxwellian distribution. In a collisionless plasma, use of (2.51) yields

$$j_\omega = \frac{\omega_p^2 \omega^2}{16\pi^2 \sqrt{\pi} c^3} (mv_0^2)(1 + \cos^2 \theta) \frac{1}{\Delta} e^{-(\omega - \omega_b)^2 / \Delta^2} \quad (2.54)$$

where $v_0^2 = kT/m$ and $\Delta = \sqrt{2}(v_0/c) \omega \cos \theta$. If we do not consider the line broadening and $\omega = \omega_b$, then use of (2.54) gives [33]

$$j_\omega = \frac{\omega_p^2 \omega_b^2}{16\pi^2 c} \left(\frac{kT}{c^2} \right) (1 + \cos^2 \theta) \quad [\text{W/steradian}] \quad (2.55)$$

When collisions are the dominant broadening mechanism, and ν is constant, the use of (2.53) with $\beta_\parallel \cos \theta \rightarrow 0$ gives

$$\begin{aligned} j_\omega &= \frac{\omega_p^2 \omega^2}{6\pi^3 \sqrt{\pi} c^3} (mv_0^2)(1 + \cos^2 \theta) \int_0^\infty \frac{\nu(ay)}{(\omega - \omega_b)^2 + \nu^2(ay)} e^{-y^2} y^4 dy \\ &= \frac{\omega_p^2 \omega^2}{16\pi^3 c^3} (mv_0^2)(1 + \cos^2 \theta) \frac{\nu}{(\omega - \omega_b)^2 + \nu^2} \end{aligned} \quad (2.56)$$

where the $a = \sqrt{2} v_0$. When ν is independent of speed, the line has a Lorentzian shape and the line width at the half-power points is, $\Delta_\nu = 2\nu$. If we keep Doppler and collisional effects, $\beta_\parallel \cos \theta \neq 0$ leads to an integral. The Doppler line shape dominates near the center and the Lorentz line shape dominates in the wings.

In thermal equilibrium the emission can not exceed black-body radiation. The peak intensity is independent of the electron temperature. The intensity emitted in the backward direction is almost the same as that in the forward direction. The radiation is distributed over wide angular cones.

2.2.3 Radiation of an Accelerated Charge

Consider a charge e in vacuum whose instantaneous position $P'(t')$ is given by the vector $\vec{\rho}(t')$ and whose instantaneous velocity is $\vec{v}(t')$ [6]. In Fig. 2.2, t' is the time at which the signal propagated at velocity c is emitted at $P'(t')$ to arrive at the position of the observer $P(t)$ at a time t . The “retarded” time t' is related to t through

$$t' = t - \frac{R(t')}{c} \quad (2.57)$$

where $R(t')$ is the distance between e and the observer. The retarded values of the velocity and acceleration of the charge are

$$-\vec{v} = \frac{d(\hat{q}R)}{dt'} \quad (2.58)$$

$$-\dot{\vec{v}} = \frac{d^2(\hat{q}R)}{dt'^2} \quad (2.59)$$

where $\hat{q} = \vec{R}/R$ is the unit vector directed from P' to P .

The electric and magnetic fields at $P(\vec{r}, t)$,

$$\vec{E}(\vec{r}, t) = -\nabla\phi(\vec{r}, t) - \frac{\partial\vec{A}(\vec{r}, t)}{\partial t} \quad (2.60)$$

$$\vec{B}(\vec{r}, t) = \nabla \times \vec{A}(\vec{r}, t) \quad (2.61)$$

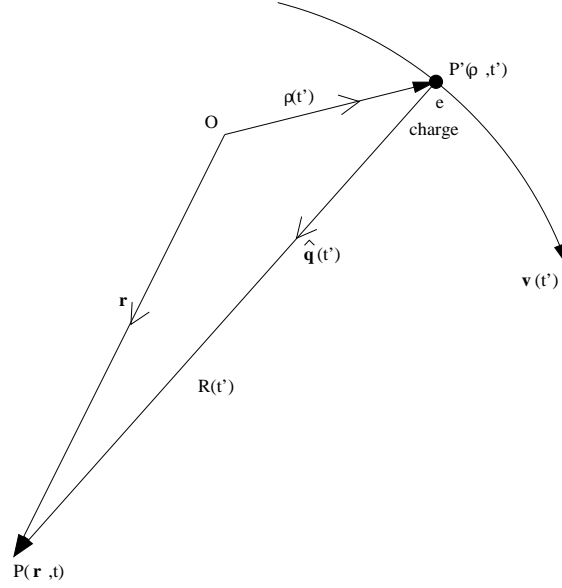


Figure 2.2: Radiation scheme.

are deduced from the Liénard-Wiechert potential [58],

$$\phi(\vec{r}, t) = \frac{e}{4\pi\epsilon_0} \left[\frac{1}{g R} \right]_{t'} \quad (2.62)$$

$$\vec{A}(\vec{r}, t) = \frac{e}{4\pi\epsilon_0 c} \left[\frac{\vec{\beta}}{g R} \right]_{t'} \quad (2.63)$$

where $\vec{\beta} = \vec{v}/c$, $g = (1 - \hat{q} \cdot \vec{\beta})$, and $[\]_{t'}$, denotes that the quantity within the brackets is to be evaluated at the retarded time t' defined by (2.57). After substituting (2.62) and (2.63) into (2.60) and (2.61) and some tedious transformations, we find that

$$\vec{E}(\vec{r}, t) = \frac{e}{4\pi\epsilon_0} \left[\frac{(1 - \beta^2)(\hat{q} - \vec{\beta})}{g^3 R^2} + \frac{\hat{q} \times \{(\hat{q} - \vec{\beta}) \times \dot{\vec{\beta}}\}}{g^3 c R} \right]_{t'} \quad (2.64)$$

$$\vec{B} = \frac{1}{c} \hat{q} \times \vec{E} \quad (2.65)$$

For nonrelativistic motions, g goes to 1, and (2.64) yields

$$\vec{E}(\vec{r}, t) = \frac{e}{4\pi\epsilon_0} \left[\frac{\hat{q}}{R^2} + \frac{\hat{q} \times (\hat{q} \times \dot{\vec{v}})}{c^2 R} \right] \quad (2.66)$$

where \vec{B} has the same form as (2.65).

The first term of (2.66) represents the near static field of the moving charge and is independent of its acceleration. The second term represents the “radiation” field, in which \vec{E} and \vec{B} vary linearly with $\dot{\vec{\beta}}$. The fields exhibit the typical $1/R$ fall-off with distance, and are orthogonal to the radius vector. The observation point is assumed to be far away from the charge, so that \hat{q} and R change negligibly during a small acceleration interval [33].

2.2.4 Optical Depth

Consider a plasma sphere of radius a . The larger the a , the larger the reabsorption, until a point is reached at which the volume emission is just balanced by the black-body radiation from the surface. If we equate two equations we find that [6]

$$a \approx 1.2 \times 10^{33} \frac{T^{7/2}}{n_e n_i Z^2 \overline{G}} \quad (2.67)$$

Thus for a plasma with $T = 1.16 \times 10^5 \text{ } ^\circ K = 10 \text{ eV}$, $n_e = 10^{12} \text{ cm}^{-3}$, $Z = 1$, $\overline{G} = 2\sqrt{3}/\pi$, $a \approx 5 \times 10^{16} \text{ cm}$

Note that the quantity $1/a$ defines an effective absorption coefficient α_{eff} . For a plasma of characteristic size L the dimensionless parameter

$$\tau_0 \equiv \alpha_{eff} L = \frac{1}{a} L \quad (2.68)$$

If we assume L is 2 cm, then τ_0 is 4×10^{-17} .

The emission at a given frequency has three characteristic regimes, depending on the value of τ_0 [6]. When $\tau_0 \ll 1$, the radiation seen by the observer suffers negligible self-absorption in its passage through the medium, and the observer sees essentially the contribution from each individual volume element along the ray, that is, the intensity $I_\omega = \int j_\omega ds$. The medium is said to be optically transparent to the radiation. When $\tau_0 \gg 1$, the intensity is a direct measure of the source function. The medium is said to be opaque to the radiation. If, at the same time, the medium is in thermal equilibrium, the medium is said to emit as a black body. Finally, when τ_0 is neither very small nor very large compared with unity, the medium is said to be semitransparent or gray.

Therefore, plasmas in this study are said to be optically transparent or optically thin. Reabsorption or self-absorption is negligible.

2.3 Dielectric Constant of a plasma

A very simple form of the equation of motion for a weakly ionized cold plasma, known as the Langevin equation, is introduced. In a weakly ionized plasma the number density of the charged particles is much smaller than that of the neutral particles. In this case, the charge – neutral interactions are dominant. The equation of motion for an average electron can be written as

$$m_e \frac{\partial \vec{v}_e}{\partial t} = -e(\vec{E} + \vec{v}_e \times \vec{B}) + \vec{F}_{coll} \quad (2.69)$$

where $\vec{F}_{coll} = -\nu_c m_e \vec{v}_e$.

Therefore, the Langevin equation is given by

$$m_e \frac{\partial \vec{v}_e}{\partial t} = -e(\vec{E} + \vec{v}_e \times \vec{B}) - \nu_c m_e \vec{v}_e \quad (2.70)$$

2.3.1 DC Conductivity

The steady state Langevin equation is applied to derive an expression for the DC conductivity of a weakly ionized homogeneous plasma for which the Lorentz model (electron gas) is applicable. The applied \vec{E} is assumed to be constant and uniform.

2.3.1.1 Isotropic Plasma

If there is no magnetic field, then the steady state Langevin equation for electrons becomes

$$0 = -e\vec{E} - \nu_c m_e \vec{v}_e \quad (2.71)$$

The action of the applied electric field is balanced dynamically by the electron-neutral collisions. The electron current density is

$$\vec{J} = -e n_e \vec{v}_e = \left(\frac{n_e e^2}{m_e \nu_c} \right) \vec{E} \quad (2.72)$$

From Ohm's law, $\vec{J} = \sigma_0 \vec{E}$, the DC conductivity of an isotropic electro gas became

$$\sigma_0 = \left(\frac{n_e e^2}{m_e \nu_c} \right) \quad (2.73)$$

The electron mobility μ_e is

$$\mu_e = v_e / E = -e / m_e \nu_c = -\sigma_0 / n_e e \quad (2.74)$$

2.3.1.2 Anisotropic Magnetoplasma

The steady state Langevin equation with magnetic fields can be written as

$$0 = -e(\vec{E} + \vec{v}_e \times \vec{B}_0) - \nu_c m_e \vec{v}_e \quad (2.75)$$

where \vec{B}_0 is a constant and uniform magnetic field. Using (2.72)

$$\vec{J} = \sigma_0(\vec{E} + \vec{v}_e \times \vec{B}_0) \quad (2.76)$$

where σ_0 is in (2.73).

It is worth to consider a useful result which arises when the collisional effects are negligible. If collisional effects are dominant compared to the effects of the magnetic fields, then the plasma can not be magnetized.

When $\nu_c \rightarrow 0$ the DC conductivity becomes very large ($\sigma_0 \rightarrow \infty$). So, we have

$$\vec{E} + \vec{v}_e \times \vec{B}_0 = 0 \quad (2.77)$$

If we take cross product of \vec{B}_0 on both sides then

$$(\vec{v}_e \times \vec{B}_0) \times \vec{B}_0 = -\vec{E} \times \vec{B}_0 \quad (2.78)$$

where $(\vec{v}_e \times \vec{B}_0) \times \vec{B}_0 = -\vec{v}_{e\perp} B_0^2$, and

$$\vec{v}_{e\perp} = (\vec{E} \times \vec{B}_0)/B_0^2 \quad (2.79)$$

The DC conductivity dyad (tensor) $\bar{\sigma}$ is defined by Ohm's law,

$$\vec{J} = \bar{\sigma} \cdot \vec{E} \quad (2.80)$$

Consider a Cartesian coordinate system and $\vec{B}_0 = B_0 \hat{z}$, and plug $\vec{v}_e = -\vec{J}/en_e$ from (2.72) in (2.76).

$$\vec{J} = \sigma_0 \vec{E} - (\sigma_0 B_0/en_e)(\vec{J} \times \hat{z}) \quad (2.81)$$

Here

$$\vec{J} \times \hat{z} = J_y \hat{x} - J_x \hat{y}. \quad (2.82)$$

With the above relation, (2.81) becomes

$$\begin{aligned} J_x &= \sigma_0 E_x - (\omega_{ce}/\nu_c) J_y \\ J_y &= \sigma_0 E_y - (\omega_{ce}/\nu_c) J_x \\ J_z &= \sigma_0 E_z \end{aligned} \quad (2.83)$$

where $\omega_{ce} = e B_0 / m_e$. We can eliminate J_y and J_x from (2.83).

$$\begin{aligned} J_x &= \frac{\nu_c^2}{\nu_c^2 + \omega_{ce}^2} \sigma_0 E_x - \frac{\nu_c \omega_{ce}}{\nu_c^2 + \omega_{ce}^2} \sigma_0 E_y \\ J_y &= \frac{\nu_c \omega_{ce}}{\nu_c^2 + \omega_{ce}^2} \sigma_0 E_x + \frac{\nu_c^2}{\nu_c^2 + \omega_{ce}^2} \sigma_0 E_y \end{aligned} \quad (2.84)$$

In matrix form, we can write as

$$\begin{bmatrix} J_x \\ J_y \\ J_z \end{bmatrix} = \bar{\sigma} \begin{bmatrix} E_x \\ E_y \\ E_z \end{bmatrix}, \quad \bar{\sigma} = \begin{bmatrix} \sigma_{\perp} & -\sigma_H & 0 \\ \sigma_H & \sigma_{\perp} & 0 \\ 0 & 0 & \sigma_{\parallel} \end{bmatrix} \quad (2.85)$$

where

$$\begin{aligned} \sigma_{\perp} &\equiv \frac{\nu_c^2}{\nu_c^2 + \omega_{ce}^2} \sigma_0 \\ \sigma_H &\equiv \frac{\nu_c \omega_{ce}}{\nu_c^2 + \omega_{ce}^2} \sigma_0 \\ \sigma_{\parallel} &\equiv \frac{n_e e^2}{m_e \nu_c} \end{aligned} \quad (2.86)$$

2.3.2 AC Conductivity

Consider the case when the electric field and the mean electron velocity vary harmonically in time. Therefore, the linearized Langevin equation (2.70) becomes

$$-i\omega m_e \vec{v}_e = -e(\vec{E} + \vec{v}_e \times \vec{B}_0) - m_e \nu_c \vec{v}_e \quad (2.87)$$

$$0 = -e(\vec{E} + \vec{v}_e \times \vec{B}_0) - m_e(\nu_c - i\omega) \vec{v}_e \quad (2.88)$$

We replace ν_c by $(\nu_c - i\omega)$ in the DC conductivity dyad (2.86), then

$$\begin{aligned}\sigma_{\perp} &\equiv \frac{(\nu_c - i\omega)^2}{(\nu_c - i\omega)^2 + \omega_{ce}^2} \sigma_0 \\ \sigma_H &\equiv \frac{(\nu_c - i\omega)\omega_{ce}}{(\nu_c - i\omega)^2 + \omega_{ce}^2} \sigma_0 \\ \sigma_{\parallel} &\equiv \frac{n_e e^2}{m_e(\nu_c - i\omega)}\end{aligned}\tag{2.89}$$

2.3.3 The Plasma as a Dielectric Medium

So far, we have treated the plasma as a collection of charged and neutral particles moving about in their fields. A different approach is provided to treat the plasma as a dielectric medium by the use of a dielectric dyad, in which we are concerned only with the gross macroscopic properties of the plasma, not with the particle motions.

Instead of the Langevin equation, let us consider the following Ampere's law

$$\vec{\nabla} \times \vec{B} = \mu_0 \left(\vec{J} + \epsilon_0 \frac{\partial \vec{E}}{\partial t} \right)\tag{2.90}$$

and define the conductivity dyad $\vec{\bar{\sigma}}$ by the equation

$$\vec{J} = \vec{\bar{\sigma}} \cdot \vec{E}\tag{2.91}$$

With the above two equations and an assumption of time-harmonic variation, we obtain

$$\vec{\nabla} \times \vec{B} = \mu_0 \vec{\bar{\sigma}} \cdot \vec{E} - i\omega \mu_0 \epsilon_0 \vec{E}\tag{2.92}$$

We can rewrite

$$\begin{aligned}\vec{\nabla} \times \vec{B} &= -i\omega\mu_0\epsilon_0 \left(\bar{\bar{1}} + i\frac{\bar{\bar{\sigma}}}{\omega\epsilon_0} \right) \cdot \vec{E} \\ &= -i\omega\mu_0\bar{\bar{\epsilon}} \cdot \vec{E}\end{aligned}\tag{2.93}$$

where $\bar{\bar{1}}$ is the unit dyad, and $\bar{\bar{\epsilon}} = \epsilon_0(\bar{\bar{1}} + i\bar{\bar{\sigma}}/\omega\epsilon_0)$ is called the dielectric dyad for the plasma. The dielectric dyad can be written in matrix form as

$$\begin{aligned}\bar{\bar{\epsilon}} &= \epsilon_0 \begin{bmatrix} 1 & 0 & 0 \\ 0 & 1 & 0 \\ 0 & 0 & 1 \end{bmatrix} + \frac{i\epsilon_0}{\omega\epsilon_0} \begin{bmatrix} \sigma_{\perp} & -\sigma_H & 0 \\ \sigma_H & \sigma_{\perp} & 0 \\ 0 & 0 & \sigma_{\parallel} \end{bmatrix} \\ &= \epsilon_0 \begin{bmatrix} \epsilon_1 & -\epsilon_2 & 0 \\ \epsilon_2 & \epsilon_1 & 0 \\ 0 & 0 & \epsilon_3 \end{bmatrix}\end{aligned}\tag{2.94}$$

where

$$\begin{aligned}\epsilon_1 &= 1 + \frac{i}{\omega\epsilon_0}\sigma_{\perp} \\ \epsilon_2 &= \frac{i}{\omega\epsilon_0}\sigma_H \\ \epsilon_3 &= 1 + \frac{i}{\omega\epsilon_0}\sigma_{\parallel}\end{aligned}\tag{2.95}$$

Using (2.89) the dielectric dyad in (2.95) can be written as

$$\epsilon_1 = 1 + \frac{i}{\omega} \frac{(\nu_c - i\omega) \cdot \omega_{pe}^2}{(\nu_c - i\omega)^2 + \omega_{ce}^2}\tag{2.96}$$

$$\epsilon_2 = \frac{i}{\omega} \frac{\omega_{ce} \cdot \omega_{pe}^2}{(\nu_c - i\omega)^2 + \omega_{ce}^2}\tag{2.97}$$

$$\epsilon_3 = 1 + \frac{i}{\omega} \frac{\omega_{pe}^2}{\nu_c - i\omega}\tag{2.98}$$

where $\omega_{pe}^2 = n_e e^2 / m_e \epsilon_0$

Chapter 3

Numerical Method

Three approaches for the electron cyclotron emission analysis of the Hall thrusters are developed.

The first one employs the lumped plasma parameters from the simple plasma parameter models of a Hall thruster. The plasma parameter distributions are from the literature.

The second method is the microscopic point of view. This analysis employs the Monte Carlo (MC) method to select electrons thoroughly, and the Particle-in-cell (PIC) method to obtain the acceleration data of the electrons for the cyclotron emissions. Their trajectories are followed as they move within sampling period. ECE radiation is calculated with the acceleration data. The fast Fourier transform is taken to obtain the radiation in the frequency domain.

The last method is the macroscopic point of view. This analysis employs the hybrid finite element and moment methods (hybrid element method) to consider the plasma as inhomogeneous dielectric media. The cyclotron motion of the electrons is modeled with two dipoles with 90° phase difference. The plasma parameters and magnetic field in the thruster channel region are considered for the current sources of the dipoles.

3.1 Plasma Parameter Modeling for BPT-4000 class Hall thrusters

To analyze the ECE radiation, the magnetic field, electron temperature, and electron density distributions are important parameters. We assume that the plasma fills an annular region of width, w , inner radius, r_I , and length, L . The configuration of the Hall thruster considered in this study is shown in Figure 3.1. We note two critical points along the axial axis: z_a , a point in the throat, and z_b , the exit point. In distance normalized to L we assume

$$z_a = 0.5 \tag{3.1}$$

$$z_b = 0.8 \tag{3.2}$$

3.1.1 1D Modeling

In the 1D modeling, we assume that all quantities are independent of the azimuthal and radial directions, and depend only on position in the axial direction. To analyze the ECE radiation, the magnetic field, electron temperature, and electron density distributions are important parameters.

First, a 1D magnetic model is considered. In a typical Hall thruster, the radial field is dominant compared to the axial field [65]. Thus a 1D radial magnetic field might be adequate to approximate the ECE radiation. A shifted Gaussian (bell-shaped) magnetic field is assumed and the maximum value is at the exit plane [9]. The 1D magnetic field model is given by

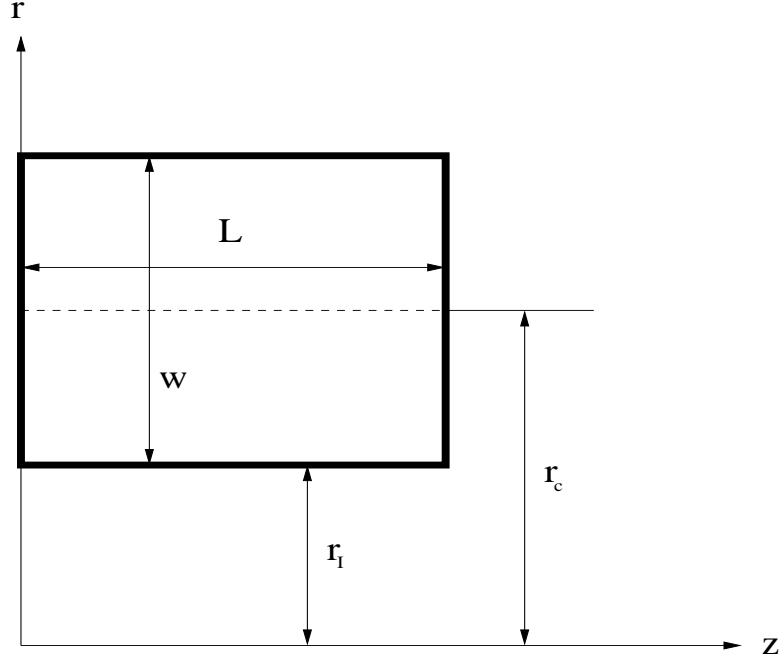


Figure 3.1: Hall thruster model

$$B_r(z) = B_0 + (B_{max} - B_0) \exp[-\{(z - z_b)/L_b\}^2] \quad (3.3)$$

where $B_0 = 0.2B_{max}$ and $B_{max} = 0.05$ T and $L_b = 0.6$. This profile of magnetic field distribution is shown in Fig. 3.2, which is in good agreement with experimental profiles [26, 69].

The electron temperature is not uniform in the channel, and decreases slightly toward the exit. This trend is reported in the literature [54]. Our 1D electron temperature model is given by

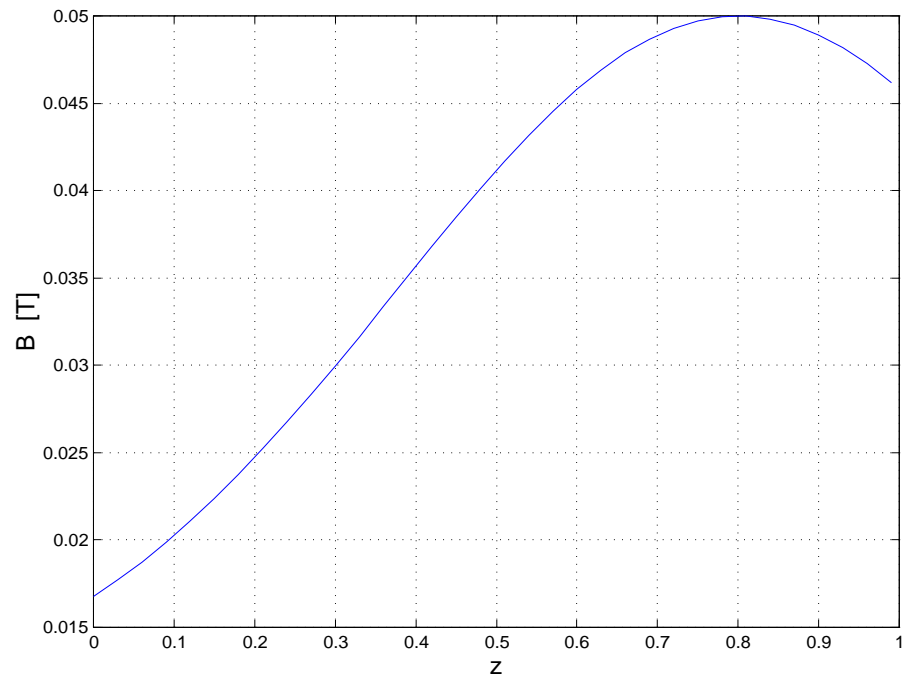


Figure 3.2: Radial magnetic flux density [T] along the normalized z axis for the 1D model.

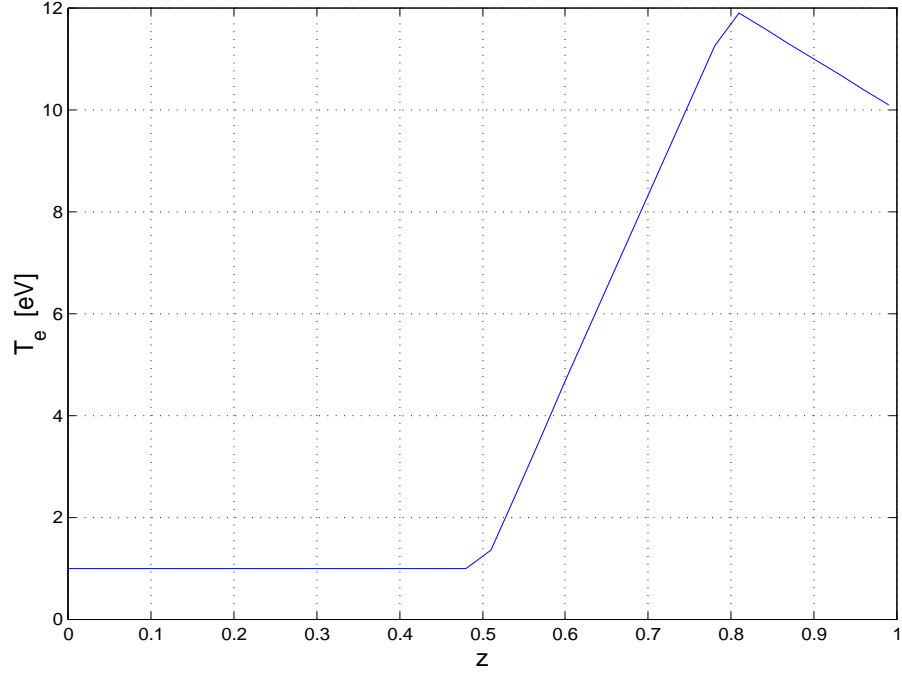


Figure 3.3: Electron temperature [eV] along the normalized z axis for the 1D model.

$$T_e = \begin{cases} T_a & \text{if } z < z_a \\ T_a + (T_b - T_a)(z - z_a)/(z_b - z_a) & \text{if } z_a < z < z_b \\ T_b + (T_c - T_b)(z - z_b)/(1.0 - z_b) & \text{if } z_b < z \end{cases} \quad (3.4)$$

where $T_a = 1$ eV, $T_b = 12$ eV, and $T_c = 10$ eV. The electron temperature distribution is shown in Fig. 3.3.

Most of the plasma in the channel of the Hall thruster is quasi-neutral. Therefore the electron density is the same as the ion density in the channel. Experimental results show that the plasma density reaches its peak value inside

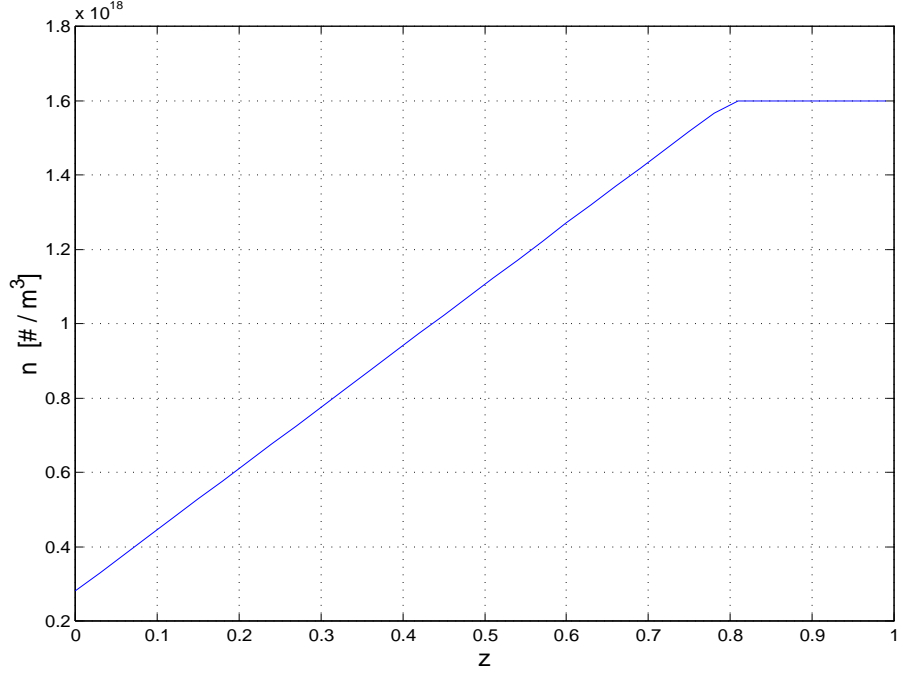


Figure 3.4: Electron density [$\# / m^3$] along the normalized z axis for the 1D model.

the acceleration channel. In this region, the radial magnetic field is maximum and thus a large number of electrons are inhibited from moving in the axial direction, resulting in the high probability of plasma production [9]. Our 1D electron density model is given by

$$n = \begin{cases} n_a + (n_b - n_a)z/z_b & z < z_b \\ n_b & z > z_b \end{cases} \quad (3.5)$$

where $n_a = 2.8 \times 10^{17} \text{ m}^{-3}$ and $n_b = 1.6 \times 10^{18} \text{ m}^{-3}$. The profile of the electron density is shown in Fig. 3.4.

3.1.2 2D Modeling

In the 2D plasma modeling, We assume that all quantities are independent of the azimuthal angle, which is axisymmetric, and depend on position in the axial and the radial directions. The two critical points along the axial direction are used in this modeling. Additionally some new parameters are introduced.

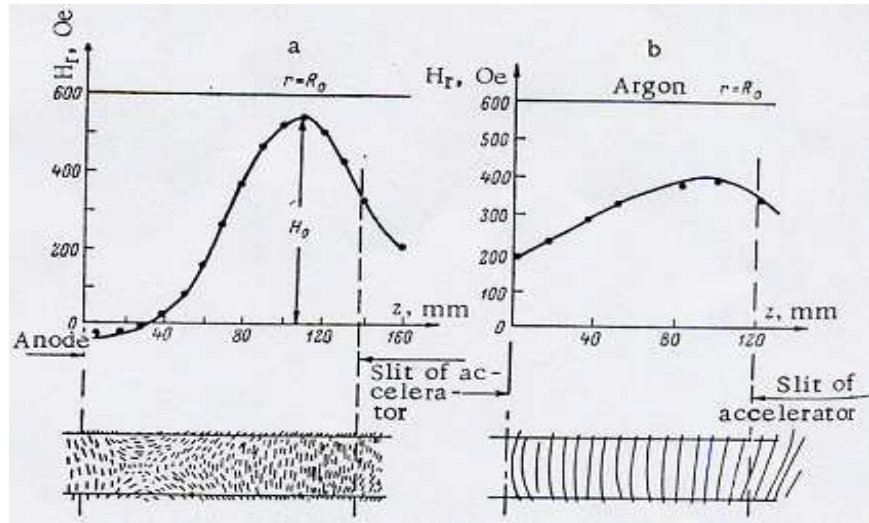
3.1.3 Magnetic Field Model

For a typical Hall thruster, the magnetic field density at the inner and outer walls of the channel is higher than at the center line of the channel. A shifted Gaussian (bell-shaped) radial magnetic field at center line is assumed and the maximum value is at the exit plane [9, 69]. The radial and axial magnetic field profiles at the inner wall, outer wall, and center line of the channel are based on the data given in [60]. These distributions are shown in Figure 3.5.

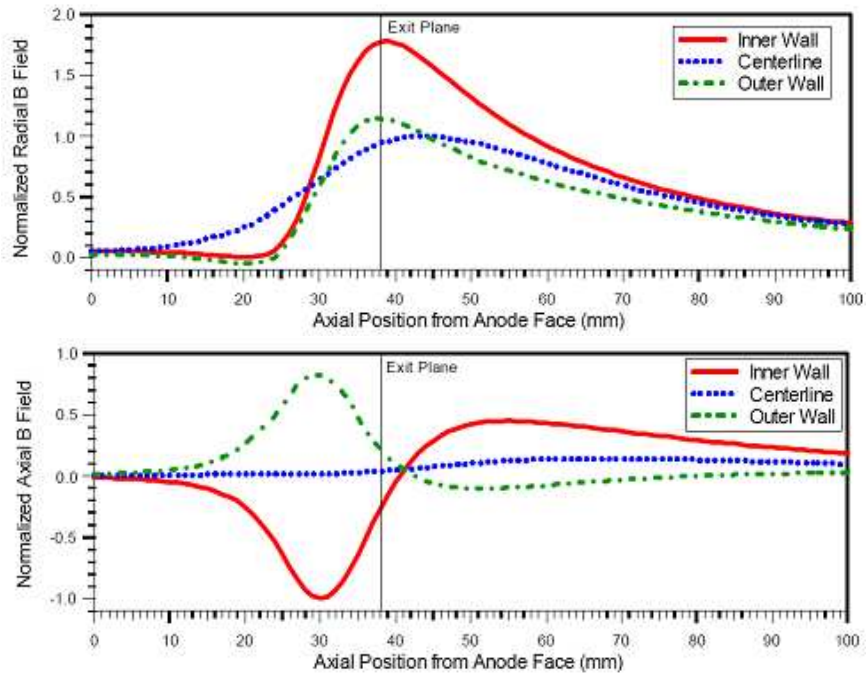
The 1D model, equation (3.3), is used as the radial magnetic field along the center line. The complete radial magnetic field model is given by

$$\begin{aligned}
 B_{rc}(z) &= B_0 + (B_{max} - B_0) \cdot e^{-[(z-z_b)/L_b]^2} \\
 B_{ri}(z) &= B_{0ri} (e^{-A_{r1}[(z-z_c)/L_c]^2} - e^{-A_{r2}[(z-z_c)/L_c]^2}) \\
 B_{ro}(z) &= B_{0ro} (e^{-A_{r1}[(z-z_c)/L_c]^2} - e^{-A_{r2}[(z-z_c)/L_c]^2})
 \end{aligned} \tag{3.6}$$

where B_{rc} , B_{ri} and B_{ro} are the radial magnetic field densities at the center line ($r = r_c$), inner wall ($r = r_I$) and outer wall ($r = r_c + w/2$), respectively, and



a)



b)

Figure 3.5: The measurements of the magnetic field from a) [69] and b) [60].

$B_0 = 0.2B_{max}$, $B_{max} = 0.05$ T, and $L_b = 0.6$. The plots for (3.6) are shown in Figure 3.6. We use $B_{0ri} = 2.2B_{max}$, $B_{0ro} = 1.4B_{max}$, $A_{r1} = 0.7$, $A_{r2} = 2.5$, $z_c = 0.25z_b$, and $L_c = 0.8L_b$. It is in good agreement with experimental profiles [26, 69].

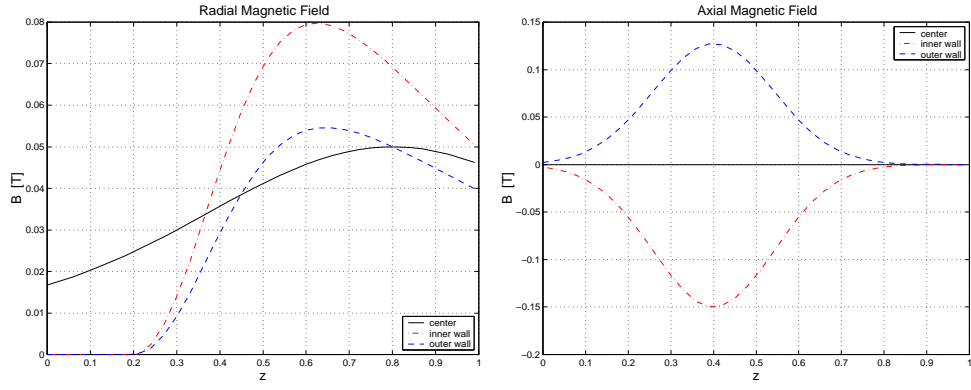
The axial magnetic field model is given by

$$\begin{aligned} B_{ac}(z) &= 0 \\ B_{ai}(z) &= -B_{0ai} \cdot e^{-A_{a1}[(z-z_d)/z_d]^2} \\ B_{ao}(z) &= B_{0ao} \cdot e^{-A_{a1}[(z-z_d)/z_d]^2} \end{aligned} \tag{3.7}$$

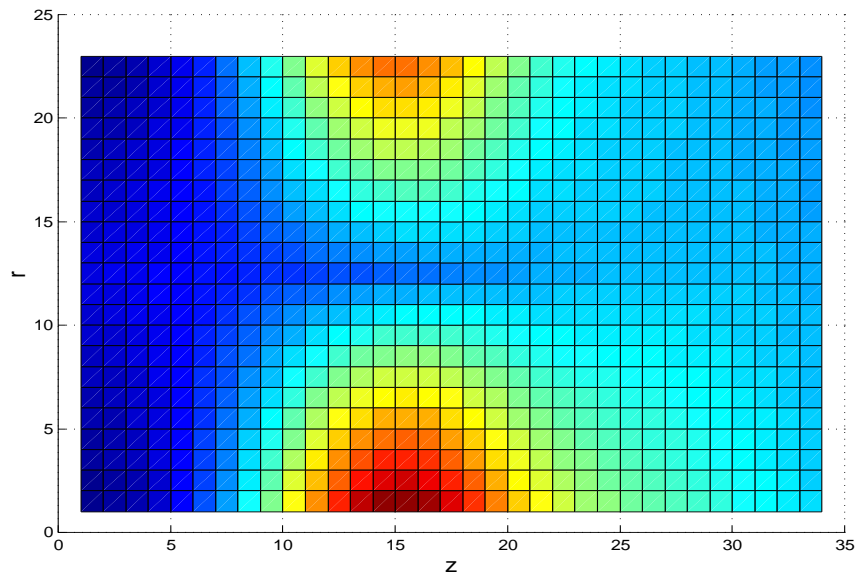
where B_{ac} , B_{ai} , and B_{ao} are the axial magnetic field density at the center line, inner wall and outer wall, respectively. The axial magnetic field densities from (3.7) are shown in Figure 3.6. $B_{0ai} = 3B_{max}$, $B_{0ao} = 2.5B_{max}$, $A_{a1} = 2.0$, and $z_d = 0.5z_b$. The axial magnetic field at the center line is approximately zero. The magnitude of the magnetic field density profiles with (3.6) and (3.7) are shown in Figure 3.6. The numbers on the axes at Figure 3.6 represent the cell number.

3.1.4 Electron Temperature Model

The electron temperature is not uniform in the channel, and the maximum temperature appears at the acceleration region but not at the exit plane. The electron temperature at the exit plane is actually equal to or lower than the maximum temperature. This trend is reported in the literature [54] and shown in Figure 3.7.



a)



b)

Figure 3.6: a) Magnetic field profiles of the model. b) The magnitude of magnetic field distribution of the model.

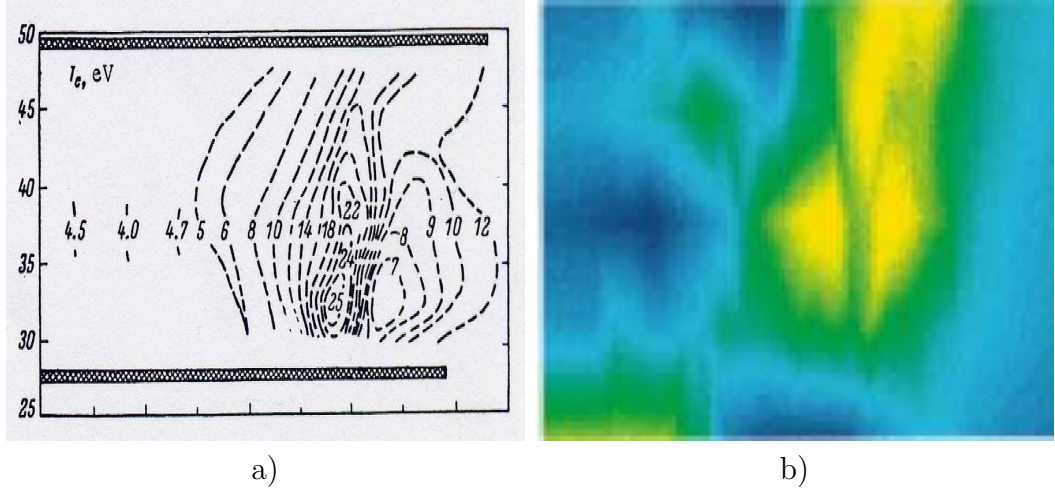


Figure 3.7: Electron temperature measurement from a) [9] and b) [29].

The electron temperature profile is based on the experimental data given in reference [9, 29]. A linear interpolation is used to model the electron temperature. The electron temperature model at the center line of the channel along the axial direction is given by

$$T_e^c = \begin{cases} T_a & \text{if } z < z_a \\ T_a + (T_b - T_a)(z - z_a)/(z_b - z_a) & \text{if } z_a < z < z_b \\ T_b + (T_c - T_b)(z - z_b)/(1.0 - z_b) & \text{if } z_b < z \end{cases} \quad (3.8)$$

where $T_a = 1$ eV, $T_b = 12$ eV, and $T_c = 10$ eV. The radial model for the electron temperature is given by

$$T_e^r = T_e^c - \frac{T_c - T_b}{1.0 - z_b} |r - r_c| \quad (3.9)$$

where T_e^r is the electron temperature on the radial axis at a given axial position, and r_c is the radius of the center line. r_c is also a normalized value. The slope

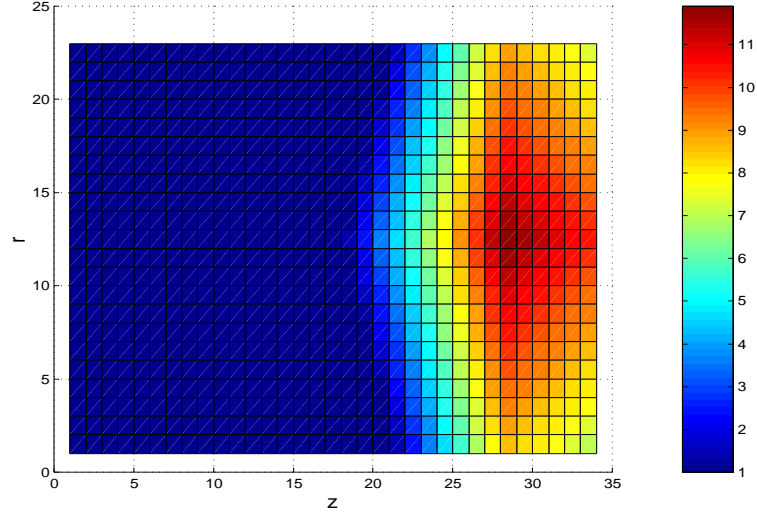


Figure 3.8: Electron temperature [eV] profiles of the model.

of equation (3.9) is the same as the slope of the last condition of equation (3.8).

The 2D axial electron temperature distribution at the center line of the channel is the same as the 1D electron temperature model, equation (3.8). The profile is given in Figure 3.3. The electron temperature distribution used in this study is shown in Figure 3.8.

3.1.5 Electron Density Model

Most of the plasma in the channel of the Hall thruster is quasi-neutral. Therefore the electron density is the same as the ion density in the channel. Experimental results show that the plasma density reaches its peak value inside the acceleration channel. The experimental results from literature are shown

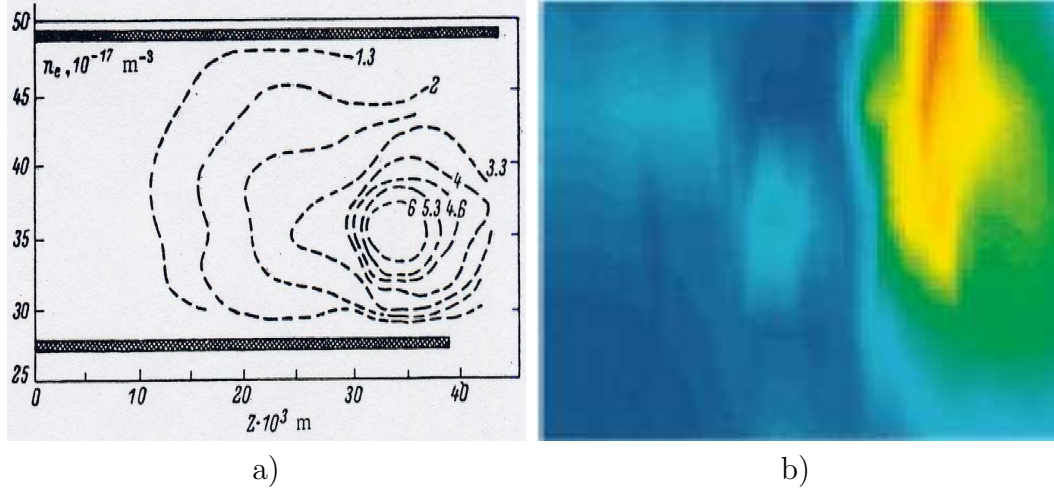


Figure 3.9: Electron density measurement from a) [9] and b) [29].

in Figure 3.9 In this region, the radial magnetic field is maximum, and thus a large number of electrons are inhibited from moving in the axial direction, resulting in the high probability of plasma production [9].

The electron density model at the center line is given by

$$n^c = \begin{cases} n_a + (n_b - n_a)z/z_b & z < z_b \\ n_b & z > z_b \end{cases} \quad (3.10)$$

where $n_a = 2.8 \times 10^{17} \text{ m}^{-3}$ and $n_b = 1.6 \times 10^{18} \text{ m}^{-3}$.

In order to model the 2D electron density profile, we use the ion density measurement data given in [21, 29]. The axial electron density profile for the 2D model is the same as the 1D model, (3.10). The electron density model along the radial axis is given by

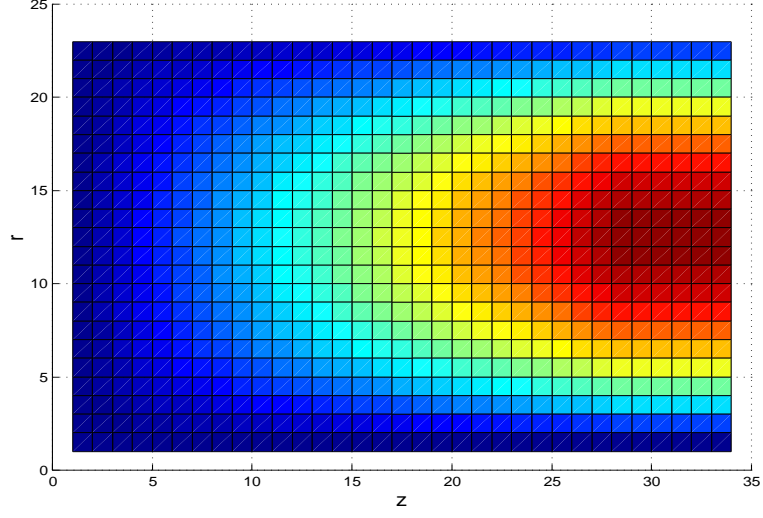


Figure 3.10: The electron density $[\#/m^3]$ profiles of the model

$$n^r = \begin{cases} n^c - \{(n^c - n_a)/r_1^2\} \cdot (r - r_1)^2 & r < r_1 \\ n^c - \{(n^c - n_a)/(w - r_1)^2\} \cdot (r - r_1)^2 & r > r_1 \end{cases} \quad (3.11)$$

where n^r and n^a are the radial and axial electron densities, respectively, and r_1 is the radial position parameter, which means the highest electron density region.

The axial electron density, n^a , is from (3.10), and is dependent on the axial position. The 2D electron density distribution at the center line of the channel ($r_1 = 0.5$ case) is the same as the 1D electron density model, (3.10) and Figure 3.4. The electron density distribution is shown in Figure 3.10.

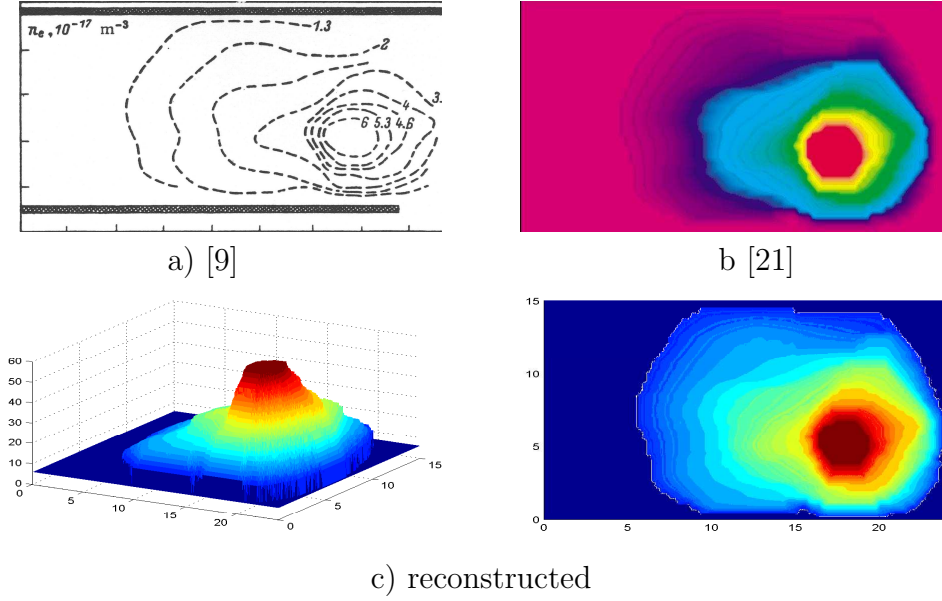


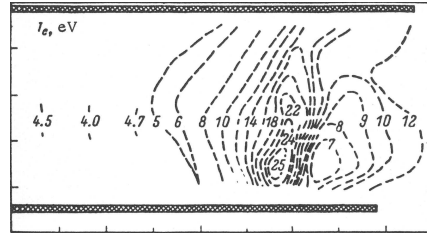
Figure 3.11: Electron density distributions.

3.2 Plasma Parameters for SPT100 class Hall thrusters

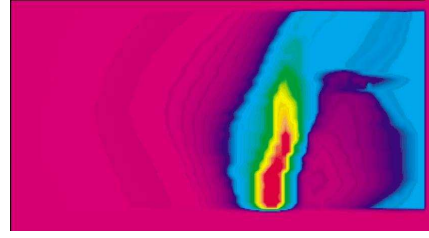
Measured plasma properties and analyzed magnetic field for SPT100 class Hall thrusters were presented in many papers [9, 21, 29, 60, 65].

3.2.1 Electron Density and Electron Temperature

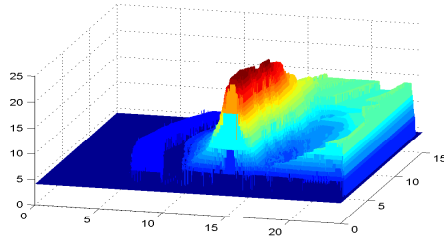
The electron density and electron temperature distributions [9, 21, 65] are reconstructed and used again in this study. Electron density distributions from the literature and reconstructed in this study are shown in Figure 3.11, and electron temperature distributions are shown in Figure 3.12. Electric field distribution is also adopted from [21] and is shown in Figure 3.13.



a) [9]

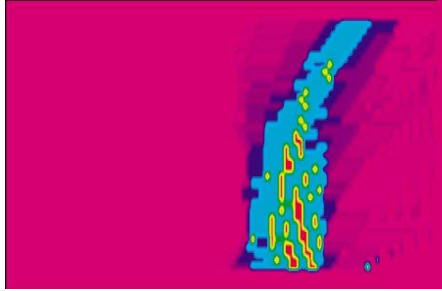


b) [21]

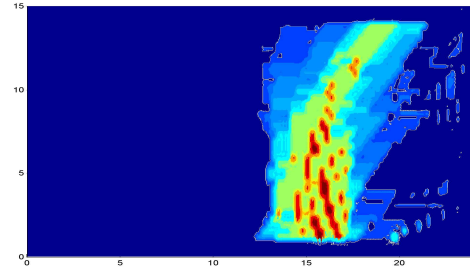


c) reconstructed

Figure 3.12: Electron temperature distributions.



a)



b)

Figure 3.13: Electron temperature distribution a) from [9] b) from [21] c) reconstructed.

3.2.2 Magnetic Field

As mentioned before, not only radial but also axial magnetic field information is required for 2D analysis. Unfortunately, we could not obtain the structures and currents information to perform magnetic field analysis, so an alternate way to obtain the magnetic field distribution was tried. Many, but limited, information about magnetic field distributions of Hall thrusters are in literature. Generally, equipotential contours and radial distributions of the magnetic fields can be easily obtained. Equipotential contours of the magnetic fields are from [9, 60] and are shown in Figure 3.14. Radial magnetic field distributions at the center lines are from [9, 11] and are shown in Figure 3.15. If we can generate a similar contour pattern to the measurement and can obtain the radial magnetic field distribution from the generated contour pattern, then the generated contour pattern is weighted according to the scale between the generated radial field distribution and the measurement. Target contour patterns for this approach are shown in Figure 3.14, and radial magnetic field distributions from literature are in Figure 3.15.

We generated similar field contours to the information in Figure 3.14 and took the radial magnetic field data at the center line. Then the data is compared to the the references and is weighted to match the information. The generated field contour and the final radial field distribution at the center line in the contour are shown in Figure 3.16. The generated magnetic field closely matches the trend from the references around the exit plane. Field density at the exit plane is higher than at the anode side (inside of the channel),

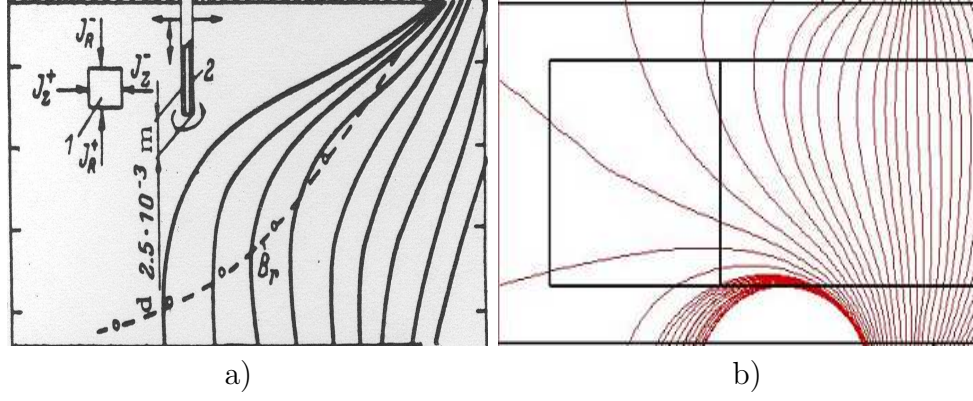


Figure 3.14: Contour plot of magnetic field a) from [9] b) from [60]

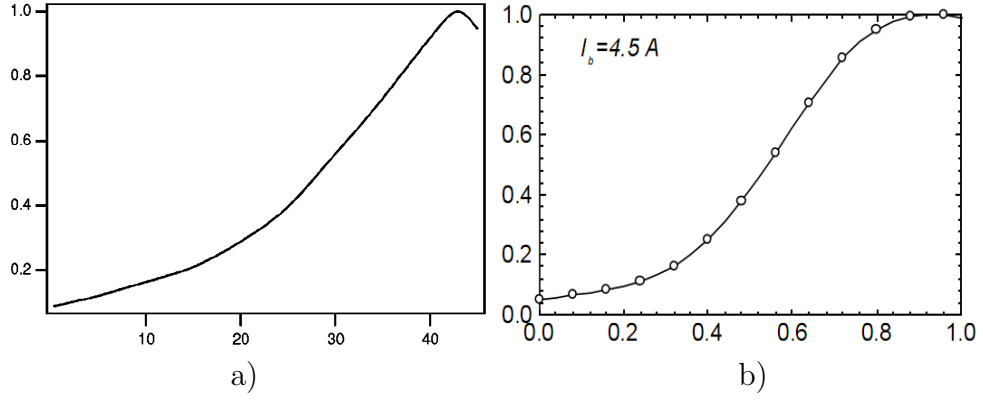


Figure 3.15: Radial magnetic field distribution at the center line a) from [9] b) from [11].

and most of the field is radial. The radial field distribution also shows good agreement at the exit plane. The exit region is more important for this analysis than the inside of channel. This is because the exit region has dominant values of plasma parameters: magnetic fields, electron density, and electron temperature. However, half of the channel from the anode side is different. It has a stronger magnetic field at the center line in our simulation than in the references. In the references, it also shows much less density than that of exit plane region. The magnetic field profiles from the literature are for optimized Hall thrusters, but the generated distribution is from simplified conventional structure and arbitrary currents. Consequently, generated field has wider low density region of magnetic field. This is a low frequency region, so the region is relatively less important than the exit plane region. This difference of magnetic field distribution can affect the results.

3.3 The Monte Carlo Method

Statistical simulation methods may be contrasted to conventional numerical discretization methods, which typically are applied to ordinary or partial differential equations that describe some underlying physical or mathematical system. In many applications of Monte Carlo, the physical process is simulated directly, and there is no need to even write down the differential equations that describe the behavior of the system.

The only requirement for the Monte Carlo simulation is the physical or mathematical system described by probability density functions (PDFs).

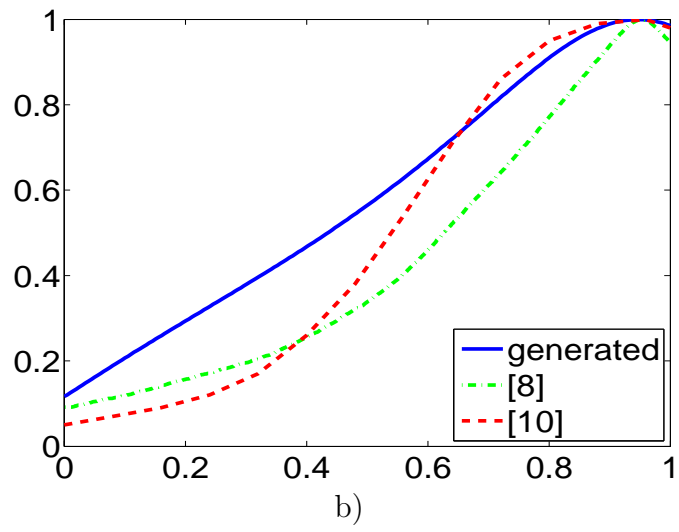
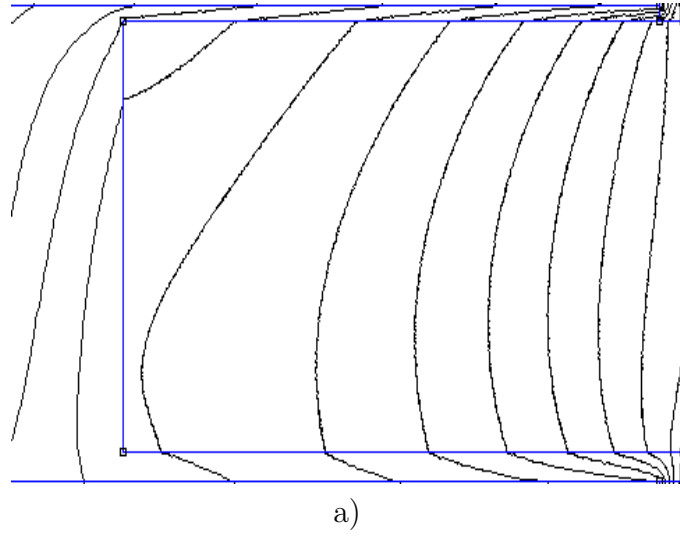


Figure 3.16: a) Generated field contour and b) radial field distributions at center lines in magnetic field modeling for PIC

For now, we will assume that the behavior of a system can be described by PDFs. Once the PDFs are known, the Monte Carlo simulation can proceed by random sampling from the PDFs. The outcomes of these random samplings must be accumulated in an appropriate manner to produce the desired result, but the essential characteristic of Monte Carlo is the use of random sampling techniques to arrive at a solution of the physical problem. In many practical applications, we can predict the statistical error, the variance, in this average result, and hence estimate of the number of Monte Carlo trials that are needed to achieve a given error.

3.3.1 Numerical Applications

Now, examples including the normal, log normal, exponential, and Maxwell-Boltzmann distributions are examined with the Monte Carlo method. The first is the normal distribution. The PDF of the normal distribution of random variable x with the median of 0 and the standard deviation of 1 is given by

$$f(x) = \frac{1}{\sqrt{2\pi}} e^{-x^2/2} \quad (3.12)$$

The CDF of (3.12) is given by

$$F(x) = \frac{1}{2} \left[1 + \operatorname{erf} \left(\frac{x}{\sqrt{2}} \right) \right] \quad (3.13)$$

where erf stands for the error function and is equivalent to $2/\sqrt{\pi} \int_0^x e^{-t^2} dt$.

The inversion of (3.13) is given by

$$F^{-1}(\xi) = \sqrt{2} \operatorname{erf}^{-1}(2\xi - 1) \quad (3.14)$$

Samples from 10 to 10,000 are tried with (3.14), and the results are in Figure 3.17. The left column is PDFs and the right one is CDFs. The result from the Monte Carlo method shows good agreement with the distribution from 100 samples in CDFs, and we can also see fairly good agreement from 1000 samples in PDFs.

The PDF of the log normal distribution with the median of 1 and the geometric standard deviation of 1 is given by

$$f(x) = \frac{1}{\sqrt{2\pi}x} e^{-(\ln x - 1)^2/2} \quad (3.15)$$

The CDF of (3.15) is given by

$$F(x) = \frac{1}{2} \left[1 + \operatorname{erf} \left(\frac{\ln x - 1}{\sqrt{2}} \right) \right] \quad (3.16)$$

The inversion of (3.16) is given by

$$F^{-1}(\xi) = \exp \left(\sqrt{2} \operatorname{erf}^{-1}(2\xi - 1) + 1 \right) \quad (3.17)$$

The result of the Monte Carlo sampling for the log normal distribution is shown in Figure 3.18. The result shows the same trend as the normal distribution one.

The third is the exponential distribution. The PDF with rate parameter of 1 is given by

$$f(x) = e^{-x} \quad x \geq 0 \quad (3.18)$$

The CDF of the exponential distribution is given by

$$F(x) = 1 - e^{-x} \quad (3.19)$$

The inverse function of (3.19) is given by

$$F^{-1}(\xi) = -\ln(1 - \xi) \quad (3.20)$$

The result shown in Figure 3.19 has the same trend as the two previous results.

The last is the Maxwell-Boltzmann distribution of speeds. The PDF of the distribution is written as

$$f(v) = 4\pi \left(\frac{m}{2\pi kT} \right)^{3/2} v^2 \exp \left(-\frac{mv^2}{2kT} \right) \quad (3.21)$$

The CDF of the Maxwell-Boltzmann distribution is given by

$$F(x) = \operatorname{erf} \left(\frac{x}{\sqrt{2}a} \right) - \sqrt{\frac{2}{\pi}} \frac{x}{a} e^{-x^2/(2a^2)} \quad (3.22)$$

The inverse function of the CDF (3.22) is implemented with the cubic spline interpolation [78]. The Monte Carlo sampling result with the Maxwell-Boltzmann distribution of speeds is shown in Figure 3.20. This result also has the same trend as before.

According to our results from the normal to the Maxwell-Boltzmann distributions, we can say that taking over 100 samples has good agreement with the CDF, and taking over 1000 samples shows fairly good matches to both the PDFs and the CDFs. Consequently, if more than 1000 samples are selected, then it is enough to represent the distribution.

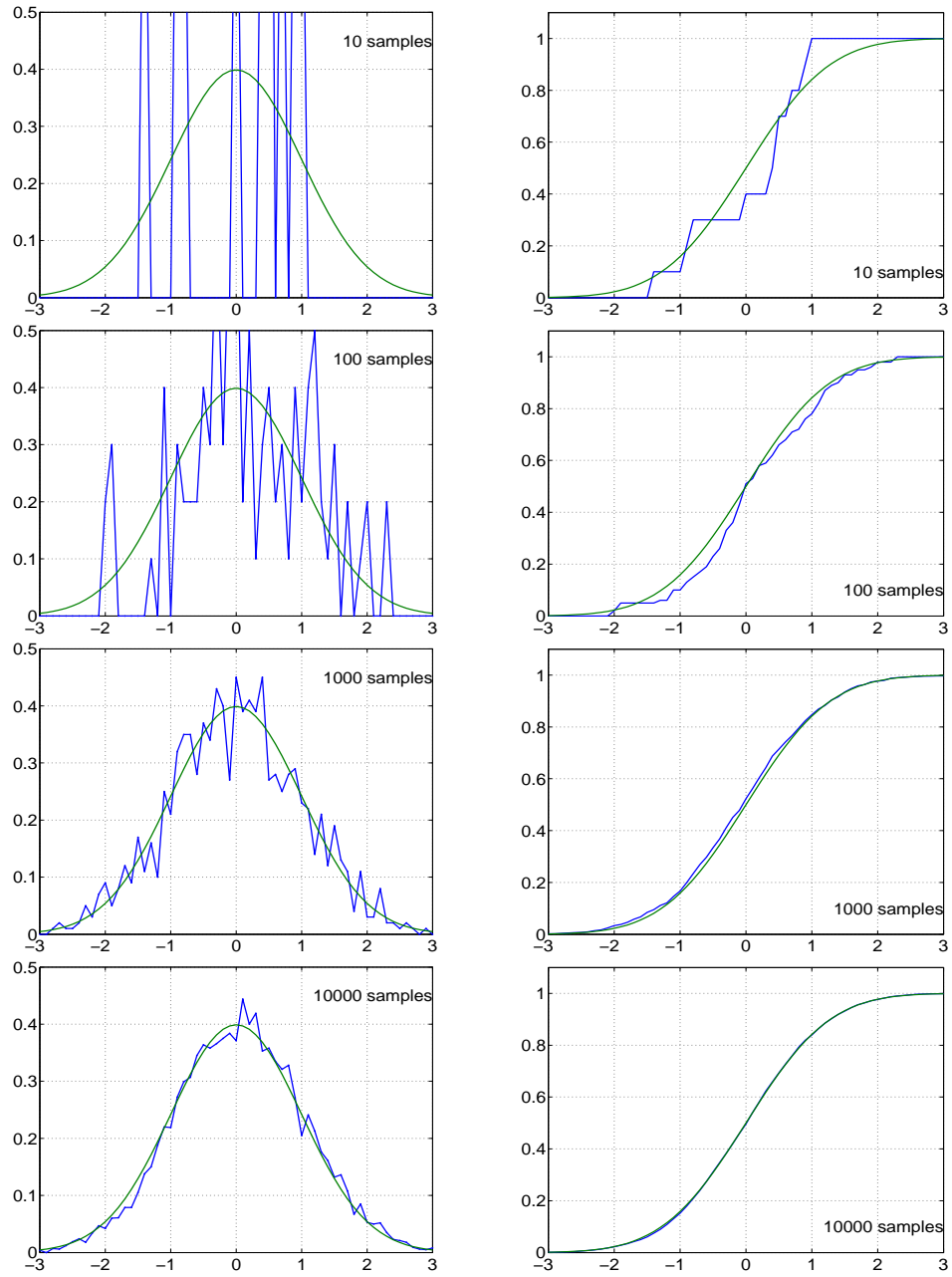


Figure 3.17: Monte Carlo on the normal distribution. The graphs in the left column are PDFs and in the right column are CDFs.

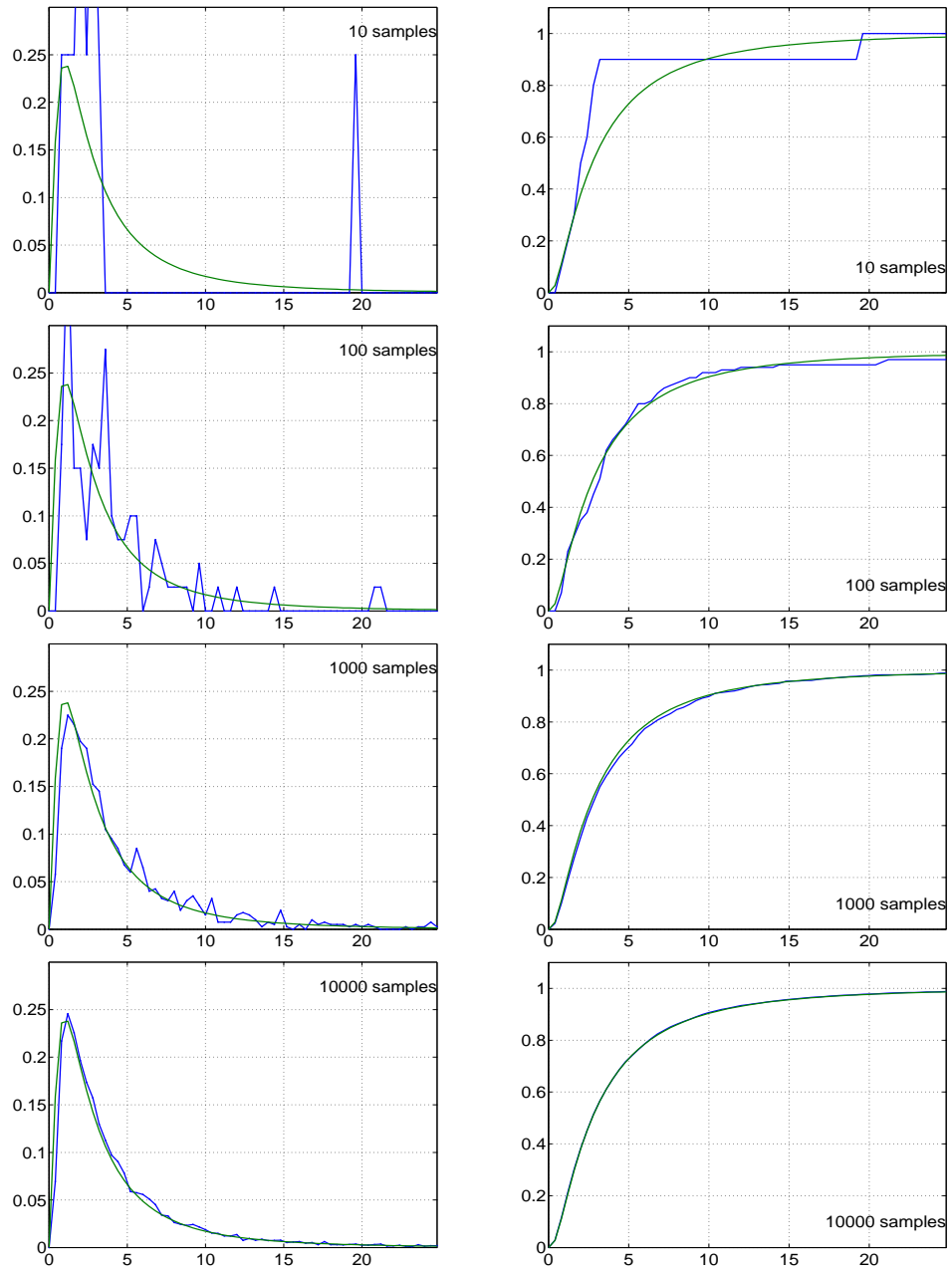


Figure 3.18: Monte Carlo on the log normal distribution. The graphs in the left column are PDFs and in the right column are CDFs.

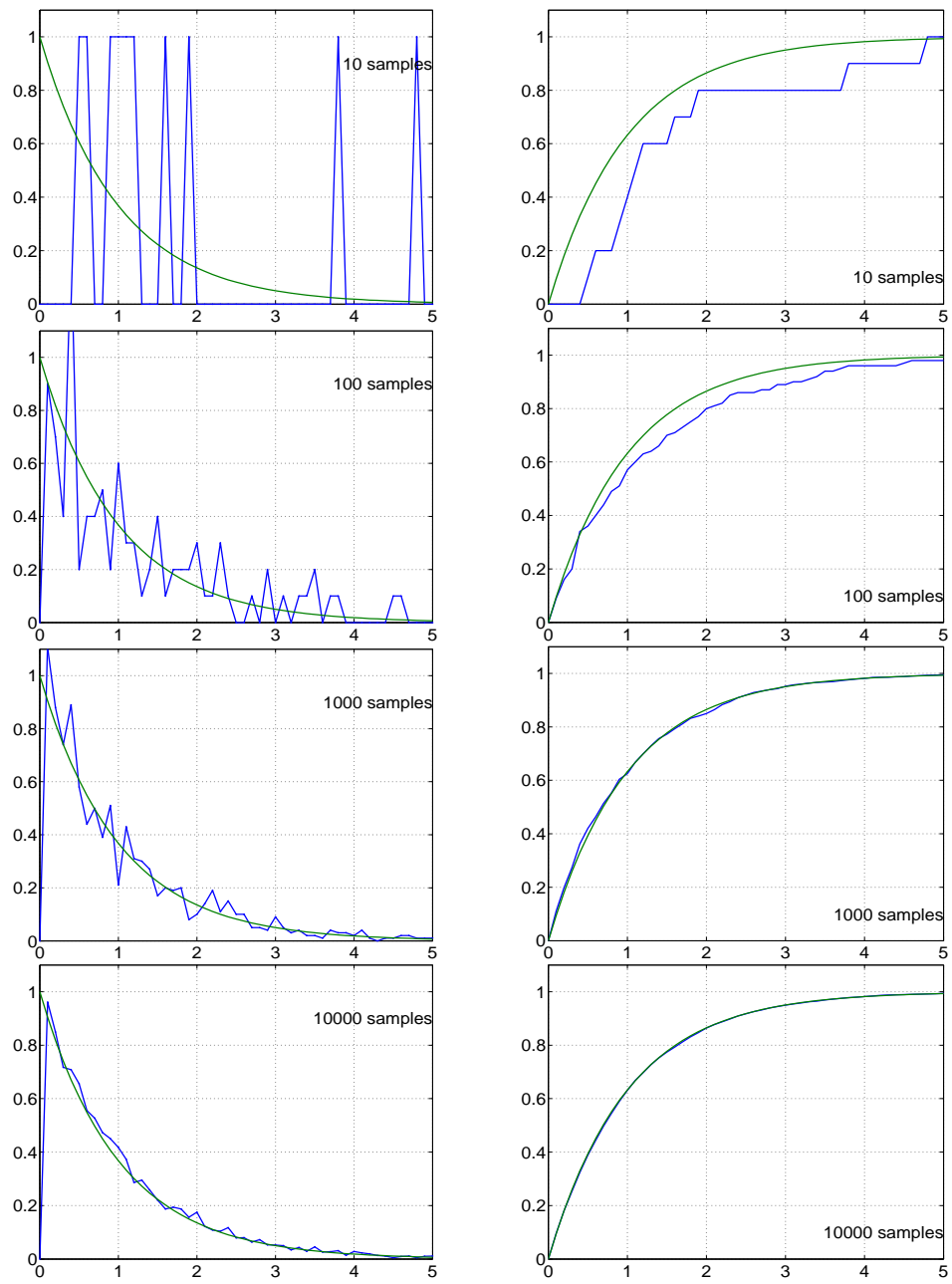


Figure 3.19: Monte Carlo on the exponential distribution. The graphs in the left column are PDFs and in the right column are CDFs.

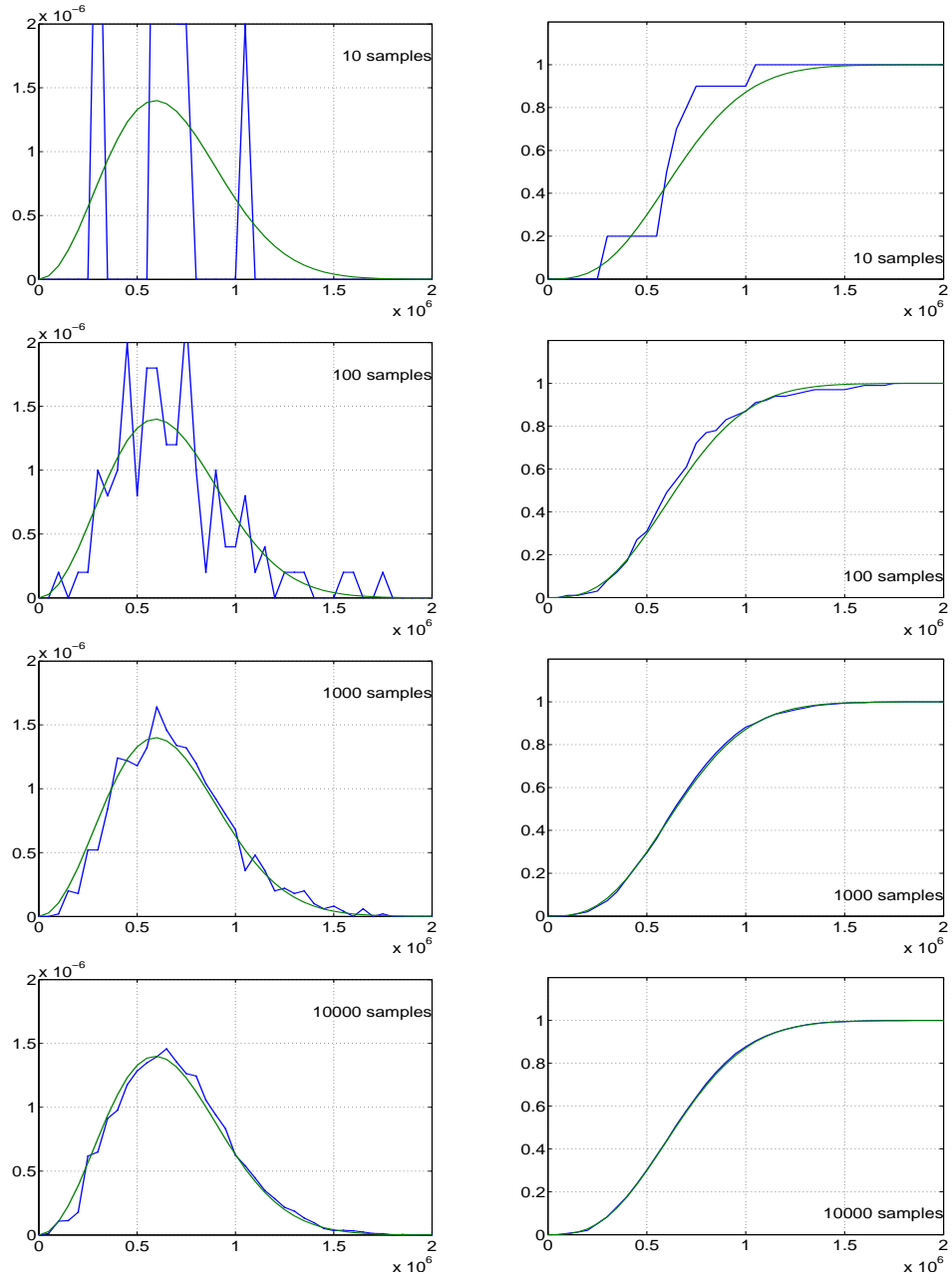


Figure 3.20: Monte Carlo on the Maxwell-Boltzmann distribution of speeds. The graphs in the left column are PDFs and in the right column are CDFs.

3.4 Particle-In-Cell

There are many ways to analyze radiation. Two approaches are suggested in this study. By definition, the radiation is from charge acceleration [6, 7, 33]. In the first approach, we solve for the charge acceleration from the Lorentz equation. We then use the solution to simulate the radiation. The radiation is ultimately shown in the frequency domain. We will now discuss electron-neutral collisions in this particle-in-cell code.

3.4.1 Selecting Electrons

We select electrons for the first step of this analysis. One electron represents a certain number of electrons in this analysis. Generally, electrons are in the position and velocity coordinates. Electrons in this analysis have the position, velocity and acceleration coordinates. We randomly select the initial positions for the electrons with the uniform distribution. The velocities of the electrons are also selected stochastically. Velocities have two components, speed and direction. Let us consider the two components separately.

3.4.1.1 Maxwell-Boltzmann Distribution of Speed

The speed of electrons in the Hall thrusters is well represented by the Maxwell-Boltzmann distribution in many cases [13, 17, 21]. In this numerical approach, the distribution is embodied with the Monte Carlo method shown in section 3.3.1, and only this distribution is tried. However, we can easily expand this to other distributions.

3.4.1.2 Isotropic Velocity

After a collision, not only the speed, but also the direction of the electrons is random. It is called isotropic velocity. Therefore, the unit vector of the velocity is uniformly distributed on the surface of a unit sphere.

First, we try a simple linear relationship with uniformly distributed random variables on the interval $[0,1]$. We then try a suggested relationship to consider the variation of the surface area as a function of θ . The simple linear relationship is given by

$$\begin{cases} \theta &= \pi \cdot x_1 \\ \phi &= 2\pi \cdot x_2 \end{cases} \quad x_1, x_2 = [0, 1] \quad (3.23)$$

The surface area of a sphere from $\theta = 0$ does not linearly increase along θ . The suggested relationship is formulated to consider this nonlinearity, and is written by

$$\begin{cases} \theta &= \arccos(1 - 2 \cdot x_1) \\ \phi &= 2\pi \cdot x_2 \end{cases} \quad x_1, x_2 = [0, 1] \quad (3.24)$$

The linear and suggested relationships mentioned above are tried on the unit sphere, and the results are projected on the x-y and x-z planes and are shown in Figures 3.21 and 3.22, respectively. In Figure 3.21, highest density of points occurs at the center in a), and the points are more concentrated on the top and bottom sides of the sphere in b). It shows that this relationship does not have uniformly distributed velocity. In figure 3.22, however, the points are distributed evenly and randomly.

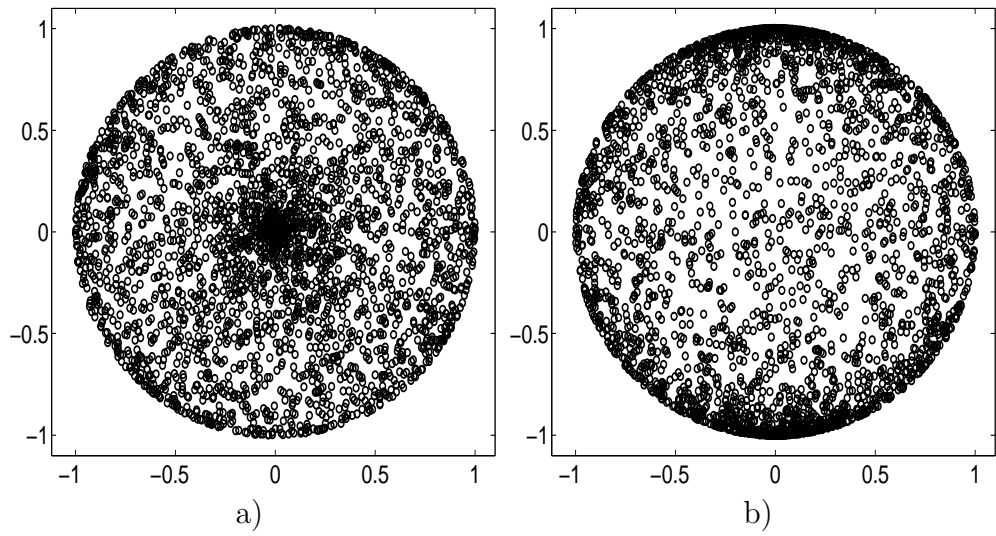


Figure 3.21: Isotropic velocity on the unit sphere from 3.23. a) top view b) side view

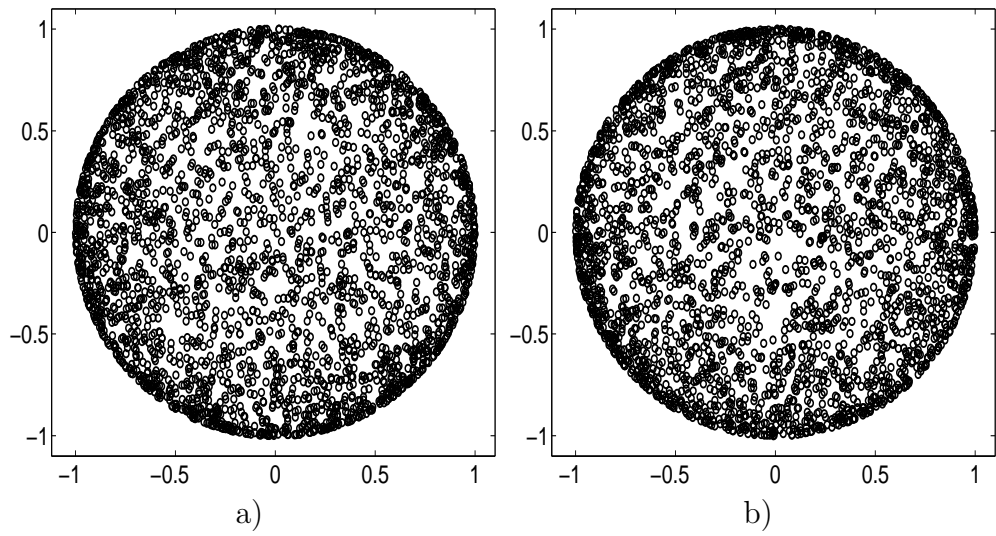


Figure 3.22: Isotropic velocity on the unit sphere from 3.24. a) top view b) side view

3.4.2 Time Scale

The electron motions are calculated from the Lorentz force equation with a sampling time. Deciding the sampling time and total sampling period is very important for the PIC method. Shorter sampling time and a longer time period are, of course, better for the computational accuracy, but it requires a higher performance of computing. On the other hand, bigger sampling time and a shorter time period are better for computational load. We need to find compromising values to achieve both higher accuracy and acceptable computational load. The time scale is considered from these two points of view.

3.4.2.1 Fourier Transform Point of view

The electric field from the accelerated electron is calculated with (2.66) and the Fourier transform is taken to obtain the electric field in the frequency domain.

The sampling time and the total sampling period are decided from the maximum frequency and the resolution in the frequency domain, respectively. The frequency range of ECE is from 1 to 5 GHz. Analysis range up to 50 GHz is enough to cover the ECE radiation, and the resolution of 100 MHz is also detailed enough to check the results. The sampling time is given by $1/(2 \cdot 50GHz) = 1 \times 10^{-11}s$, and the total sampling period is written by $1/100 \text{ MHz} = 1 \times 10^{-8}s$.

3.4.2.2 Magnetic field Point of view

In a numerical simulation, the motion of one particle is stable for $\omega\Delta t < 2$, and accurate for $\omega\Delta t \leq 0.2$ [8, 22]. In this analysis, ω is ω_{ce} and the maximum magnetic field in the channel region is 1550 G. For the maximum field, 1550 G, Δt is less than $7.3 \times 10^{-12}s$

For the sampling time, $7.3 \times 10^{-12}s$ is chosen from the magnetic field point of view, and $1 \times 10^{-8}s$ is chosen for the total sampling period from the Fourier transform point of view. If we consider a little margin for the sampling time, then $5 \times 10^{-12}s$ is good enough. During the sampling period of $1 \times 10^{-8}s$, 2000 samples are needed with the sampling time of $5 \times 10^{-12}s$. The resulting range in the frequency domain is up to 100 GHz from $1/(2 \cdot 5 \times 10^{-12})$ with the resolution of 100 MHz from $1/(2000 \cdot 5 \times 10^{-12})$.

2048 samples, instead of 2000, can be taken to use the fast Fourier transform. Then, the frequency range of the result is same as the range of the 2000 sample case. The resolution is 97.7 MHz from $1/(2048 \cdot 5 \times 10^{-12})$. If 4096 samples are chosen, the frequency range is same as previous cases, but the resolution is half of the 2048 case, 48.8 MHz, $1/(4096 \cdot 5 \times 10^{-12})$.

3.4.3 Collision Frequency

To check collision frequency, the cross section information for the species is required. Scattering cross sections obtained from the literature are presented in Figure 3.23, and the cross sections for low-energy region is in Figure 3.24.

Collision frequency is given by

$$\nu_c = n_e Q_t v_e \quad (3.25)$$

where n_e is electron density, Q_t is the total scattering cross section, and v_e is the electron velocity. The collision frequency from (3.25) is in Figure 3.25. Here, n_e is assumed to be $1 \times 10^{18} \text{cm}^{-3}$.

As shown in Figure 3.25, the collision frequency is less than 1 MHz in all regions. The target frequency for this analysis is higher than 100 MHz as we saw previously in section 3.4.2. Conclusively, we can generally say that this plasma can be treated as a collisionless one in this analysis.

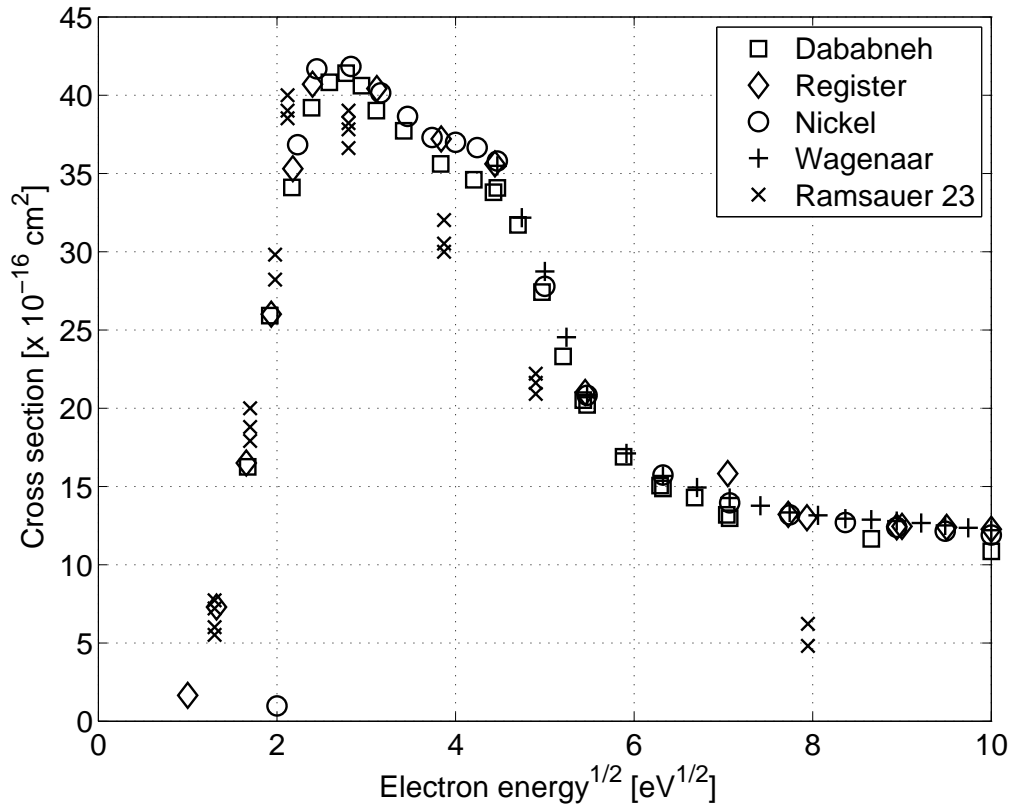


Figure 3.23: Cross section of Xe for high-energy region. Dababneh [72, 73], Register [79], Nickel [36], Wagenaar [80], and Ramsauer 23 [63]

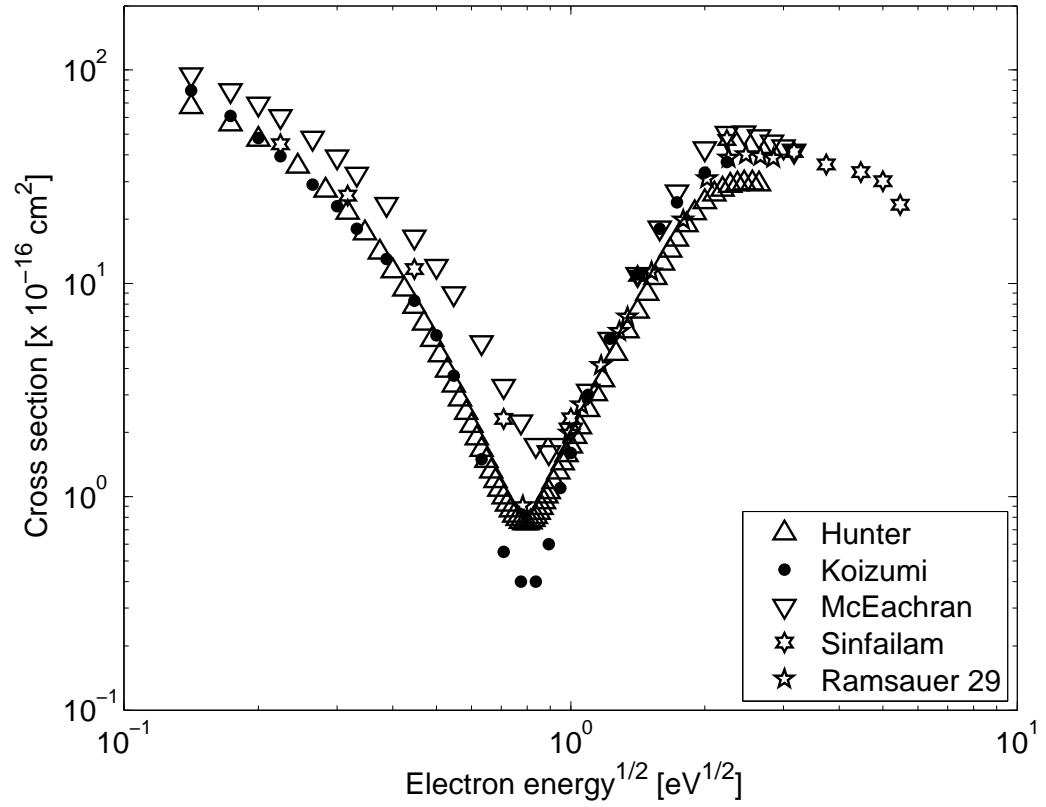


Figure 3.24: Cross section of Xe for low-energy region. Hunter [18], Koizumi [70], McEachran [52], Sinfailam [71], and Ramsauer 29 [64]

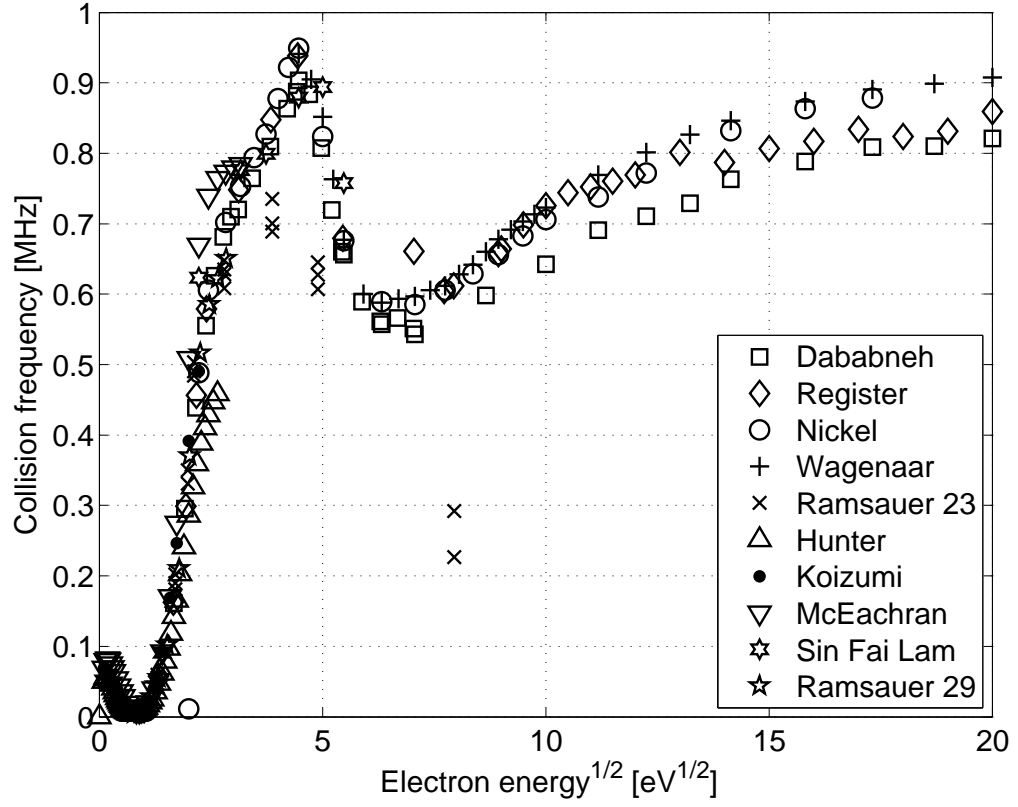


Figure 3.25: Collision frequency of Xe Dababneh [72, 73], Register [79], Nickel [36], Wagenaar [80], Ramsauer 23 [63], Hunter [18], Koizumi [70], McEachran [52] Sinfailam [71], and Ramsauer 29 [64]

3.5 Numerical Modeling of Electromagnetic Radiation

3.5.1 Hybrid Element Method

A hybrid element method [47] has been devised where finite elements are coupled to boundary elements.

The basic technique is to apply the equivalence principle to transform the original problem into interior and exterior problems, which are coupled on the exterior dielectric body surface through the continuities of the tangential electric field and magnetic field. The interior problem involving the inhomogeneous medium is solved by the finite element method, and the exterior problem involving unbounded region is solved by the moment method [88]. A detailed formulation of the hybrid moment and finite element method is described in [47].

A hybrid method code named EMAP5 was announced from the electromagnetic compatibility laboratory of the university of Missouri-Rolla [34, 39, 86]. EMAP5 is a full-wave electromagnetic field solver that combines the method of moments with a vector finite element method [25]. The FEM is employed to handle the interior domain of inhomogeneous dielectric bodies and the method of moments is used to develop surface integrals that relate the field quantities on boundary surfaces with the equivalent surface currents. These integral equations are then coupled to the finite element equations through the continuity of the tangential magnetic fields [34]. EMAP5 is designed primarily to simulate electromagnetic interference sources at the printed circuit board level [2]. They tried many other examples with EMAP5 [25, 81, 85]. The

EMAP5 code can be freely downloaded from the website [25]. We use EMAP5 to analyze the radiation of the plasma as inhomogeneous media.

3.5.2 Near & Far Fields

The space surrounding an antenna is usually subdivided into three regions: reactive near field, radiating near field (Fresnel) and far field (Fraunhofer) regions [4].

The outer boundary of reactive near field region is commonly taken to exit at a distance $R < 0.62\sqrt{D^3/\lambda}$ from the antenna surface, where λ is the wavelength and D is the largest dimension of the antenna.

The inner boundary of the Fresnel region is taken to be the distance $R \geq 0.62\sqrt{D^3/\lambda}$ and the outer boundary the distance $R < 2D^2/\lambda$. D must also be large compared to the wavelength ($D > \lambda$). For a very short dipole, a distance $R < \lambda/2\pi$ from the antenna surface is commonly used. This criterion is based on a maximum phase error of $\pi/8$.

The Fraunhofer region is commonly taken to exit at distances greater than $2D/\lambda$ from the antenna. For a very short dipole, the region of distances $R > \lambda/2\pi$ is referred to as the intermediate field region while that for $R \gg \lambda/2\pi$ is referred to as the Fraunhofer region or the far field region.

In this study, the length of antennas is about 1 mm with frequency of 1 GHz. $\lambda/2\pi = 30 \text{ cm} / 6.28 = 4.8 \text{ cm}$. Observation distance in this study is 1 m. The distance is more than ten times bigger than the criterion. Therefore, radiation regime in this study is the far field or Fraunhofer region.

Chapter 4

Code Validation

Before discussing the results of this study, we show the validation and/or verification of the numerical codes with examples. Two numerical codes are being used in this study. First one is the PIC code to analyze radiation with the electron motion information, and the other is hybrid element method code to solve the radiation problems with inhomogeneous dielectrics.

The most important thing for the PIC code is the accuracy of particle motions including positions, velocities and acceleration. We consider ions in the plasma are stationary in the time scale mentioned in previous section 3.4.2. Only electron motions are considered. Various compositions of electric and magnetic fields are tried to check the accuracy of the motions compared to analytic values.

For the hybrid element method code, some examples are already presented in the literature [34, 85]. We here try various two dipole cases to check the possibilities of adopting this code for this study. The results of this validation are compared to analytic solutions.

4.1 Particle-In-Cell Analysis

This PIC code uses the Lorentz force equation (2.1) to take the information of the charged particle motions. We test three cases with electric and magnetic fields to check the accuracy of the code and compare the result to the analytic calculations.

4.1.1 Constant Magnetic Field

First, constant magnetic fields are tried for electron trajectories. Electrons in constant magnetic fields have gyration motions with Lamor radii. The electron trajectories are compared to analytically calculated values. 100, 500, and 1550 G magnetic fields are used for magnetic fields, and 1 and 10 eV for velocities. From (2.16) the Lamor radius is proportional to the ratio of the magnetic field and perpendicular speed.

Figure 4.1 shows the trajectories and the fast Fourier transforms of the velocities and acceleration from the code. Analytic calculations (\square) are also shown on the trajectories. In all cases, the Lamor radius of the charge motion from the code have a good agreement with analytic calculations with less than 1% deviation.

Table 4.1: Lamor radius [mm] (from Figure 4.1 / analytic)

Te (eV)	magnetic field (G)		
	100	500	1550
1	0.3372 / 0.3372	0.0675 / 0.0674	0.0220 / 0.0218
10	1.0664 / 1.0664	0.2135 / 0.2133	0.0694 / 0.0688

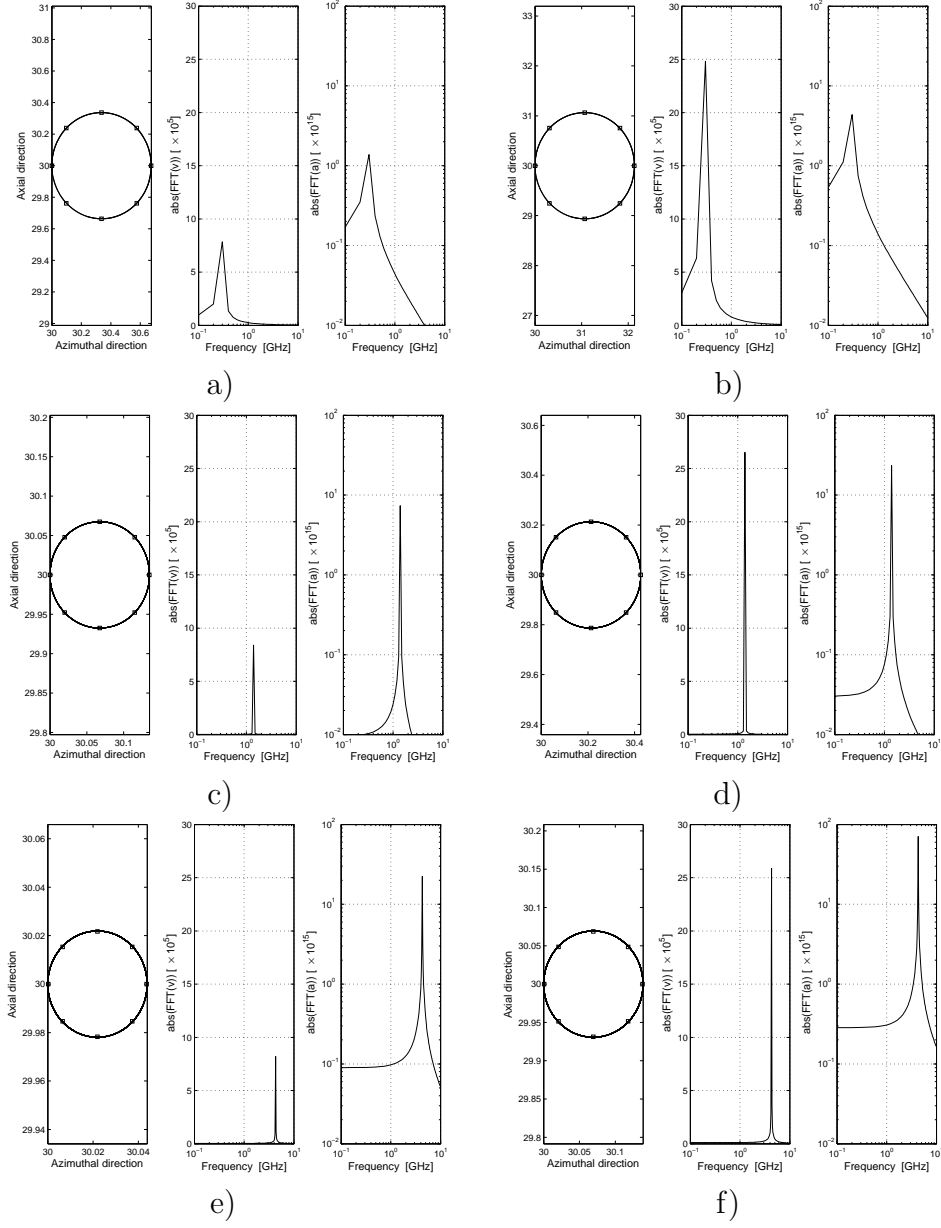


Figure 4.1: Gyration motions in magnetic fields. \square is analytic results. a) $B = 100$ G and $T_e = 1$ eV b) $B = 100$ G and $T_e = 10$ eV c) $B = 500$ G and $T_e = 1$ eV d) $B = 500$ G and $T_e = 10$ eV e) $B = 1550$ G and $T_e = 1$ eV f) $B = 1550$ G and $T_e = 10$ eV

The electron cyclotron frequencies depend on the magnetic fields. The frequencies associated with magnetic fields of 100, 500, and 1550 G are 0.2799, 1.3996, and 4.3388 GHz, respectively. The electron cyclotron frequencies in Figure 4.1 are 0.3, 1.4, and 4.3 GHz, respectively. In this study, the resolution in frequency domain is 100 MHz. Considering the frequency resolution, the results are acceptable. Therefore, the trajectories with constant magnetic field have a good agreement with analytic ones.

4.1.2 $\vec{E} \times \vec{B}$ Drifts

Now let us include electric fields in our analysis. Charged particles have drift motions in crossed electric and magnetic fields. This drift motion is called the $\vec{E} \times \vec{B}$ drift or the guiding center drift. An electron is launched in the space with constant magnetic and electric fields. The electron has zero initial velocity. The electric fields considered in this case are 1 and 10 kV/m in +z direction, and the same magnetic fields as in the previous case are used in +y direction.

From (2.22) the magnitude of the $\vec{E} \times \vec{B}$ drift is the ratio of \vec{E} to \vec{B} , and the direction is perpendicular to both of \vec{E} and \vec{B} . In this case, the drift has to have -v_x direction, and the electron can have only x and z components of velocity due to the +y directional magnetic fields. The drift velocities of 100, 500, and 1550 G magnetic field cases with 1 kV/m electric field will be 1×10^5 , 2×10^4 , 6.45×10^3 m/s, respectively, and those with 10 kV/m electric field will be 10 times bigger.

The electron trajectories and velocity vectors of this result are shown in Figure 4.2. We can see the $\vec{E} \times \vec{B}$ drift in the trajectories in all cases. In the velocity domain, we can see not only the circular velocity vectors but also shifts toward $-v_x$ direction, which is what we expect. The amount of shifts of the cases with 1 kV/m in Figure 4.2 are -1.000×10^5 , -2.000×10^4 , and -6.453×10^3 m/s. The shifts with 10 kV/m are -1.000×10^6 , -2.000×10^5 , and -6.453×10^4 m/s. These values have good agreement with previous analytic calculations.

In Figure 4.2 e) and f), a small drift in the $-z$ direction is evident. The amounts are -8.794×10^1 m/s and -8.794×10^2 m/s, which is 1.4% of the $\vec{E} \times \vec{B}$ drift. This additional drift is also shown in other cases with same value, but the value is fractional compared to the main drift. This phenomenon is due to the sampling time in the code. The additional drift can be eliminated or reduced with smaller sampling time.

4.1.3 ∇B Drifts

Last, the gradient of magnetic fields are considered. Charged particles have drift motions in magnetic fields with gradient. This drift is called the ∇B Drift, (2.31).

We launch an electron at the center of the near exit plane region. There are constant magnetic and electric fields in the channel. The electric field considered in this case is 10 kV/m in $+z$ direction. The same magnetic fields as previous case ones are used as the maximum magnetic field. The maximum

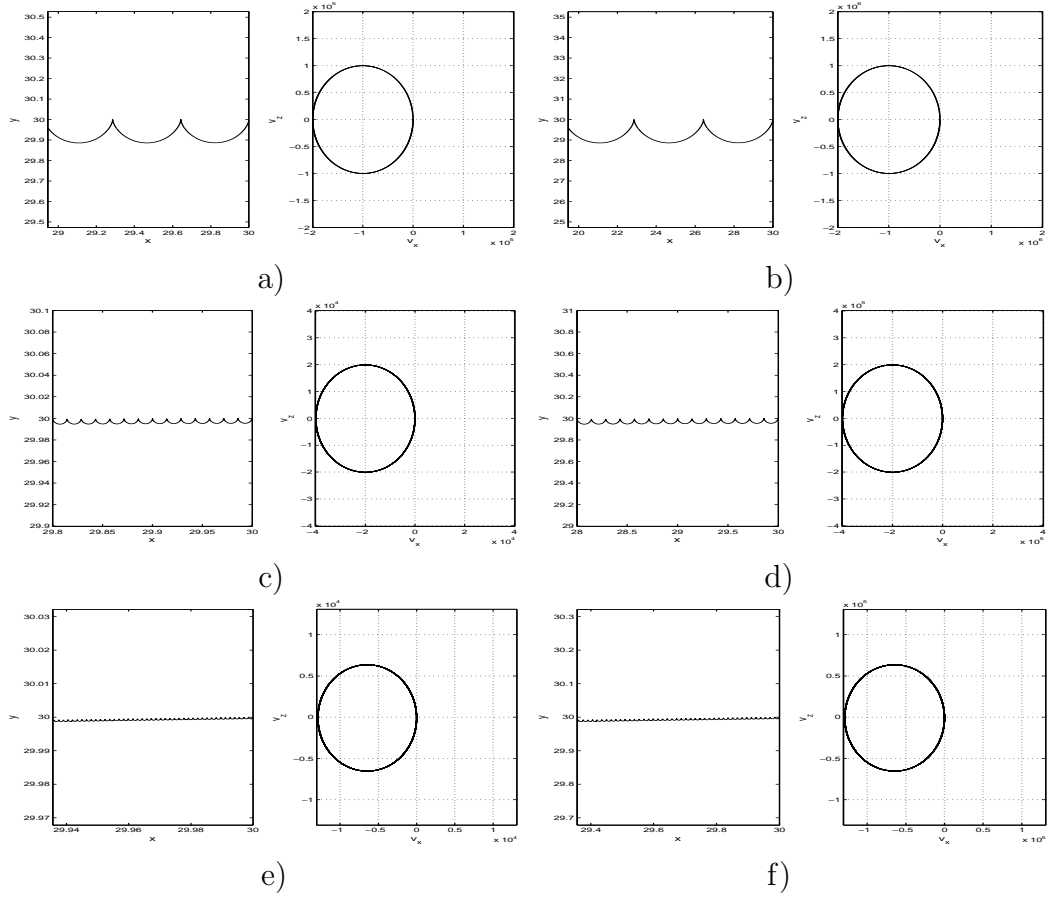


Figure 4.2: $\vec{E} \times \vec{B}$ drifts. a) $B = 100$ G and $E = 1$ kV/m b) $B = 100$ G and $E = 10$ kV/m c) $B = 500$ G and $E = 1$ kV/m d) $B = 500$ G and $E = 10$ kV/m e) $B = 1550$ G and $E = 1$ kV/m f) $B = 1550$ G and $E = 10$ kV/m

magnetic field is occurred at the inner wall. The magnetic field decrease with $1/r$ decay. The relationship is $\vec{B} = B_o \cdot 35/r$. The magnetic field is in the radial direction.

We try three electron temperatures, 4, 8 and 12 eV. Every condition for this try is similar to the analysis conditions in this study. However, time scale, especially total sampling period, has to be changed to see the results. The total sampling periods of 5×10^{-7} sec, 12.5×10^{-7} sec and 50×10^{-7} sec for the magnetic fields of 100 G, 500 G and 1550 G, respectively.

The results are shown in Figures 4.3, 4.4 and 4.5. Each figure shows the variation of the electron motion with respect to the electron temperature. It also shows the Fourier transform of the electron velocity (the third column) and acceleration (the last column). Figure 4.3 shows the 100 G cases. The 4 eV electron cannot reach the inner wall, never goes back to the center position and goes through the outer surface region. The 8 eV electron reaches back to the center position but cannot reach the inner wall either. Both of these two cases show the magnetic mirror effect. The 12 eV electron can reach the inner wall and goes back and forth between inner and outer walls. In the 500 G cases, Figure 4.4, all electrons cannot reach the inner wall. Figure 4.5, the 1550 G cases, shows the same trend.

The $E \times B$ drift is also shown in the Figures. Although the duration time of Figure 4.4 is 2.5 times longer than the time of Figure 4.3, the movement along the azimuthal direction is approximately half of the case of Figure 4.3. Because the magnetic field is five times greater than the magnetic field of

Figure 4.3. Figure 4.5 shows the same trend.

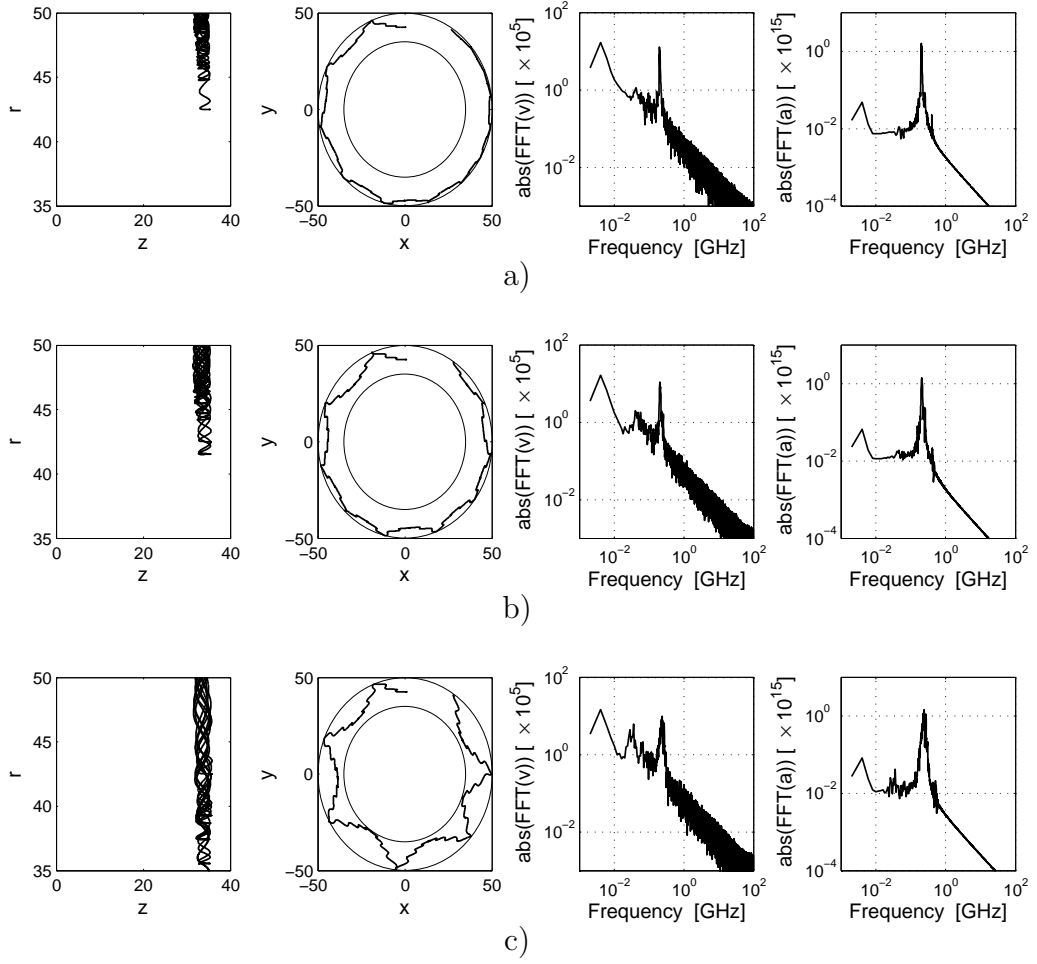


Figure 4.3: ∇B drift with the electric field of 10 kV/m and the magnetic field $\vec{B} = 100G \cdot 35/r\hat{r}$. a) 4 eV b) 8 eV c) 12 eV

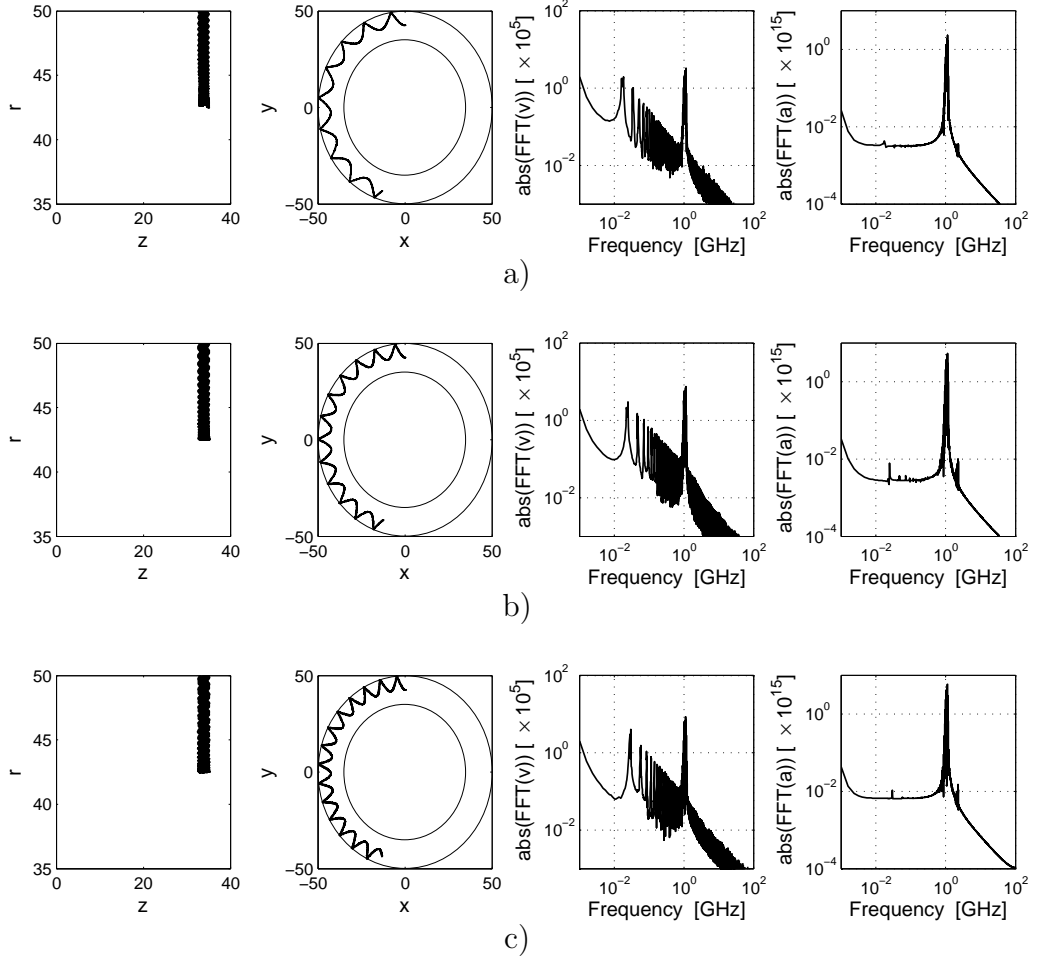


Figure 4.4: ∇B drift with the electric field of 10 kV/m and the magnetic field $\vec{B} = 500G \cdot 35/r\hat{r}$. a) 4 eV b) 8 eV c) 12 eV

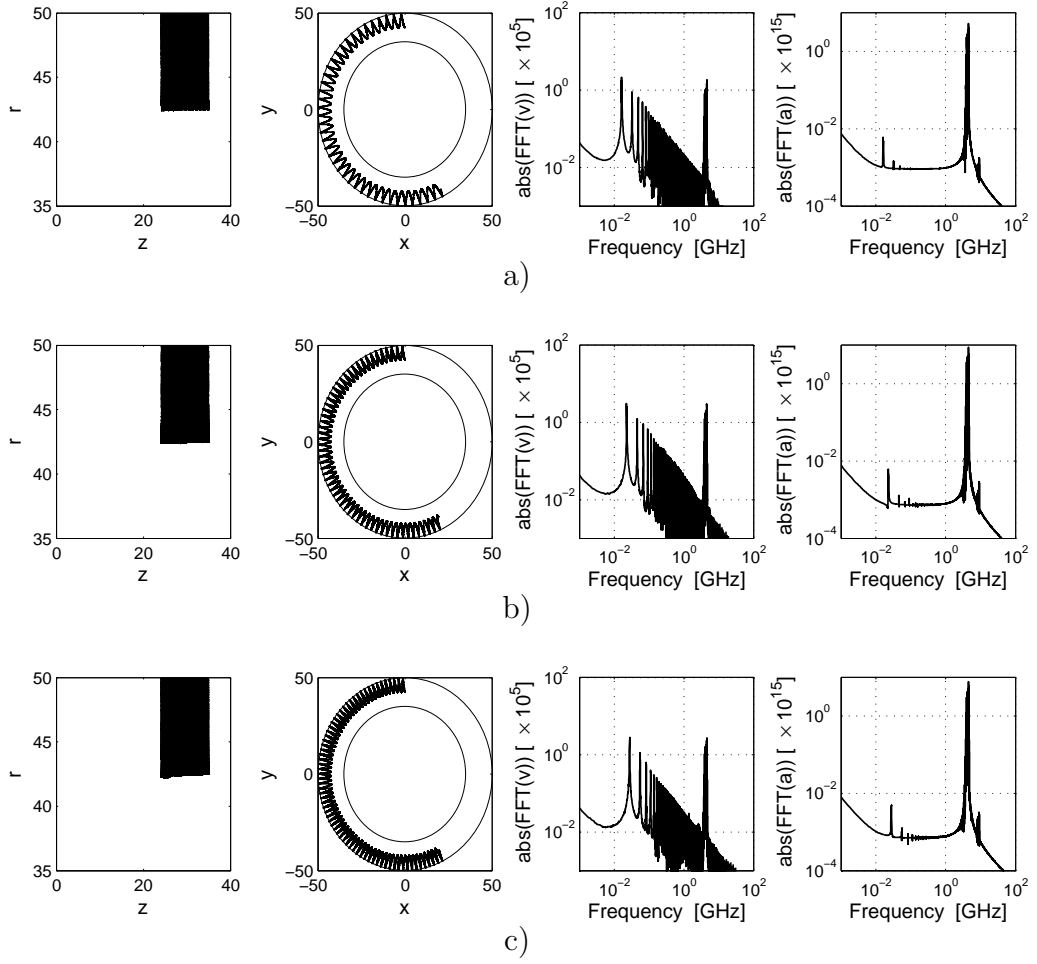


Figure 4.5: ∇B drift with the electric field of 10 kV/m and the magnetic field $\vec{B} = 1550G \cdot 35/r\hat{r}$. a) 4 eV b) 8 eV c) 12 eV

4.2 Hybrid Moment Method

EMAP5 is a full-wave electromagnetic field solver that combines the method of moments with a vector finite element method [25]. The FEM is employed to handle the interior domain of inhomogeneous dielectric bodies. The method of moments is used to develop surface integrals that relate the field quantities on boundary surfaces with the equivalent surface currents. These integral equations are then coupled to the finite element equations through the continuity of the tangential magnetic fields [34]. EMAP5 allows only for the Cartesian coordinates.

The code validity of EMAP5 is already shown in many papers [2, 34, 39, 81, 85, 86]. Here, the validity of EMAP5 for this study is checked with several cases.

4.2.1 Two Dipoles

The cyclotron motion of charged particles can be modeled with two dipoles 90° out of phase. Two in phase dipoles make another tilted dipole. Two sets of the code run are used for the case of 90° phase difference.

The electric field radiation pattern of the two in phase dipoles is shown in Figures 4.6 a) and 4.7 a). The pattern looks like the pattern from a dipole tilted 45° . Figures 4.6 b) and 4.7 b) show the electric field pattern from two dipoles 90° out of phase. This pattern is same as the radiation pattern of a charged particle with cyclotron motion.

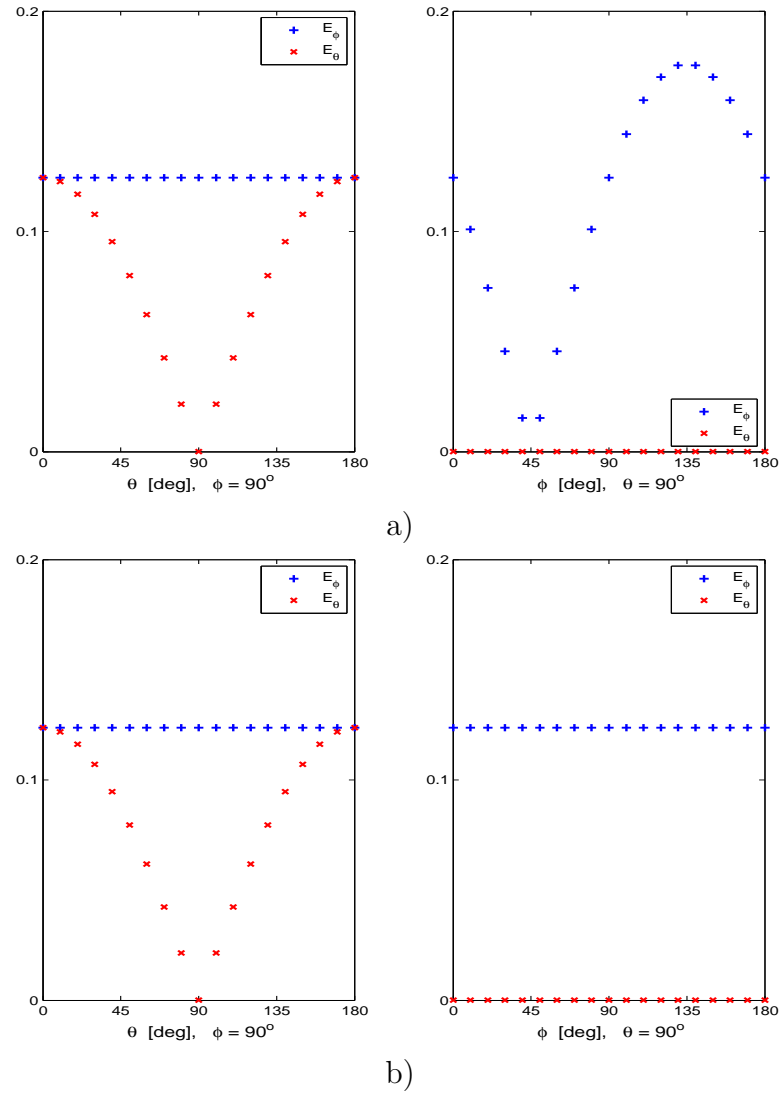


Figure 4.6: Radiation pattern of electric field a) from the linear sum of 2 dipoles b) from 2 dipoles with 90° phase difference.

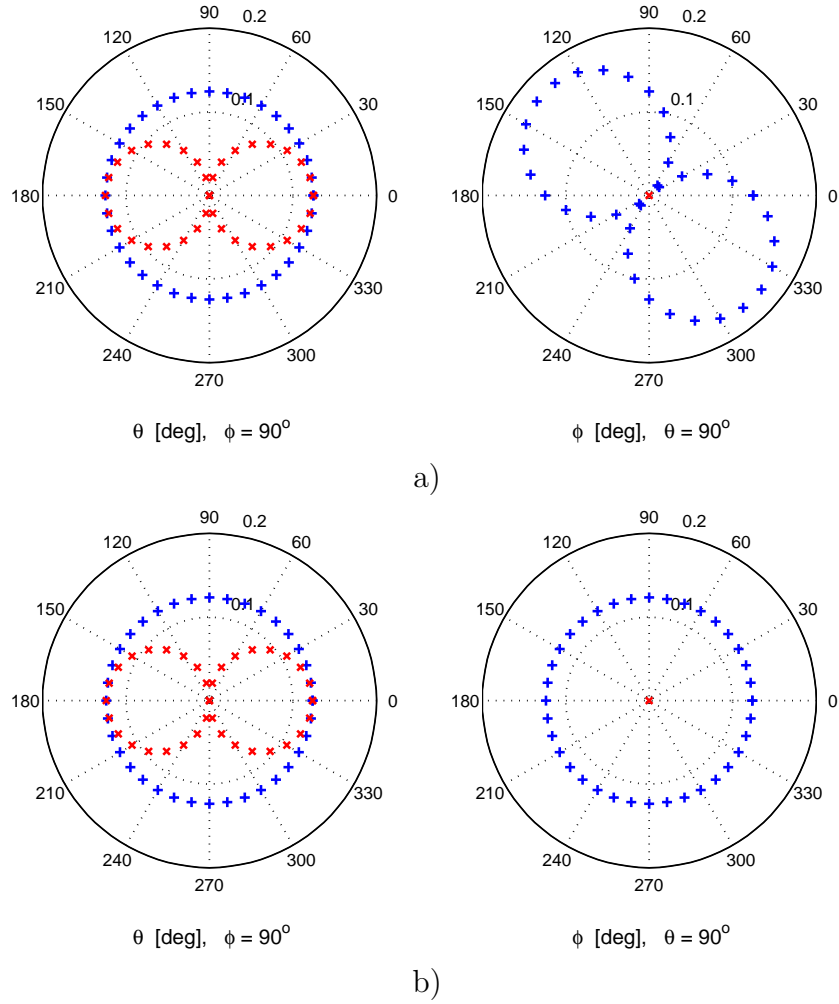


Figure 4.7: Radiation pattern of electric fields in the polar coordinates, $E_\phi(+)$ and $E_\theta(\times)$, a) from the linear sum of 2 dipoles b) from 2 dipoles with 90° phase difference.

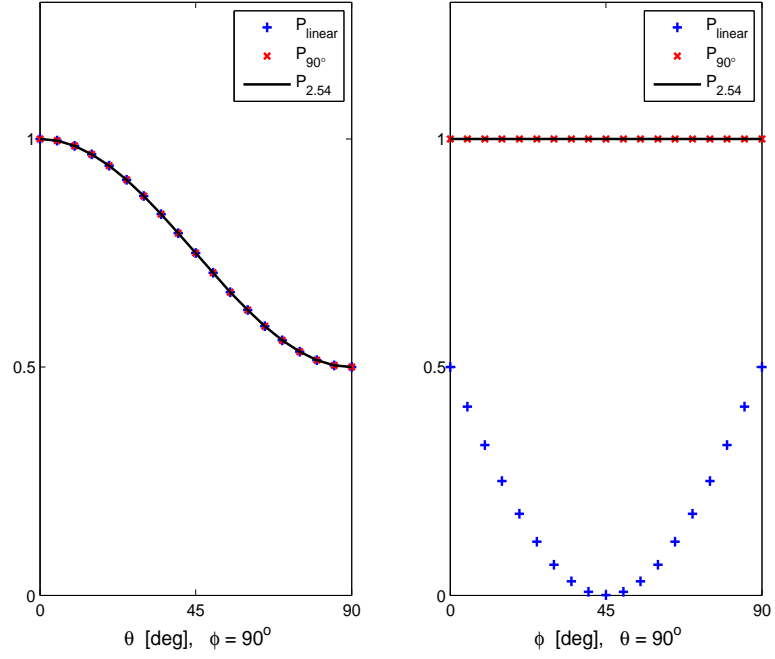


Figure 4.8: Radiation pattern of power from 2 dipoles.

The power radiation patterns are shown in Figure 4.8. Equation (2.55) is used to compare both of radiation patterns of in and out of phase. The power radiation pattern of two dipoles 90° out of phase is also the same as the analytic one.

4.2.2 Modified Length of Infinitesimal Dipoles

The radiation of an infinitesimal dipole is proportional to the current on and the length of the dipole. The multiplication of the current and length acts as a constant not only in the far field range but also in the intermediate range. If it is possible to trade off between the amount of current on the dipole

and the length of the dipole, then we can reduce the number of elements and the calculation time in this analysis with EMAP5. We check the validity of this approach in this section.

We compare three cases: original length from Lamor radius, fixed modified length to 1 mm, and analytic solution. Frequencies, f , used in this section are 5.6, 1.4, and 0.28 GHz. In the original cases, the lengths of dipoles, l , are 0.034, 0.108, 0.128, 0.472, 0.680, 2.4 mm, and the current is assumed to be 1 A. In the modified length cases, the length is assumed to be constant, 1 mm, then the current is 0.034, 0.108, 0.128, 0.472, 0.680, 2.4 A. Same frequencies are used. Frequencies and lengths of the original ones are used in the analytic calculations. The intermediate field formula for infinitesimal dipoles [4] is used for the calculation.

The results are shown in Figure 4.9. The modified cases have good agreement with analytic ones in the range between 0.5 and 2.4 mm of the length. In the other ranges, from 34 to 128 μm , the electric field radiation patterns still agree with analytic ones. The difference of the length is up to about 30 times, but the error is less than 1 % for the range of 34 to 128 μm .

We try another case with two dipoles of the 1 mm length. One is on the x axis, and the other is on the y axis. There is no physical variation; the positions and the length are fixed. The only currents on the dipoles are adjusted to make the angles that we want. Figure 4.10 shows that we can generate not only dipoles on the axis but also fictitious dipoles with angles of θ and ϕ . These results show that this approach is valid for this study.

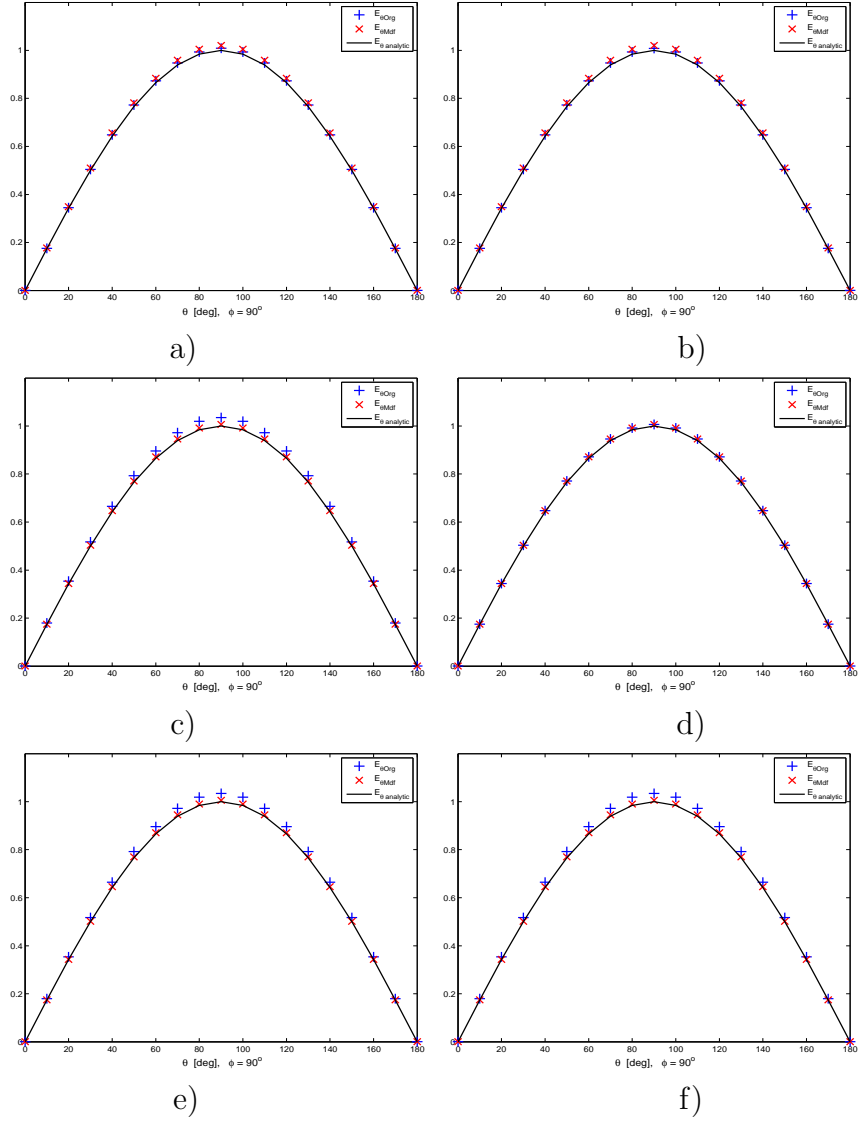


Figure 4.9: Radiation patterns of a dipole with original length and current (+), fixed length of 1 mm and compromised current (\times), and analytic calculation ($-$). a) $f = 0.28$ GHz, $l = 0.68$ mm b) $f = 0.28$ GHz, $l = 2.4$ mm c) $f = 1.4$ GHz, $l = 128 \mu\text{m}$ d) $f = 1.4$ GHz, $l = 472 \mu\text{m}$ e) $f = 5.6$ GHz, $l = 34 \mu\text{m}$ f) $f = 5.6$ GHz, $l = 108 \mu\text{m}$

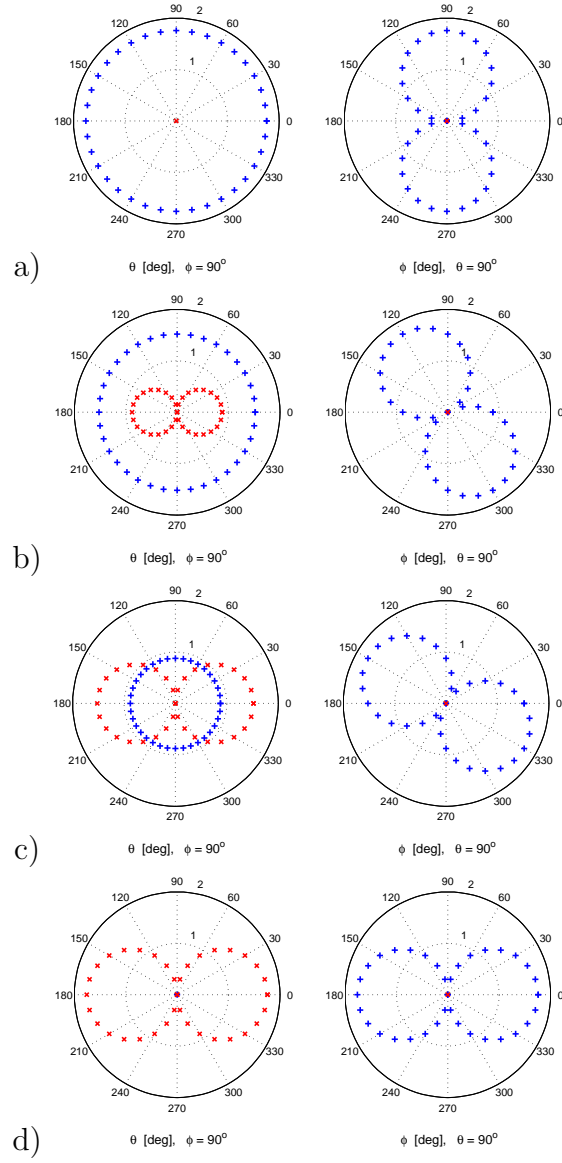


Figure 4.10: Radiation patterns with two dipoles. The currents are a) $x - 1$ A, $y - 0$ A, $\phi = 0^\circ$ b) $x - 0.866$ A, $y - 0.5$ A, $\phi = 30^\circ$ c) $x - 0.5$ A, $y - 0.866$ A, $\phi = 60^\circ$ d) $x - 0$ A, $y - 1$ A, $\phi = 90^\circ$

Chapter 5

Results

This thesis describes the numerical simulation of the ECE radiation from SPT100 class, 1.35 kW, and BPT-4000 class, 5 kW, Hall thrusters. We analyze the radiation with three methods: the single particle approximation analysis, the Particle-In-Cell/Monte Carlo analysis, and the hybrid element method analysis. We use the plasma parameter models developed in Chapter 3 for the magnetic field, electron temperature and electron density distributions. The same parameter distributions are used for all of the approaches.

The first method is the single particle approximation analysis. This is the simplest one among the approaches. We assume that the plasma parameters are constant in a cell. We plug the parameter distributions into a formula of the ECE radiation and calculate the radiation according to the observation angle. The ECE radiation formula is derived with the single particle assumption. The frequency of a cell is determined by the magnetic field of the cell. This analysis is easy to approach and does not require a high computing performance. The formula used in this analysis is radiated power per steradian. The radiated electric field is derived from the power, so there is no polarization information on the electric field.

The next method is the Particle-In-Cell (PIC) analysis. This approach is from the fundamental definition of radiation, i.e., the radiation is from charge acceleration. PIC is for analysis of microscopic phenomena. Particle motions in the thruster channel region are simulated with the PIC method. We select electrons from the Maxwell-Boltzmann distribution for the speed of electrons. The Monte Carlo method is used in the electron selection. We spread the selected electrons in the channel region and solve the Lorentz force equation to get the motion data of the electrons. The radiated electric field is obtained from the particle motions. Then, we take the Fourier transform of the electric field to see the radiation in the frequency domain. This is more realistic approach to the plasma. The parameters in a cell are not constant because of adopting the Monte Carlo method. It shows detailed results of the radiation. In this analysis, we assume that the radiation is in free space. The channel plasma is considered as current sources for radiation. The material constants of the plasma is considered as free space.

The last approach adopted is to consider the non free space and inhomogeneous media. Plasmas in Hall thrusters are generally not well modeled as free space. A new approach of the ECE analysis is introduced. The hybrid FEM/MoM (hybrid element method) suggested in many papers [34, 39, 47, 88] is adopted to solve the problem of radiation in the non free space and inhomogeneous media. The hybrid element method is to exploit advantages of FEM and MoM and to compensate their disadvantages. In this analysis, the plasma is considered as a dielectric, and the source currents are from the

plasma parameters.

We compare the numerical results to experimental data [16, 43] and also compare the results of all approaches to each other.

The configuration we consider has an annular plasma region where the origin of the coordinate system is the origin of the annular plasma. This means the analysis configuration has circular symmetry. Not only the cylindrical coordinates, but also Cartesian coordinates are defined. The Hall thruster axis is aligned with the z-axis for both the cylindrical and Cartesian coordinates. The line from the center of the Hall thruster to the fixed observation point, OB, is defined as the x-axis. We assume that the distance from the origin to the observer point in the r-z plane is 1 m , which is the same distance as the experiment.

Dimensions of the plasma annular region of the BPT-4000 class Hall thruster are inner radius $r_I = 5$ cm, length $L = 4$ cm and width of the plasma region $w = 2$ cm. Dimensions of the SPT100 class Hall thrusters used in papers are slightly different [13, 14, 22, 23, 87]. In this study, 100 mm outer diameter, 60 mm inner diameter, and 40 mm length are chosen as dimensions for this analysis; $r_I = 3$ cm, $L = 4$ cm and $w = 2$ cm.

5.1 Single Particle Approximation Results

The computation configuration to study the ECE radiation of the Hall thruster is shown in Figure 5.1. The dark rectangle in the configuration is the computation region. We assume that all parameters are constant in a cell. We compare the results from the 1D and 2D models to the experimental data [16, 43].

In this study, (2.55) is used with the model parameters to calculate the radiation power from each cell. The power from each cell is summed to give the total power flux at each angle. The angle between the observer point and the radial axis is varied from 0 to 90° to obtain the power about the observation angle. The power from the cells is also divided according to the frequency of the cells and summed to consider the total power radiation over the entire frequency domain. After that, the electric field on the frequency domain at the observation point is given by

$$P = \frac{1}{\eta_0} E^2 \quad (5.1)$$

The electric field shown in the results is in units of dB $\mu\text{V}/\text{m}$ given by

$$20 \log_{10}(E \times 10^6) = 20 (\log_{10} E + 6) \quad (5.2)$$

where E is in V/m .

First, the 1D analysis is performed to verify the validity and the limits of the 1D model. After that, this analysis is expanded to the 2D configuration with the 2D model to verify the validity and the improvement of the 2D model. This analysis is implemented with Matlab.

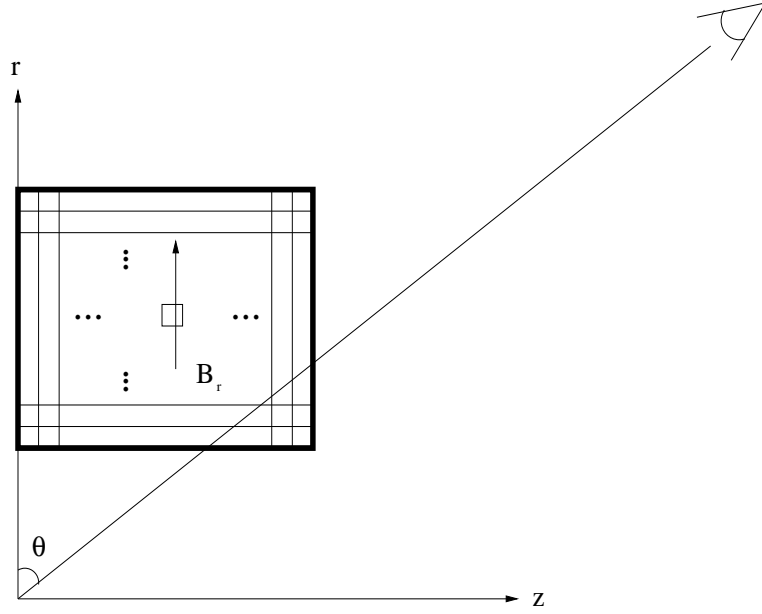


Figure 5.1: Hall Thruster computation configuration.

5.1.1 BPT-4000 Class

5.1.1.1 1D Results

In the 1-D analysis, the parameters are varied only along the axial direction. The shape of each cell is a thin annular ring with w width. The size of the system we consider is much smaller than the distance to the observer: $w = 2$ cm, $r_I = 5$ cm and $L = 4$ cm. Therefore, the observation angle of the closest part of the cell is approximately the same as the angle of the furthest part of the cell. We assume that the radiation from each annular cell is from the center of the annular cell on the axial axis. The schematic diagram for the 1-D analysis is shown in Figure 5.2. The angle from the center of the cell to the observer is different from the observation angle from the origin. The

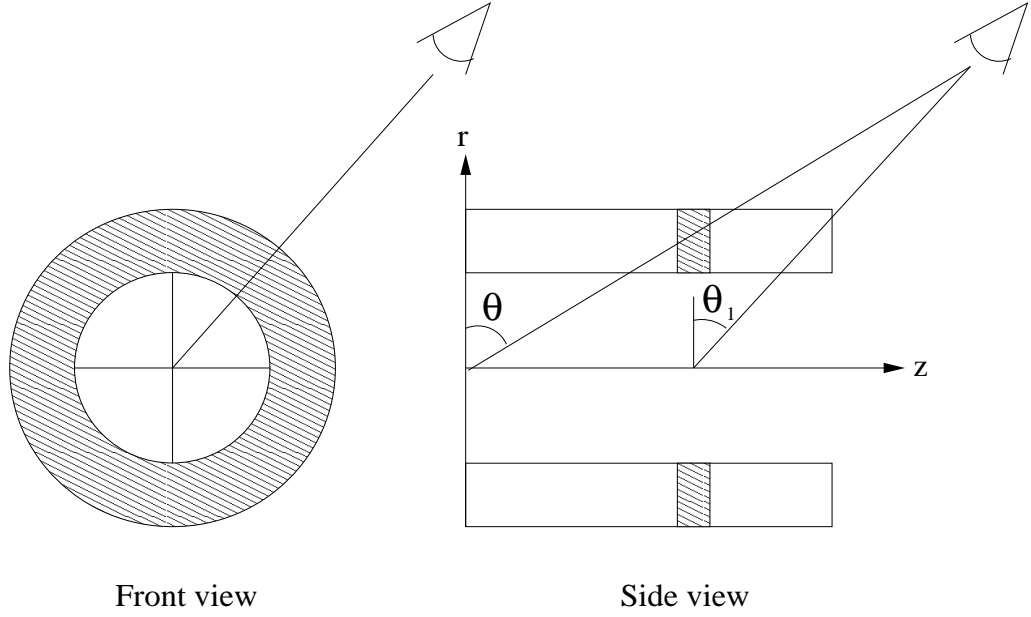


Figure 5.2: Hall Thruster 1D computation configuration.

observation angle is θ , and the angle of the radiated power and field is θ_1 . The observation angle θ is used in Figure 5.3, and the angle of the radiated power is used in calculation of the radiated power. In this study, we assumed that the distance from the cell to the observer is the same as the distance from the origin, 1 m .

The total power flux at each angle with the 1-D model of the parameters is shown in Figure 5.3. The angular trend is in good agreement with the literature for cyclotron radiation [6]. About twice as much radiation is emitted per unit solid angle along the direction of the magnetic field ($\theta = 0$) as perpendicular it. When $\theta = 0$ the wave from the electron gyration due to the magnetic field is circularly polarized, and at $\theta = \pi/2$ it is linearly polarized at

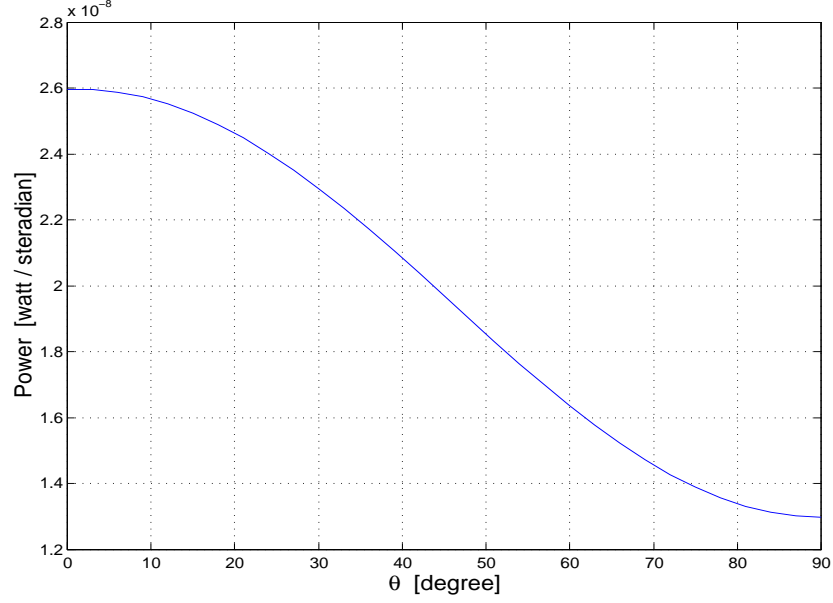


Figure 5.3: Power per steradian as a function of angle calculated from thruster axis in the 1D model (all frequencies).

right angle to the magnetic field. The total power from the magnetized plasma in the channel is $0.141 \mu\text{Watt}$.

The electric field as a function of frequency is shown in Figure 5.4. The trend in this figure is that the ECE radiation below 1 GHz is moderate, but the radiation from 1 GHz to 1.4 GHz increases up to 68 dB $\mu\text{V/m}$. Two electric field curves are shown in Figure 5.4. The upper one is the electric field shown at the $\theta = 0$ position of an observer, which is the angle of the strongest emission, and the lower one is at the $\theta = \pi/2$ position, which is the angle of the weakest emission. The difference between two curves is approximately 3 dB $\mu\text{V/m}$. In Figure 5.4, the radiation due to the electron cyclotron emission

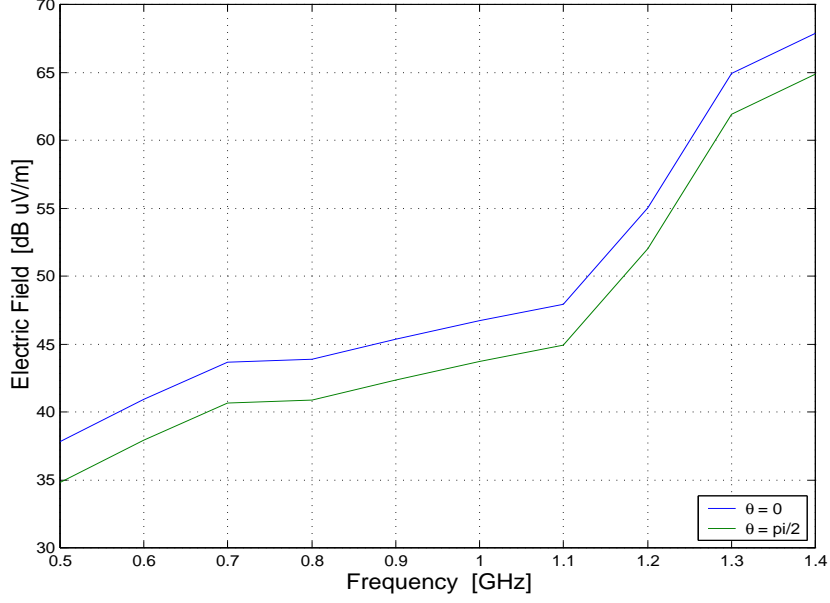


Figure 5.4: Electric field as a function of frequency in the 1D model.

ranges from 500 KHz to 1.4 GHz. Therefore the 1D model is not sufficient to explain the measured ECE radiation above 1.4 GHz.

5.1.1.2 2D Results

In the 2D analysis, the parameters are constant only along the azimuthal direction. The shape of the cell is a thin annular ring like the 1D analysis. However we consider the difference of the angle from the parts on each cell in the 2D analysis. Each annular cell is divided into 36 parts (10°) along the azimuthal axis. In this 2D model, the parameters are not varied along the azimuthal axis, but the radiation power flux is changed along the azimuthal direction in each cell to the observation point. This 2D analysis

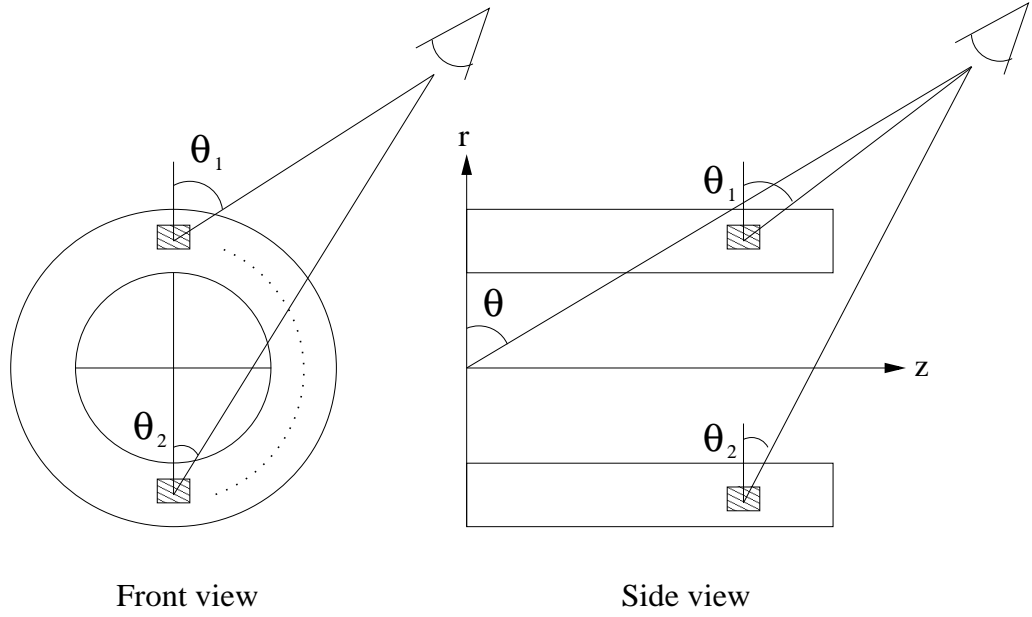


Figure 5.5: Hall Thruster 2D computation configuration.

scheme is shown in Figure 5.5.

In Figure 5.5, θ is the observation angle, and θ_1 and θ_2 are the angles from each cell. The angle from the cell to the observer is different from each other even in the same annular cell (θ_1 and θ_2). This difference is considered in the 2-D analysis. Because the geometry of the system is small compare to the distance, 1 m, the distance from the cell in the case of the θ_1 and θ_2 to the observer is approximately same as each other and as the distance from the origin. In this study we also assume that every distance is 1 m. The configuration and dimensions of the system are the same as the 1D analysis.

The total power flux at each angle with the 2D model of the parameters is shown in Figure 5.6. The angular trend is also in good agreement with theory

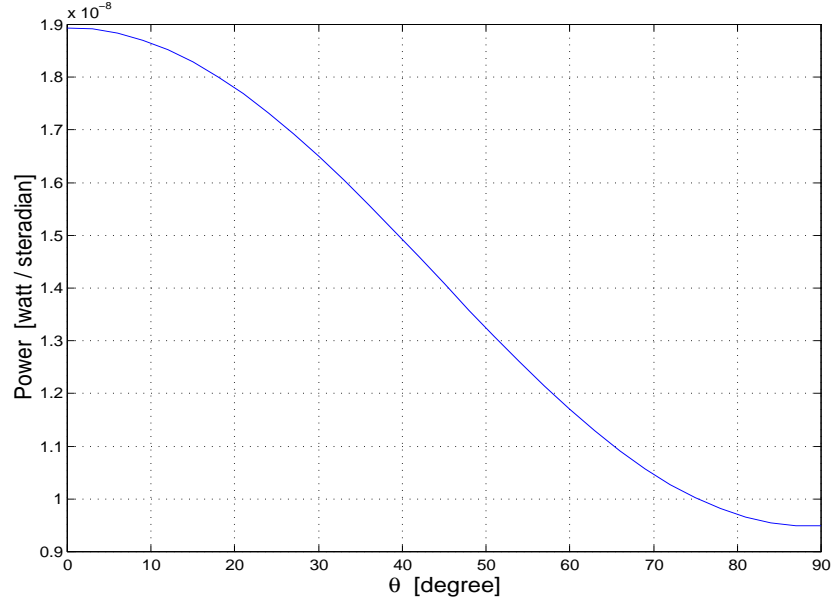


Figure 5.6: Power per steradian as a function of angle calculated from thruster axis in the 2D model of the BPT-4000 class Hall thruster (all frequencies).

[6]. However the maximum value is less than the 1D analysis case. The off-center line electron temperature and electron density are reduced compared to the 1D model. The radial profiles at the center line are the same as the profiles at the wall in the 1D model. In the 2D model the profiles at the center line are decreased linearly, for the electron temperature, or quadratically, for the electron density. In the case of the magnetic field density the profile is increased at the wall, but the major part of the channel region has almost the same magnetic field density profile as the 1D model. This explains the decrease in power.

Integrating Figure 5.6 gives a total radiated power of $0.103 \mu\text{Watt}$.

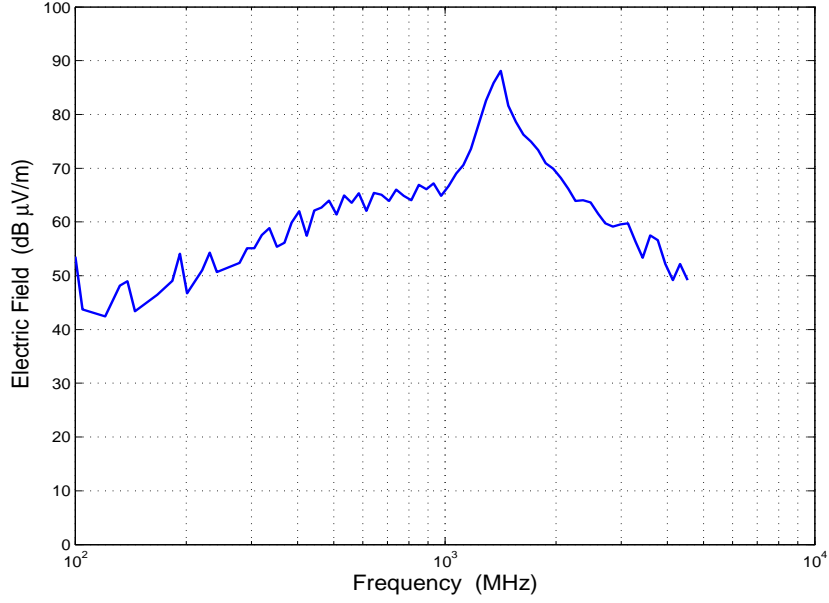


Figure 5.7: Electric field as a function of frequency in the 2D model of the BPT-4000 class Hall thruster.

The ECE radiation power from the channel plasma seems small. However, in satellite communications, the space loss is about 200 dB. Assume that the earth station transmitter and satellite receiver gains are 50 dB and 40 dB, respectively, and the transmitting power is 100 kW, 50 dBW, which are typical. The receiving signal power with these condition is 1 μ Watt. The ECE radiation power is about 10% of the receiving signal power, which is significant.

The electric field as a function of frequency is shown in Figure 5.7. Below 1 GHz the ECE radiation is moderate, less than 60 dB μ V/m. The radiation from 1 GHz to 2 GHz increases to about 87 dB μ V/m with a strong peak. Radiation also now occurs at frequencies from 2 GHz to 4 GHz. In

the 1D case the maximum frequency of the radiated field is 1.4 GHz. The increased frequency range of the radiation is due to the magnetic field density distribution. The 2D model has a higher magnetic field density profile near the walls. The higher magnetic field causes the radiation frequency range to broaden. Thus a more sophisticated magnetic field analysis of the Hall thruster is necessary to obtain the more accurate radiation frequency range.

5.1.1.3 Comparison to Experiment

The experimental measurement data of the BPT-4000 Hall thruster emission are shown in Figures 5.8 and 5.9, as given in [43]. Figures 5.8 and 5.9 are the vertically and horizontally polarized emissions, respectively, and are measured at $\theta = 0$ in the simulation coordinates. In the figures the strong radiation from about 1 GHz to about 4 GHz is identified as the ECE radiation. The radiation profile of the different polarizations is not the same. In Figure 5.8 there is a dominant maximum peak at about 1.2 GHz. The amplitude of the peak is 77 dB $\mu\text{V}/\text{m}$ including the background emission. Harmonics are clearly recognized up to 8 GHz in the vertical polarization measurements.

In Figure 5.9 strong emissions are observed at about 1.2 GHz and 2.5 GHz. The frequency of the second peak is approximately twice that of the first, and both peaks are broad. The third and forth harmonics can barely be found at around 3 and 4 GHz. It is difficult to observe any harmonics above 4 GHz in the horizontally polarized measurement. The amplitudes of the maximum peak and the second peak including the background emission

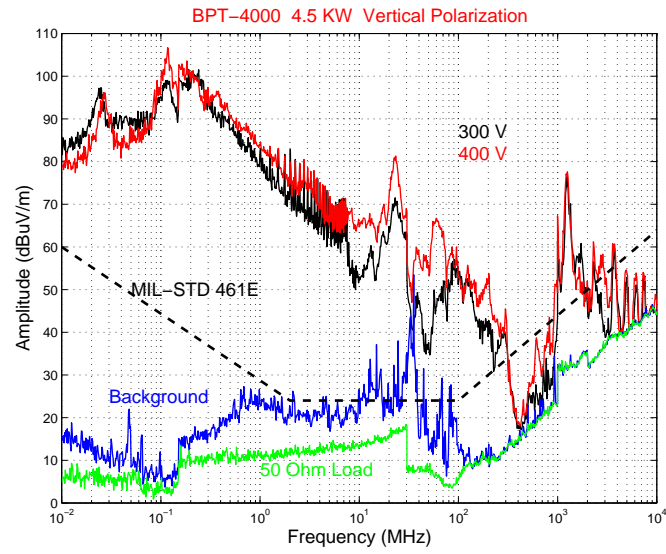


Figure 5.8: Vertically polarized emission spectrum from ref. [43]

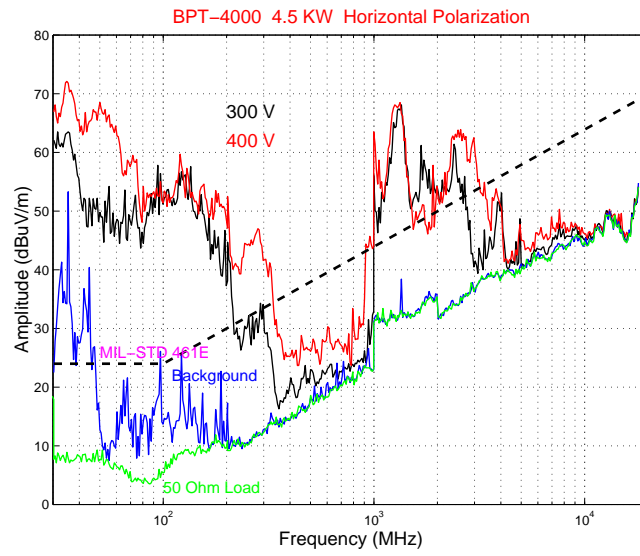


Figure 5.9: Horizontally polarized emission spectrum from ref. [43]

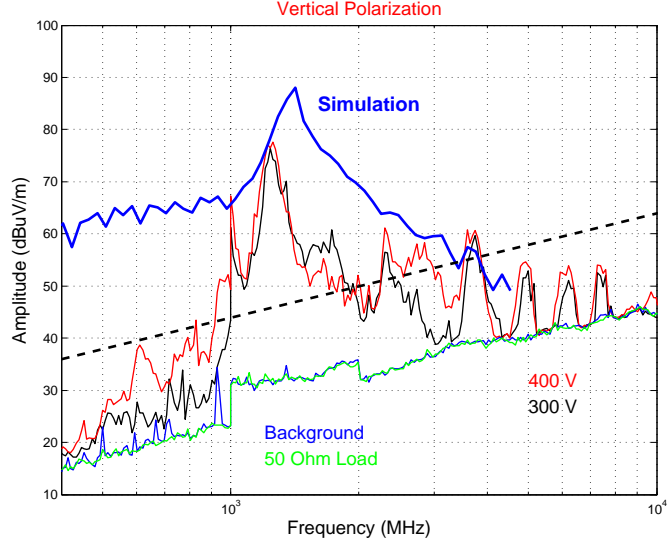


Figure 5.10: Comparison of the simulation result ($\theta = 0^\circ$) to the measured data with background (vertical polarization).

are 68 and 64 dB $\mu\text{V}/\text{m}$, respectively.

Figures 5.10 and 5.11 show the comparison between the experimental data, Figures 5.8 and 5.9, and the 2D analysis results. Because we did not consider polarization in our analysis the simulation results shown in Figure 5.10 and 5.11 are the same. The frequency of the maximum peak of the analysis data is close to the maximum radiation frequency of the measured data. In the simulation, the result that the radiation below 1 GHz range is moderate, and the radiation strongly increases from about 1 GHz to the peak frequency are similar to the measurement data. The radiation decreases after the peak frequency, with measurement and simulation having similar profiles. Our simulation result at the peak is about 10 dB $\mu\text{V}/\text{m}$ greater than the

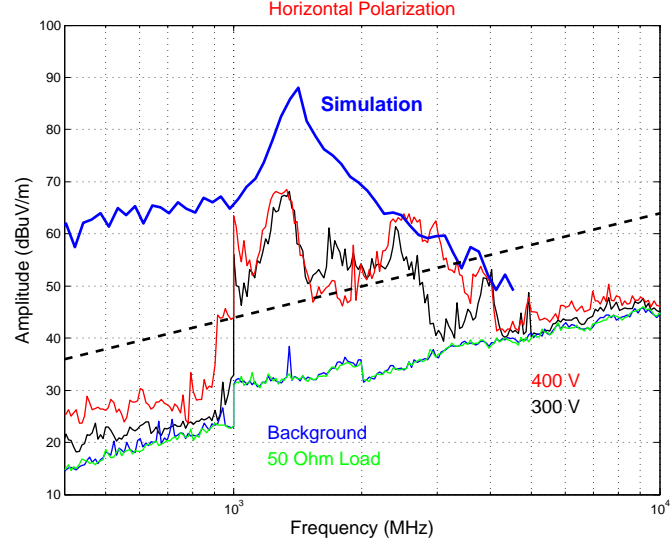


Figure 5.11: Comparison of the simulation result ($\theta = 0^\circ$) to the measured data with background (horizontal polarization).

vertical case of the experimental data, and about 20 dB $\mu\text{V}/\text{m}$ greater than the horizontal case of the experimental data.

Figures 5.12 and 5.13 show the comparison between the 2D analysis results with the experimental data with the background subtracted. To subtract the background, the measurement data is first converted back to $\mu\text{V}/\text{m}$ from dB $\mu\text{V}/\text{m}$. Then the noise is subtracted in an RMS fashion

$$S = \sqrt{M^2 - N^2} \quad (5.3)$$

where S is the desired background-subtracted signal, M is the measurement including noise, and N is the background noise. Comparing Figure 5.10-5.13 shows that subtracting the background has only a small effect.

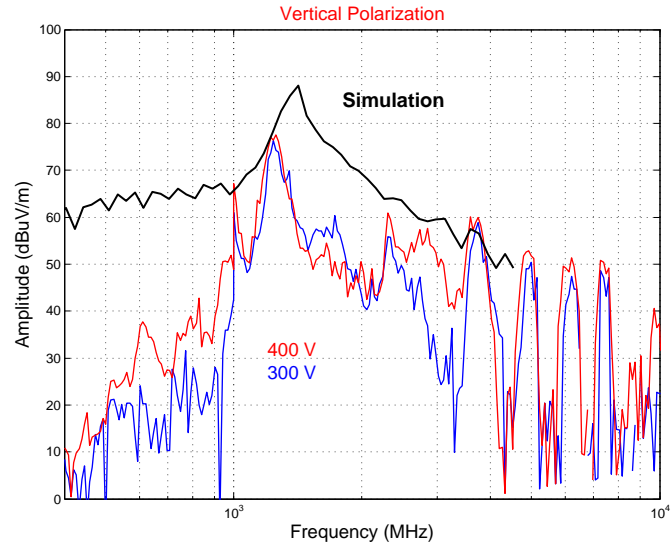


Figure 5.12: Comparison of the simulation result ($\theta = 0^\circ$) to the measured data with background subtracted (vertical polarization).

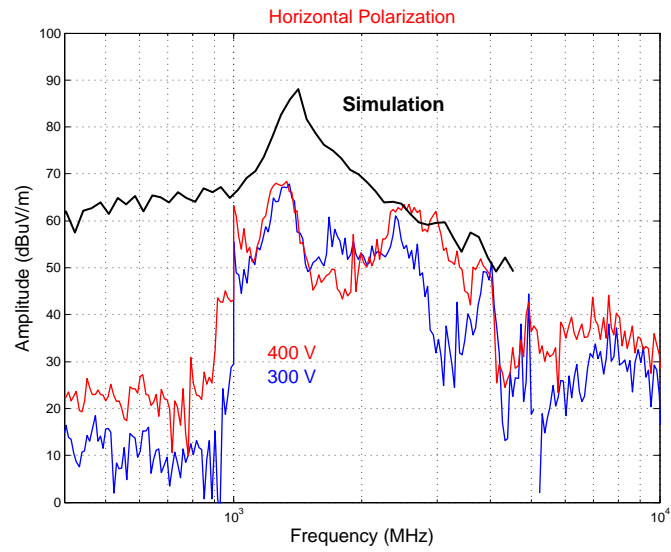


Figure 5.13: Comparison of the simulation result ($\theta = 0^\circ$) to the measured data with background subtracted (horizontal polarization).

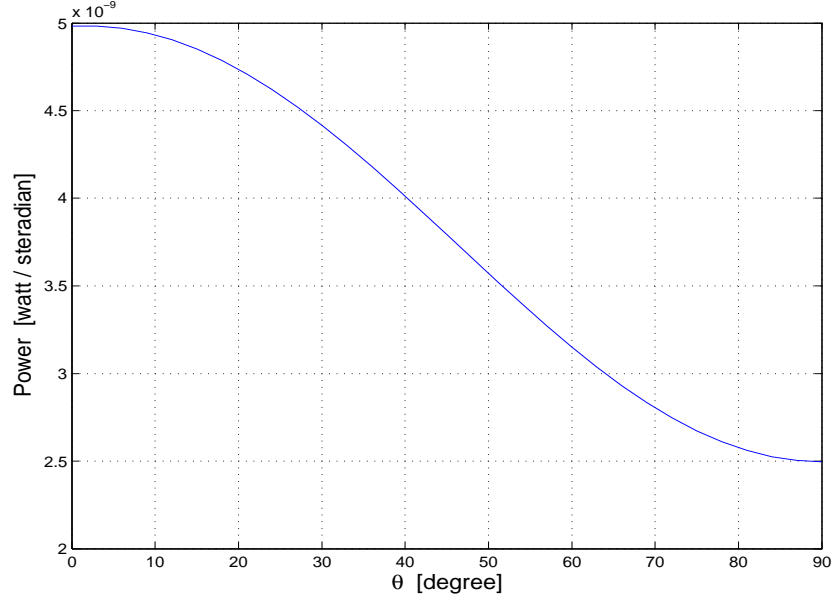


Figure 5.14: Power per steradian as a function of angle calculated from thruster axis in the 2D model of the SPT100 class Hall thruster (all frequencies).

In the experimental data, we can also see the polarization information. We need more sophisticated analysis for this.

5.1.2 SPT100 Class

5.1.2.1 2D Results

As mentioned in previous section, in the 2D analysis, the parameters are constant only along the azimuthal direction, and we consider the difference of the angle from the parts on each cell. This 2D analysis scheme is shown in Figure 5.5.

The total power flux at each angle with the 2D model of the parameters

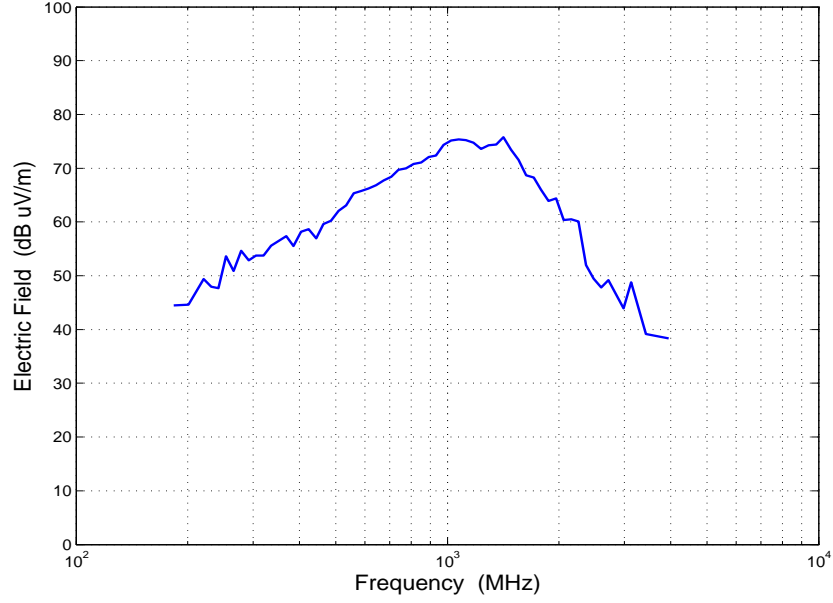


Figure 5.15: Electric field as a function of frequency in the 2D model of the SPT100 class Hall thruster.

is shown in Figure 5.14. The angular trend is also in good agreement with theory [6]. The maximum value is less than the BPT-4000 analysis case. SPT100 is a 1.35 kW Hall thruster model, and BPT-4000 is a 4.5 kW one. The electron density of the SPT100 case is less than that of the BPT4000 case. Although the maximum electron temperature of the SPT100 case is greater than that of the BPT-4000 case, the area in the SPT100 case is much smaller than in the BPT-4000 case.

Integrating Figure 5.14 gives a total radiated power of $0.027 \mu\text{Watt}$. Compared to previous calculation of the satellite receiving signal power, the ECE radiation power is less than 3% of the receiving signal power.

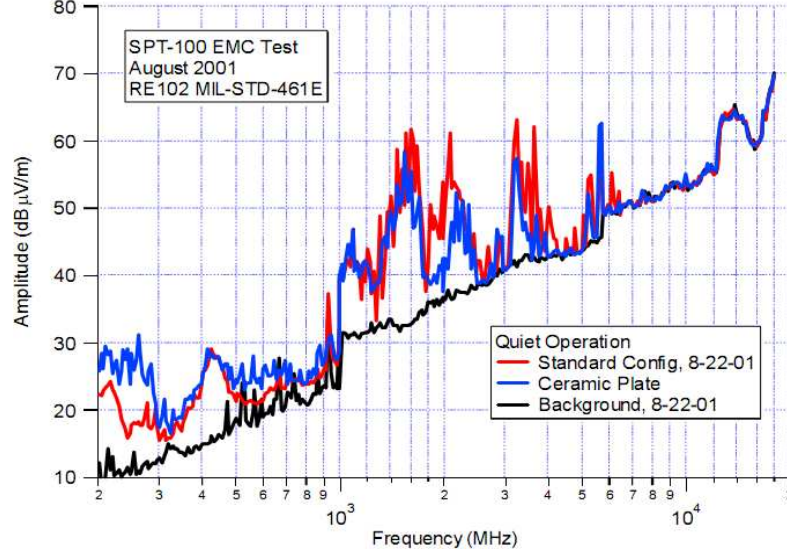


Figure 5.16: Emission spectrum from ref. [16]

The electric field as a function of frequency is shown in Figure 5.15. The radiation is linearly increasing up to the peak frequency 1.4 GHz, then decrease. The radiation from 1 GHz to 2 GHz increases to about $76 \text{ dB } \mu\text{V/m}$ with a smooth peak. Radiation also occurs at frequencies from 2 GHz to 4 GHz.

5.1.2.2 Comparison to Experiment

The experimental measurement data of the SPT100 Hall thruster emission are shown in Figures 5.16 and 5.17, as given in [16]. Figures 5.16 and 5.17 are measurements of emission spectrum with different conditions, and are measured at $\theta = 0$ in the simulation coordinates.

In the figures the strong radiation from about 1 GHz to about 4 GHz is

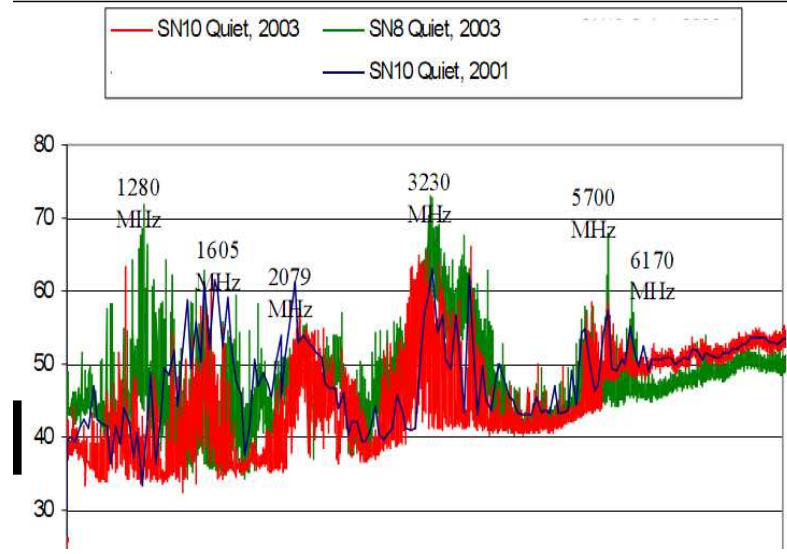


Figure 5.17: Measurement comparison over age and production variation [16]

identified as the ECE radiation. This radiation frequency range is the same as the measurement on BPT-4000 shown in previous section. In Figure 5.16 there is a dominant maximum peak at about 1.6 GHz. The amplitude of the peak including the background emission is 62 dB $\mu\text{V}/\text{m}$ including the background emission. No polarization information is shown in the measurements.

Other strong emissions are observed at about 2.1, 3.3 and 5.5 GHz. Measured frequencies shown in Figure 5.17 are close to these. Harmonic relationships are not clearly recognized except between 1.6 GHz and 3.2 GHz in the figures. The amplitude of the each peak frequency is very similar. A smaller peak is also shown at 1 GHz, and the amplitude is 46 dB $\mu\text{V}/\text{m}$.

Figure 5.18 shows the comparison between the experimental data, Fig-

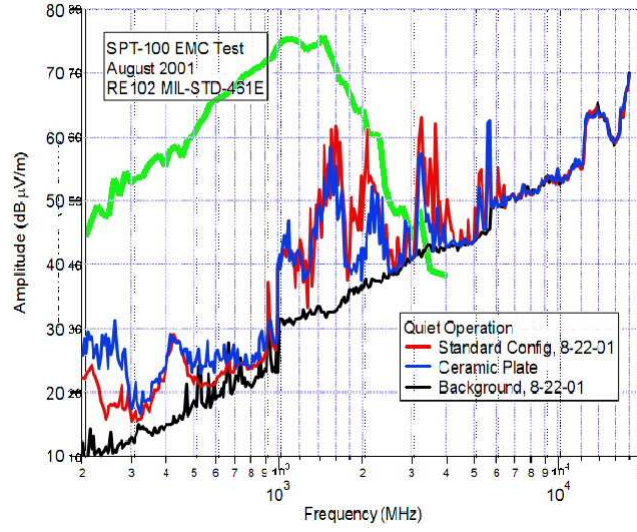


Figure 5.18: Comparison of the simulation result ($\theta = 0^\circ$) to the measured data with background.

ure 5.16, and the 2D analysis results. The frequency of the maximum peak of the analysis data is close to the maximum radiation frequency of the measured data. Our simulation result at the peak is about $15 \text{ dB } \mu\text{V/m}$ greater than the experimental data. The measurement shows sharp increase of the radiation at 1GHz, and the simulation shows smoothe increase to the peak and sharp drop from the peak.

We compare the numerical analysis results of SPT100 to the BPT-4000 measurement background subtracted [43]. Figures 5.19 and 5.20 show the comparison. The BPT-4000 measurement shows the polarization information. Again, we did not consider polarization in this analysis, so the simulation results shown in Figure 5.10 and 5.11 are the same.

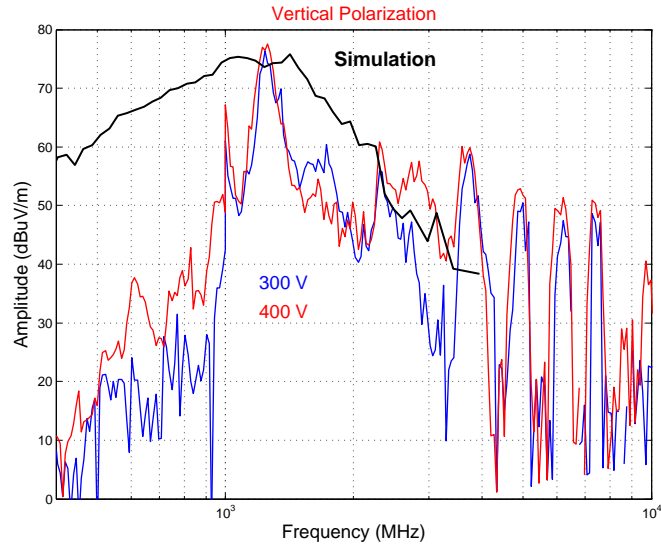


Figure 5.19: Comparison of the simulation result ($\theta = 0^\circ$) to the measured data with background subtracted (vertical polarization).

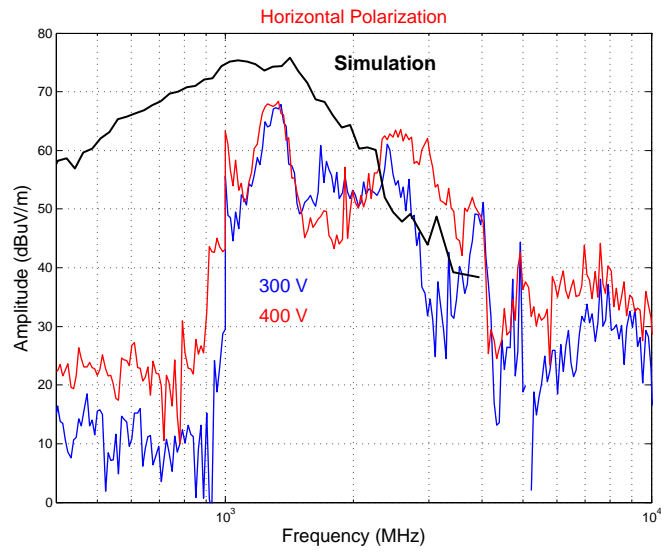


Figure 5.20: Comparison of the simulation result ($\theta = 0^\circ$) to the measured data with background subtracted (horizontal polarization).

5.2 Particle-In-Cell Results

The purpose of the PIC analysis is to get the particle motion information with the plasma parameters. General configurations are the same as the previous section. Not only the cylindrical coordinates, but also Cartesian coordinates are defined. As defined previously, the Hall thruster axis is aligned with the z-axis for both the cylindrical and Cartesian coordinates. The line from the center of the Hall thruster to the fixed observation point, OB, is defined as the x-axis. Therefore, the direction of vertical polarization at OB is the y-axis, and the direction of horizontal one is the z-axis.

Dimensions of the Hall thruster used in this study are same as previous analysis. The computation region is divided by 40 cells in the axial axis and by 20 cells in the radial axis. We assume that all distributions of the plasma parameters are circular symmetric. It does not mean that every electron in an annular cell has same parameters. Even in a cell, electron temperature for each electron can be different because of the Monte Carlo method with the Maxwellian distributions.

Electrons are carefully chosen. First, positions for electrons are randomly generated in the computation region. The positions are initial positions for the analysis. Then, electron temperatures are chosen from the reconstructed electron temperature distribution according to the initial positions, and final initial velocities are selected from the Maxwellian distributions with the electron temperatures. The Monte carlo method is applied at this moment.

Selected electrons are put into the Lorentz force equation solver to get the motion information, i.e. positions, velocities, and acceleration in magnetic and electric fields. Therefore, the fields are updated with new values from the distributions at every time step. As mentioned previously, $5 \times 10^{-12}(\text{s})$ for the time step and 2000 steps, not 2048 steps, are used in this analysis. Then, the frequency resolution is 100 MHz, not 97.7 MHz. The electric fields from the electrons are computed with the motion information, and we take the Fourier transform for a frequency domain analysis.

Results from the analysis are compared to the experimental data [16, 43] and are discussed in the next section.

5.2.1 BPT-4000 Class

5.2.1.1 Numerical Analysis Results

The electric field as a function of frequency is shown in Figure 5.21. The radiation has polarization information with peaks. It shows that the both of polarizations are similar. In the both polarization cases, the peak is up to about 125 dB $\mu\text{V}/\text{m}$. The frequency of the peaks is around 1.3 GHz. The curves in Figure 5.21 are smoother than the curves in Figure 5.7, especially in low frequency region.

5.2.1.2 Comparison to Experiment

The experimental measurement data of the emission [43] was already shown in Figures 5.8 and 5.9, and was described in the section. The experi-

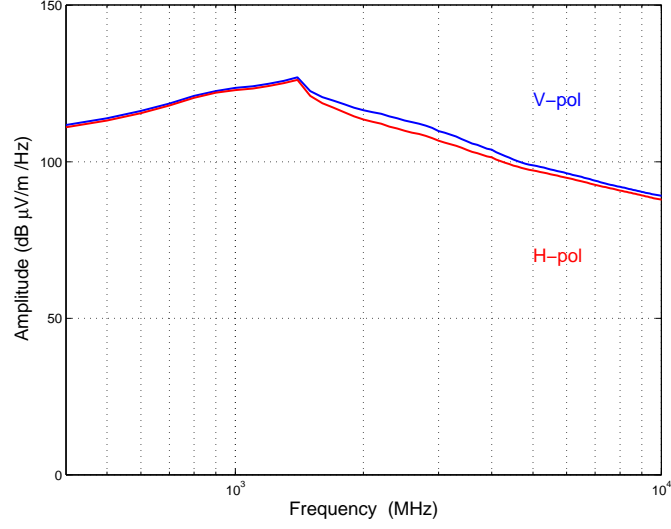


Figure 5.21: Electric field as a function of frequency at the observation point (PIC analysis with the BPT-4000 class Hall thruster).

mental data with the background subtracted shown in Figures 5.12 and 5.13 is used in this comparison.

Figures 5.22 and 5.23 show the comparison between the experimental data and this PIC analysis, and are the vertically and horizontally polarized emissions, respectively. In the vertical polarization case, Figure 5.22, the peak frequency of the analysis result is 1.3 GHz. It is similar to the peak frequency of the measurement. The peak of the analysis result is bigger than that of the measurement, and the difference is approximately 50 dB μ V/m. The analysis result shows that the radiation increases until the peak frequency and falls down quickly as the frequency increases. The difference still holds about 50 dB μ V/m. However, the low frequency region under 1 GHz has about 120 dB

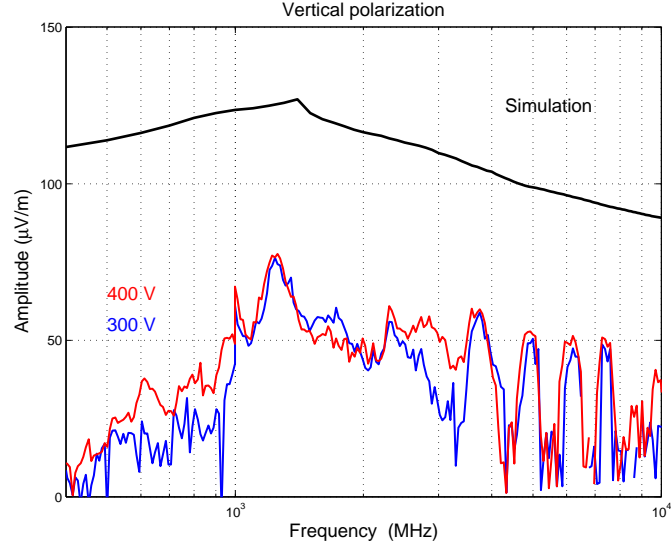


Figure 5.22: Comparison of the PIC analysis result with the BPT-4000 class Hall thruster to the measured data (vertical polarization).

$\mu\text{V}/\text{m}$ difference. It may be due to the expanded low magnetic field region in the magnetic field modeling.

Total radiation from all of the 40 cells were considered in Figures 5.22 and 5.23. Let us consider the radiation from parts of the Hall thruster, not all of it. We divide the Hall thruster into four, and Figures 5.24 and 5.25 show the results. There is no big difference between both polarizations.

The radiation from the inside of the Hall thruster is shown in Figures 5.24 a) and 5.25 a). b)s show similar trend to the horizontal case of the experiment. Plots of c) in the figures show similar pattern to the vertical polarization case of the experiment. The radiation from the exit plane, d) in both figures, shows a smooth peak around 1 GHz, which is slightly lower

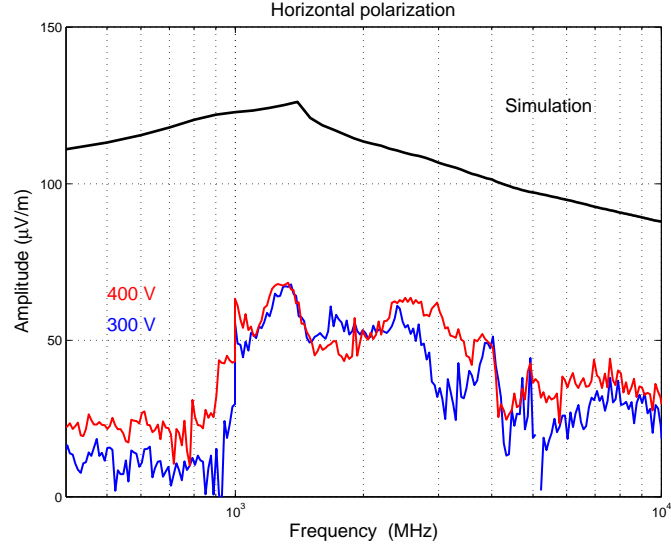


Figure 5.23: Comparison of the PIC analysis result with the BPT-4000 class Hall thruster to the measured data (horizontal polarization).

than the peak of the experiment. The maximum magnetic field at the center line is slightly behind the exit plane, and the maximum axial magnetic field shows at the middle of both side walls. At the middle of the side walls even magnetic field is maximum, other parameters, the electron temperature and density, have small values. The electron temperature and electron density distributions affect to the amplitude of the radiation, and the magnetic field determines the frequency of the radiation.

We divide the Hall thruster into eight, and Figures 5.26 and 5.27 show the results. It is hard to find difference between both polarizations. This result apparently shows that the radiation from the ionization and acceleration regions has very similar trend to the measurement data. The radiation from

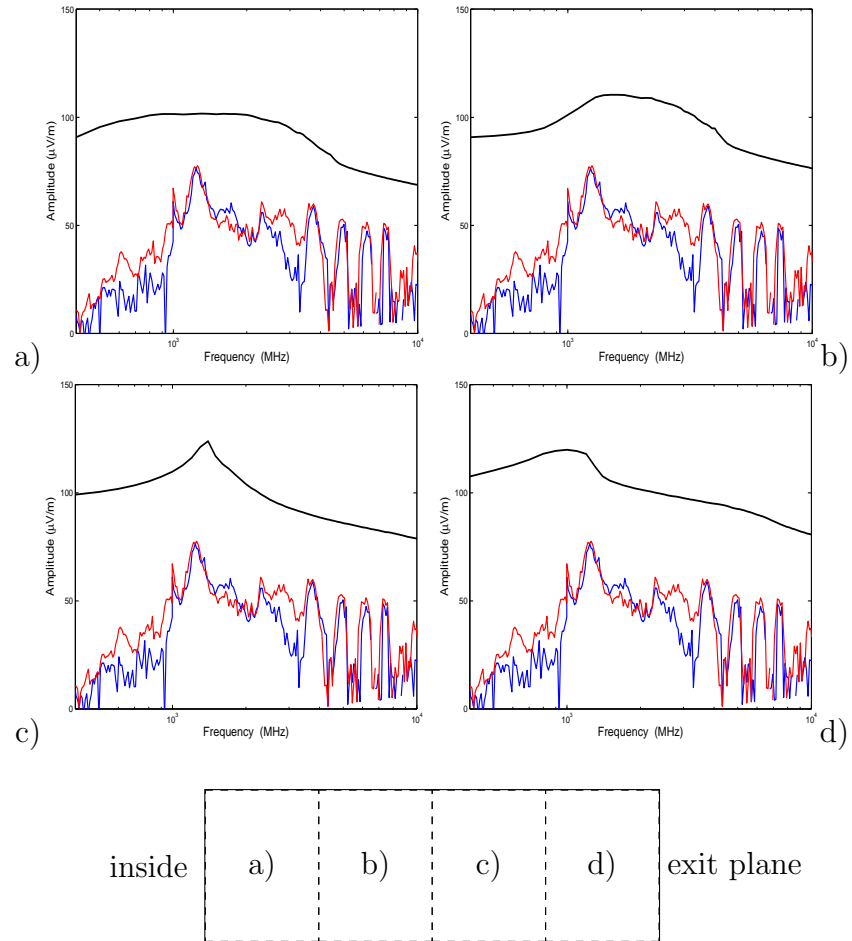


Figure 5.24: Radiation from each fourth of the Hall thruster (vertical polarization of the BPT-4000 class Hall thruster).

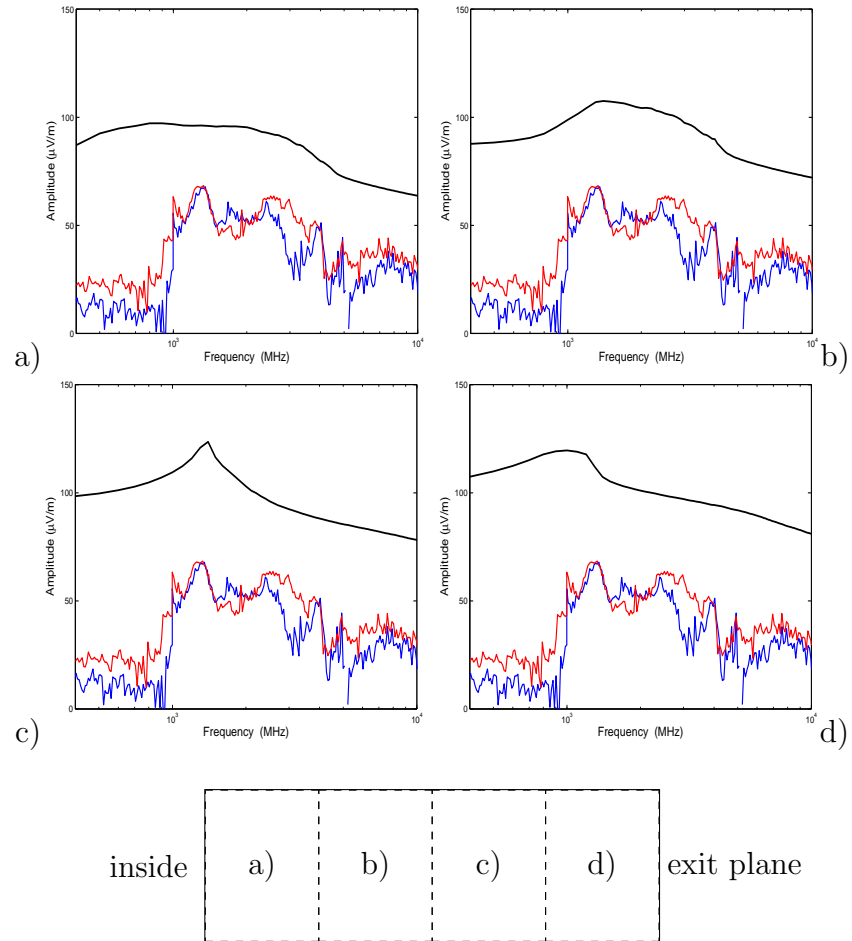


Figure 5.25: Radiation from each fourth of the Hall thruster (horizontal polarization of the BPT-4000 class Hall thruster).

the inside has a peak of low frequency of 500 MHz or a very flat top from 700 MHz to 3 GHz.

The frequency of the second peak of the experimental data is similar to the second harmonic frequency of the main peak. However, this result shows another possibility that it has different source of the radiation. Higher magnetic field at the side walls might be the source, and intermediate magnitude between the maximum radial and the maximum total magnetic fields can affect to the second peak of the experimental data.

The results of the PIC analysis show very high radiation. In the PIC analysis, we consider only plasma region. Real Hall thrusters have outer magnetic circuits, and the outer magnetic circuit of the Hall thruster might play a role of shielding. To figure out this phenomena, more detail analysis is required with real geometry data to obtain similar analysis data to the real situation.

In spite of this limitation of this analysis, with these results, we can predict the ECE radiation with plasma parameters and can also estimate where the radiation comes in the Hall thruster channel region.

5.2.2 SPT100 Class

5.2.2.1 Numerical Analysis Results

The electric field as a function of frequency is shown in Figure 5.28. The radiation has polarization information with peaks. It shows that the vertical polarization is bigger than the horizontal one. In the vertical polarization case, the peak is up to about 93 dB $\mu\text{V}/\text{m}$. The horizontal one is up to about 67 dB

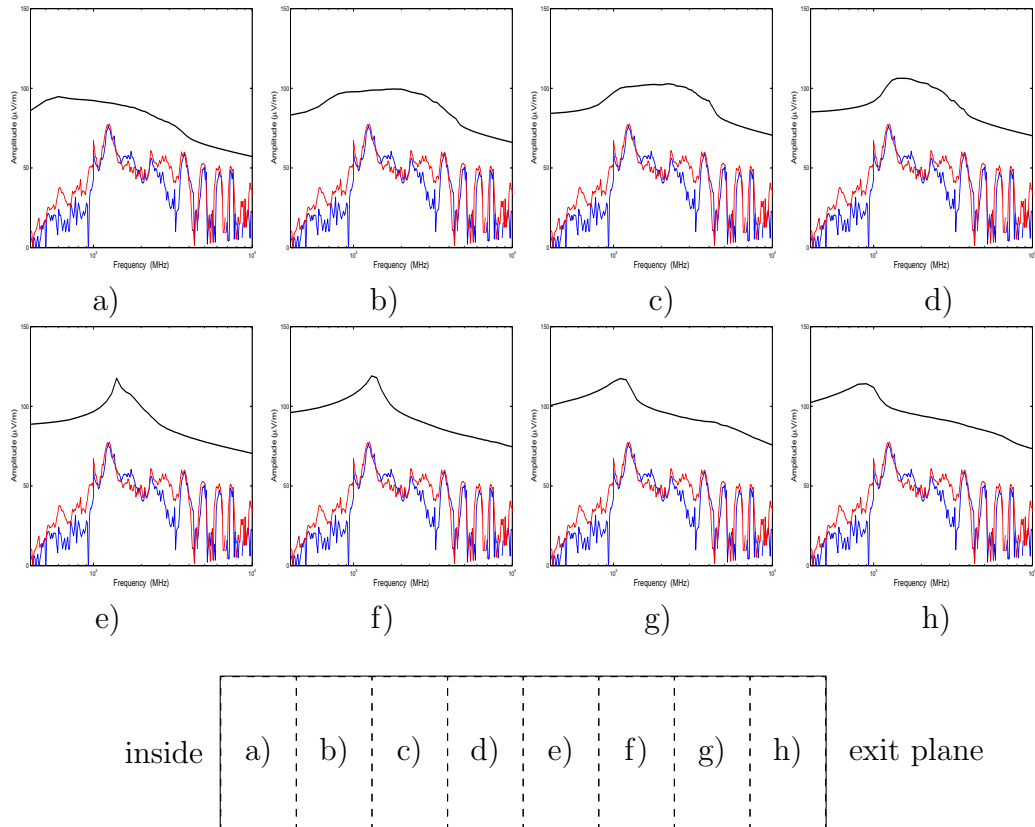


Figure 5.26: Radiation from each 1/8 of the Hall thruster (vertical polarization of the BPT-4000 class Hall thruster).

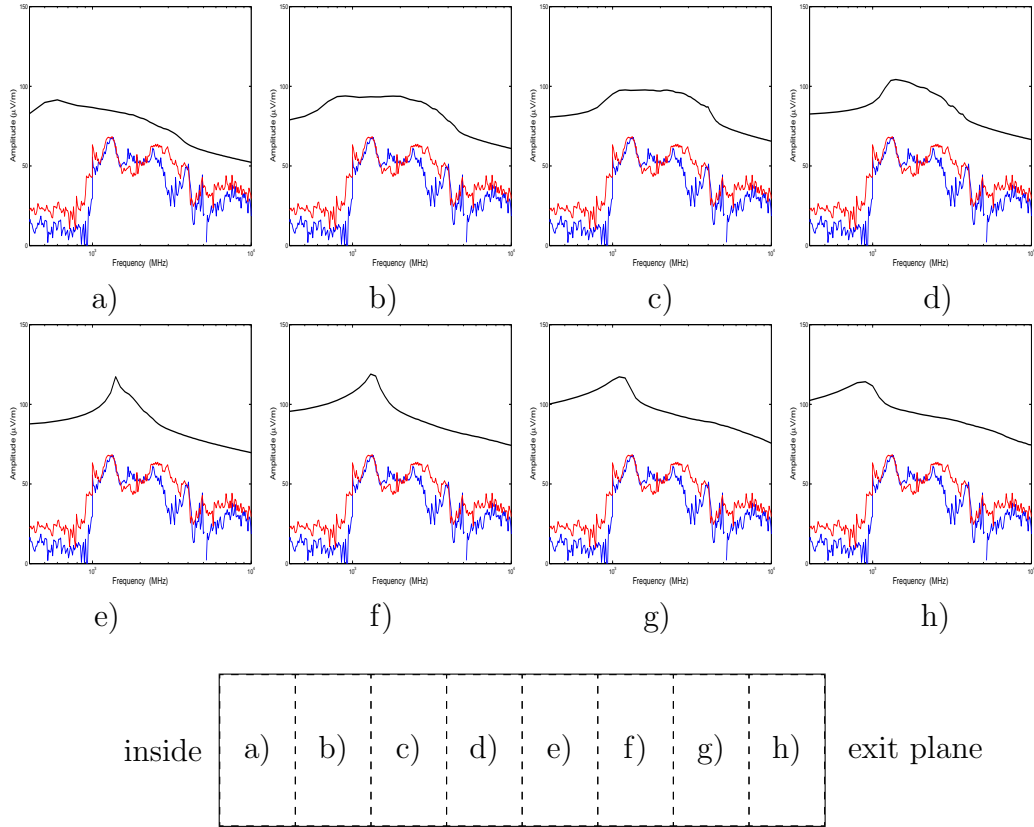


Figure 5.27: Radiation from each 1/8 of the Hall thruster (horizontal polarization of the BPT-4000 class Hall thruster).

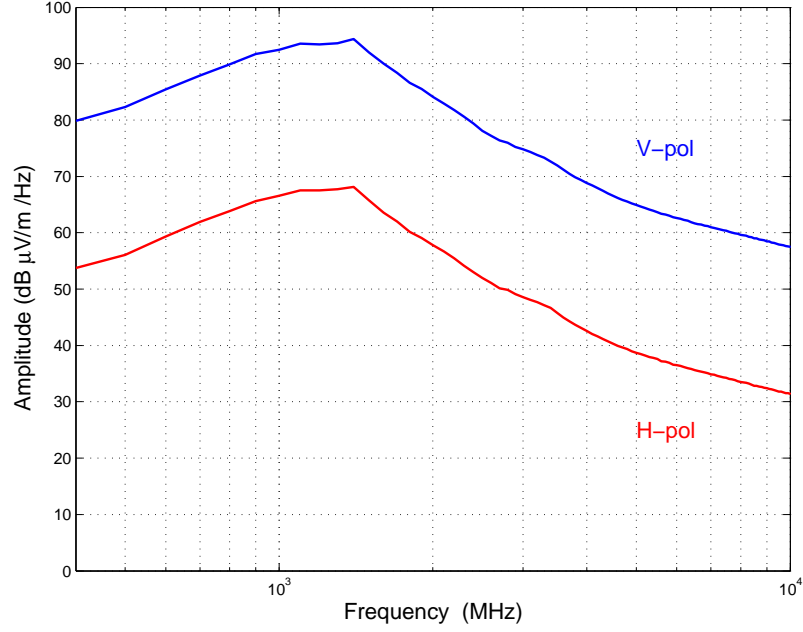


Figure 5.28: Electric field as a function of frequency at the observation point (experimental data of the SPT100 class Hallthrusters from literature).

$\mu\text{V/m}$, which is close to the result in Figure 5.7. The frequency of the peaks is around 1.3 GHz. The curves in Figure 5.28 are smoother than the curves in Figure 5.7, especially in low frequency region. It might be due to the magnetic field distribution.

5.2.2.2 Comparison to Experiment

The experimental measurement data of the emission [16, 43] were already shown in Figures 5.16, 5.8 and 5.9 and were described in the sections.

Figure 5.29 shows the comparison between the SPT100 experimental data and this PIC analysis.⁵⁵ No polarization information is shown in the

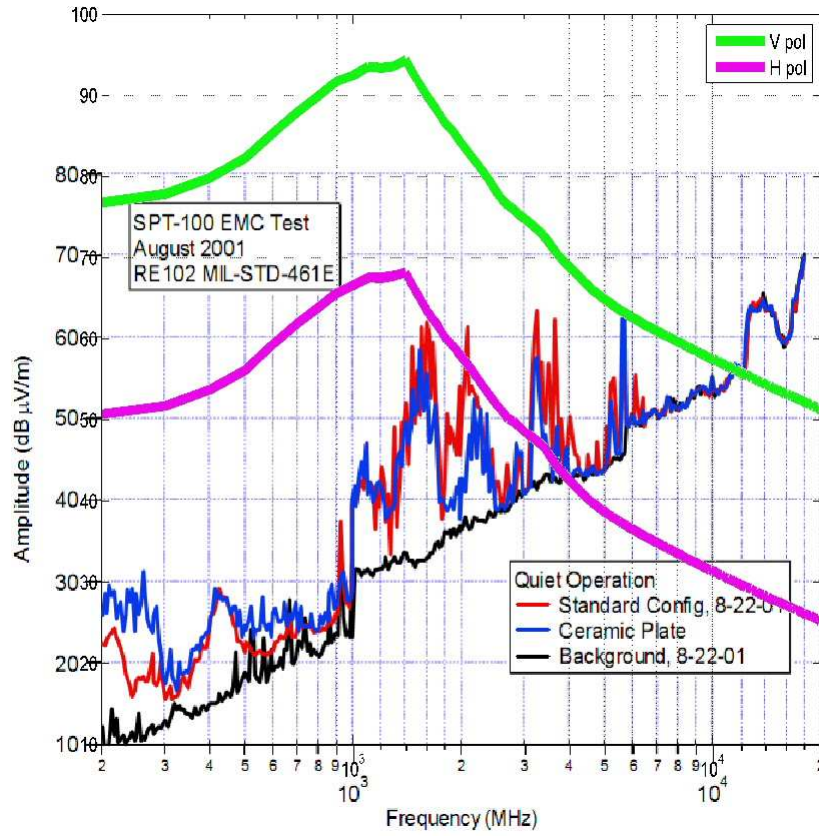


Figure 5.29: Comparison of the PIC result to the SPT100 measurement data.

measurement. In Figure 5.29, the peak frequency of the analysis result is 1.4 GHz. It is similar to the peak frequency of the measurement. The peak of the analysis result is bigger than that of the measurement. The difference from the horizontal polarization is approximately 5 dB $\mu\text{V/m}$, and that from the vertical one is about 30 dB $\mu\text{V/m}$. The analysis result shows that the radiation increases until the peak frequency, and the increase is not linear. Then, the radiation falls down quickly as the frequency increases.

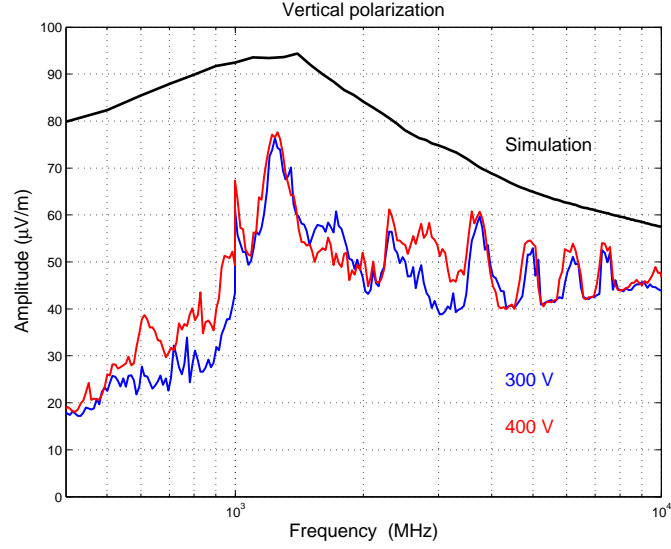


Figure 5.30: Comparison of the PIC result of SPT100 to the BPT-4000 measured data (vertical polarization).

We also compare the numerical results to the BPT-4000 measurements. The experimental data with the background subtracted shown in Figures 5.12 and 5.13 is used in this comparison. Figures 5.30 and 5.31 show the comparison between the experimental data and this PIC analysis, and are the vertically and horizontally polarized emissions, respectively.

In the vertical polarization case, Figure 5.30, the peak frequency of the analysis result is 1.3 GHz. It is similar to the peak frequency of the measurement. The peak of the analysis result is bigger than that of the measurement, and the difference is approximately 15 dB $\mu\text{V}/\text{m}$. The analysis result shows that the radiation increases until the peak frequency and falls down quickly as the frequency increases. The difference still holds about 20 dB $\mu\text{V}/\text{m}$. How-

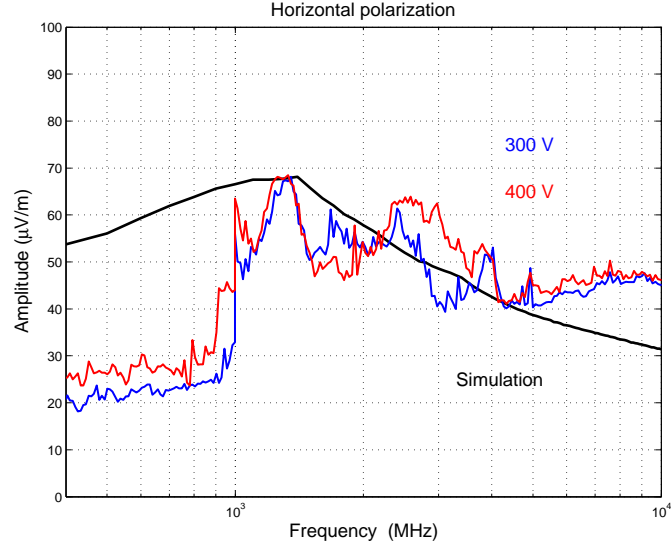


Figure 5.31: Comparison of the PIC result of SPT100 to the BPT-4000 measured data (horizontal polarization).

ever, the low frequency region under 1 GHz has about 60 dB $\mu\text{V}/\text{m}$ difference. It may be due to the expanded low magnetic field region in the magnetic field modeling.

In the horizontal polarization case, Figure 5.31, the peak frequency of the analysis result is also 1.3 GHz, and this is similar to the measurement. The peak value of the analysis result is similar to the measurement. Not only the trend but also the values of the analysis result are very similar to the measurement data except the second peak region between 2 and 3 GHz and the low frequency region under 1 GHz. The difference of the radiation is approximately 30 dB $\mu\text{V}/\text{m}$ in the low frequency region. It may also be on account of the expanded low magnetic field region.

We divide the Hall thruster into four, and Figures 5.32 and 5.33 show the radiation from each part of the Hall thruster of the vertical polarization and horizontal polarization cases, respectively.

In the vertical polarization case, Figure 5.32, d) has the closest trend to the experiment. The radiation shown in the d) is sharply increasing from 1GHz to the peak frequency and is smoothly decreasing. The peak amplitude in the simulation result is 30 dB $\mu\text{V}/\text{m}$ greater than the experimental one. We can see this trend on both polarizations.

In Figure 5.33, as the vertical polarization case, d) has the closest trend to the experiment. Not only the radiation trend but also the amplitude of the radiation are in very good agreement with the experiment. The radiation pattern in Figure 5.33 d) covers the main peak at 1.6 GHz and the second peak at 2.1 GHz.

This tells us that the exit plane region of the Hall thruster is more important for the ECE analysis than the other regions.

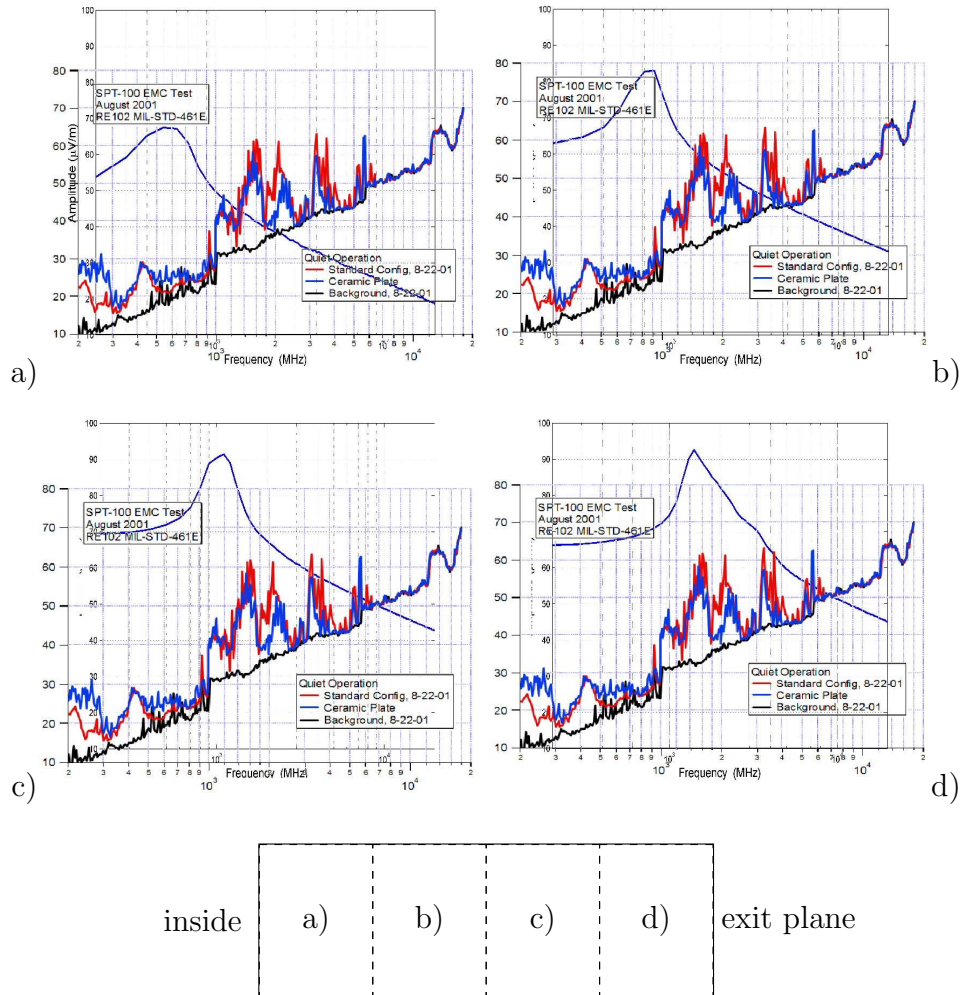


Figure 5.32: Radiation from each fourth of the Hall thruster (vertical polarization of the SPT100 class Hall thruster).

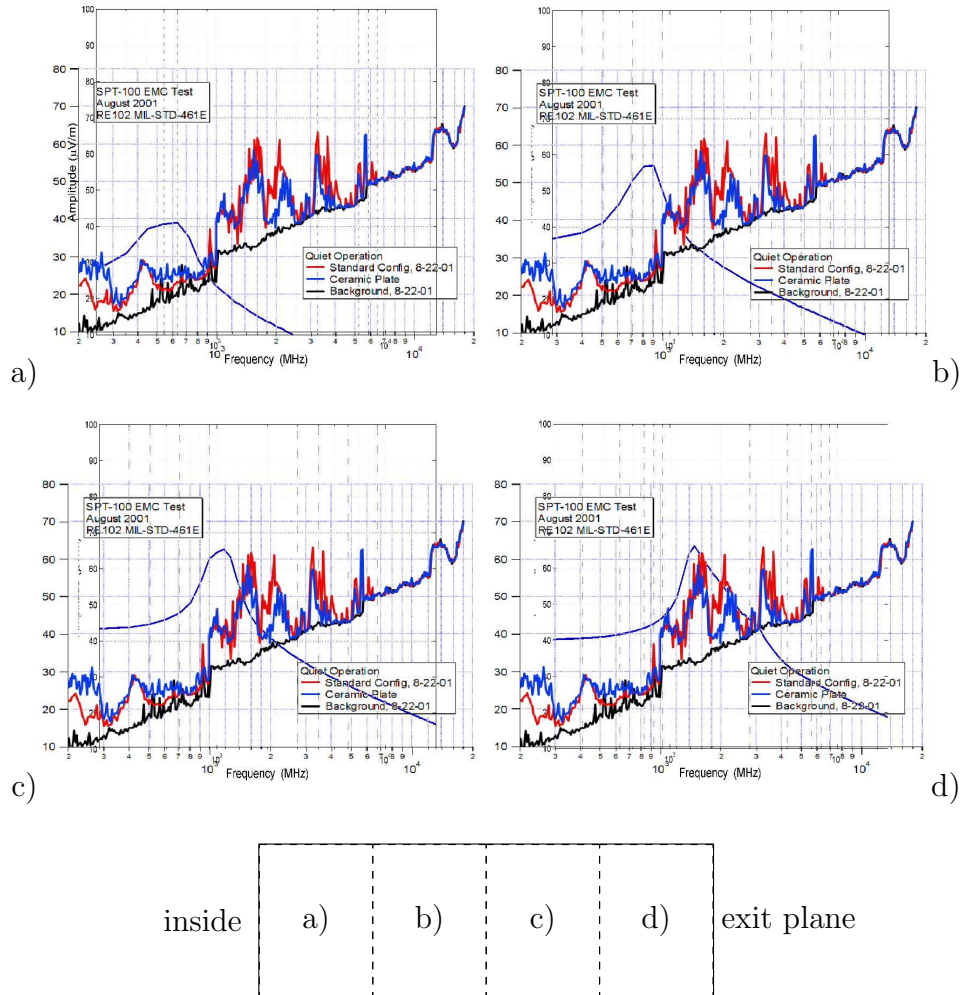


Figure 5.33: Radiation from each fourth of the Hall thruster (horizontal polarization of the SPT100 class Hall thruster).

5.3 Hybrid Element Method Results

In this analysis, we use a different configuration in the coordinate systems. The axial direction of the Hall thruster is laid on the x axis, the direction from the Hall thruster to the observation point, OB, is the y direction. The ϕ direction is from the x axis to the y axis, and the θ direction is from the z axis to the x axis. Therefore, $\phi = 0$ and $\theta = 90^\circ$ means the exit plane direction. The trajectory along θ of $\phi = 90^\circ$ is going around the side of the Hall thruster. Because EMAP5 supports only the Cartesian coordinates, we model Hall thrusters with rectangular parallelepipeds.

The analysis region is basically divided into 4 along x, by 8 along y and z. If the cell has current sources, then the cell is also divided into 4 along the source directions and into 2 along the other directions. Figure 5.34 shows the configuration for this hybrid element analysis. In Figure 5.34 a), arrows mean magnetic fields, and ovals are electron cyclotron motions.

Every cell in the plasma region has its own electron cyclotron loop and frequency governed by the magnetic field. One electron cyclotron loop can be modeled by using two dipoles 90° out of phase as mentioned in Chapter 4.2.

The lengths of dipoles are two times of the lamor radii from the magnetic fields. The currents on the dipoles are from the density and velocity of electrons, $e \cdot n_e v_e$. The dipole length multiplied by the current, $\ell \times I$, is constant in the far field cases of infinitesimal and short dipoles. Therefore, the dipole lengths are, in this analysis, fixed as 1 mm to improve the compu-

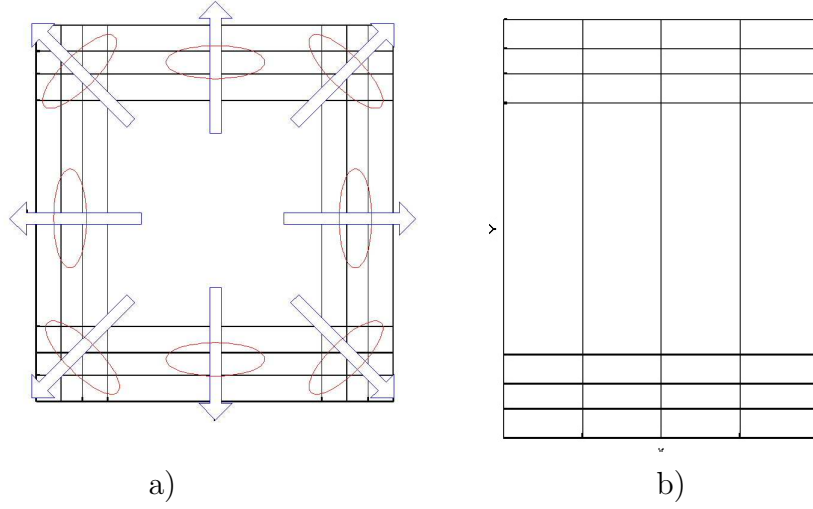


Figure 5.34: Configuration for the hybrid element analysis. a) front view b) side view

tational efficiency. Then, the current is compromised according to the ratio between the actual length and 1 mm. The $\ell \times I$ values of the fixed length dipoles are equal to the actual ones. We already checked the validity of this concept in Chapter 4.2.

Plasmas are considered as inhomogeneous dielectrics from a microwave point of view. In this analysis, plasma dielectric constants are calculated with the radiation and plasma frequencies.

The FEM part of the hybrid element method code used in this study is the 3D FEM code. The electron cyclotron motion is tilted due to the axial component of the magnetic field. We model the tilted cyclotron motion by means of considering both the radial and axial magnetic fields. The currents in the cells at the inner and outer wall sides have the radial component.

Table 5.1: Plasma parameter distributions for the hybrid element method analysis.

		$T_e(eV)$	$N_e(\times 10^{17}m^{-3})$
↑ radial 		$B_r(G)$	$B_a(G)$
		$\begin{bmatrix} 1 & 1 & 5.5 & 9 \\ 1 & 2 & 7.5 & 11 \\ 1 & 1 & 5.5 & 9 \end{bmatrix}$	$\begin{bmatrix} 3 & 6 & 8 & 10 \\ 5 & 10 & 14 & 16 \\ 3 & 6 & 8 & 10 \end{bmatrix}$
		$\begin{bmatrix} 50 & 300 & 450 & 500 \\ 50 & 300 & 450 & 500 \\ 50 & 300 & 450 & 500 \end{bmatrix}$	$\begin{bmatrix} 0 & 300 & 1200 & 0 \\ 0 & 0 & 0 & 0 \\ 0 & 300 & 1200 & 0 \end{bmatrix}$
		axial →	axial →

5.3.1 BPT-4000 Class

The BPT4000 class Hall thruster is modeled in three dimensional Cartesian coordinates. The same dimensions are used for this analysis. The length, width, and height of the Hall thruster model are 40, 140, and 140 mm, respectively.

Table 5.1 shows the distributions of the plasma parameters used in this hybrid element method analysis. These distributions are simplified versions of the previously used plasma model. Left is inner side of the Hall thruster, and right is the exit plane. Both of radial and axial magnetic field are considered in this analysis.

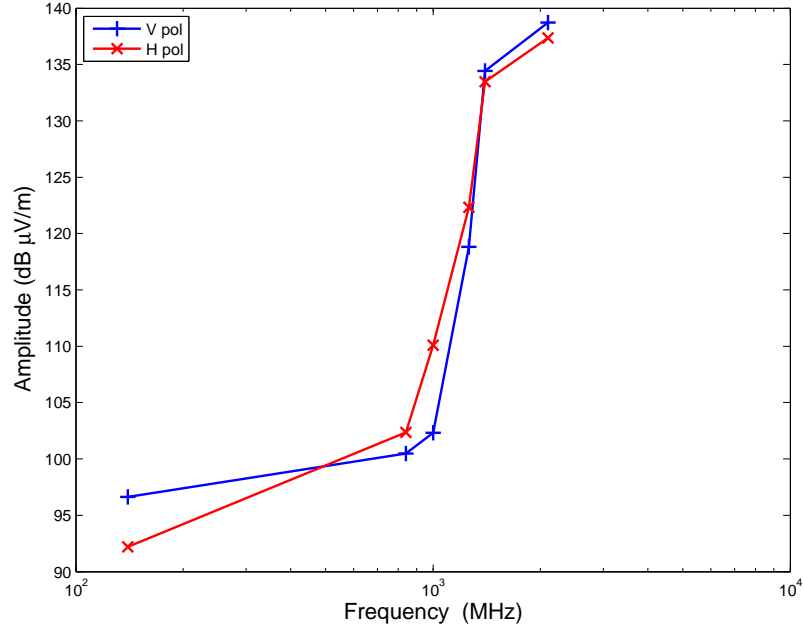


Figure 5.35: Electric field as a function of frequency of the hybrid element method analysis with the 2D magnetic field.

5.3.1.1 Numerical Analysis Results

Figure 5.35 shows the radiated electric field considering the plasma dielectric constant. We include both B_r and B_a in the analysis. The result is shown in the frequency domain. The frequencies appearing in the result are 140 MHz, 840 MHz, 1 GHz, 1.26 GHz, 1.4 GHz and 2.1 GHz. Both of the polarizations show similar results.

It shows very similar trend of radiation to the results of previous analysis. The radiation at the lower frequency than 1 GHz shows lower amplitude of about 100 dB μ V/m. The radiation is abruptly increasing from around 1

GHz and reaches a peak. The result shows a peak, the amplitude is about 140 dB $\mu\text{V}/\text{m}$, and the frequency is 2.1 GHz. The radiation at the frequency of 1.4 GHz shows over 135 dB $\mu\text{V}/\text{m}$. The radiation is about 3 dB $\mu\text{V}/\text{m}$ less than the peak. We can generally say that it shows a broad peak region from 1.4 GHz to 2.1 GHz. The peak region shows about 40 dB $\mu\text{V}/\text{m}$ higher amplitude than the low frequency region.

5.3.1.2 Comparison to Experiment

We compare the results of the hybrid element analysis to the experimental data [43]. The simulation results with the 2D magnetic field distribution is compared to the experiments in Figures 5.36 and 5.37. The results showed very similar radiation pattern in the frequency domain. The comparisons in both polarizations show the same trend. Figure 5.36 shows that the difference between the numerical analysis and the experiment is about 65 dB $\mu\text{V}/\text{m}$ at the peak, is about 55 dB $\mu\text{V}/\text{m}$ at around 1 GHz and is about 70 dB $\mu\text{V}/\text{m}$ at 400 MHz. Both polarization of the experiment show faster increasing of the radiation from around 1 GHz. The analysis results show the same trend to the experiment.

In the comparison of the horizontal polarization cases, the amplitude of the second peak is comparable to the main peak. In the results, we can see the radiation at the frequency of 2.1 GHz. This is from the high magnitude of the magnetic field due to the axial field. The radiation at 2.1 GHz is about 5 dB $\mu\text{V}/\text{m}$ higher than that of 1.4 GHz. This can be another clue of the source

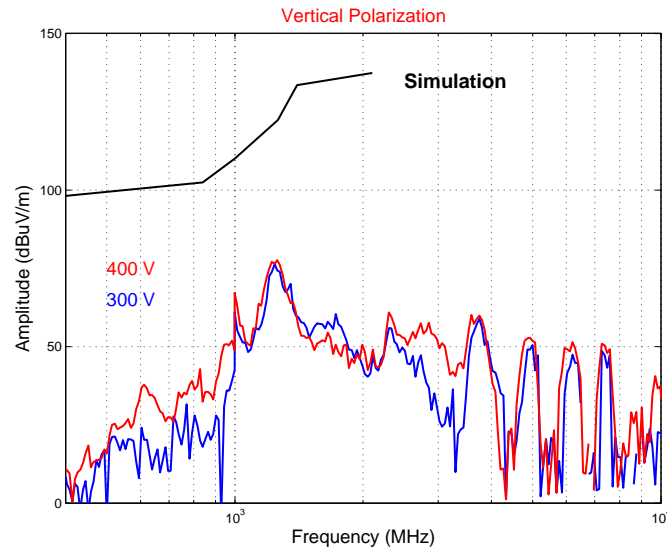


Figure 5.36: Comparison of the 2D hybrid element analysis result using the 2D magnetic field distribution to the experimental data (vertical polarization).

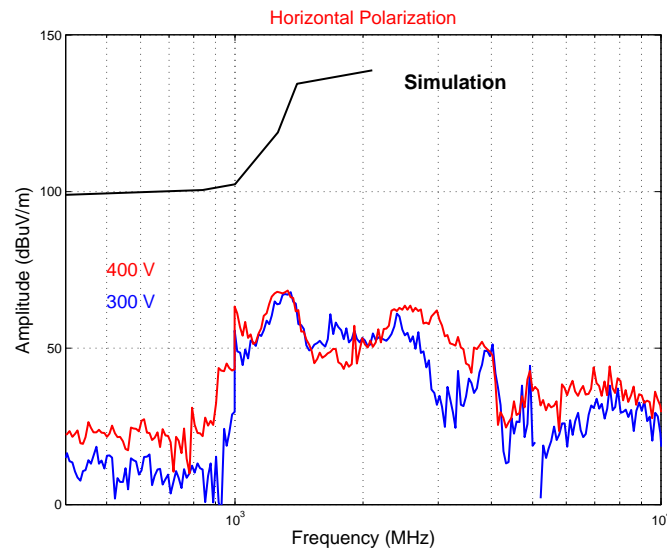


Figure 5.37: Comparison of the 2D hybrid element analysis result using the 2D magnetic field distribution to the experimental data (horizontal polarization).

Table 5.2: Plasma parameter distributions for the hybrid element method analysis.

		$T_e(eV)$	$N_e(\times 10^{17}m^{-3})$
↑ radial 		$\begin{bmatrix} 5 & 11 & 12 & 11 \\ 6 & 19 & 10 & 11 \\ 5 & 12 & 7 & 8 \end{bmatrix}$	$\begin{bmatrix} 1.1 & 2 & 2.1 & 1 \\ 1.6 & 3.6 & 5 & 2.7 \\ 1.1 & 2.2 & 3.1 & 1.4 \end{bmatrix}$
		$B_r(G)$	$B_a(G)$
↑ radial 		$\begin{bmatrix} 170 & 300 & 420 & 620 \\ 190 & 350 & 460 & 540 \\ 200 & 370 & 520 & 850 \end{bmatrix}$	$\begin{bmatrix} 170 & 180 & 200 & 120 \\ 60 & 0 & 0 & 60 \\ 0 & -100 & -100 & 0 \end{bmatrix}$
		———— axial ———→	———— axial ———→

of the second peak. The frequency of the second peak is about twice of the main peak in the experiment. However, the trend of the second peak is slightly different the main peak. The main peak is sharp, but the second peak has a broad one. As mentioned before, the amplitude of the second peak is similar to the main peak in the horizontal polarization case. The higher magnitude of the magnetic field can be another clue to explain this second peak.

5.3.2 SPT100 Class

The SPT100 class Hall thruster is modeled in three dimensional Cartesian coordinates. The same dimensions are used for this analysis. The length, width, and height of the Hall thruster model are 40, 100, and 100 mm, respec-

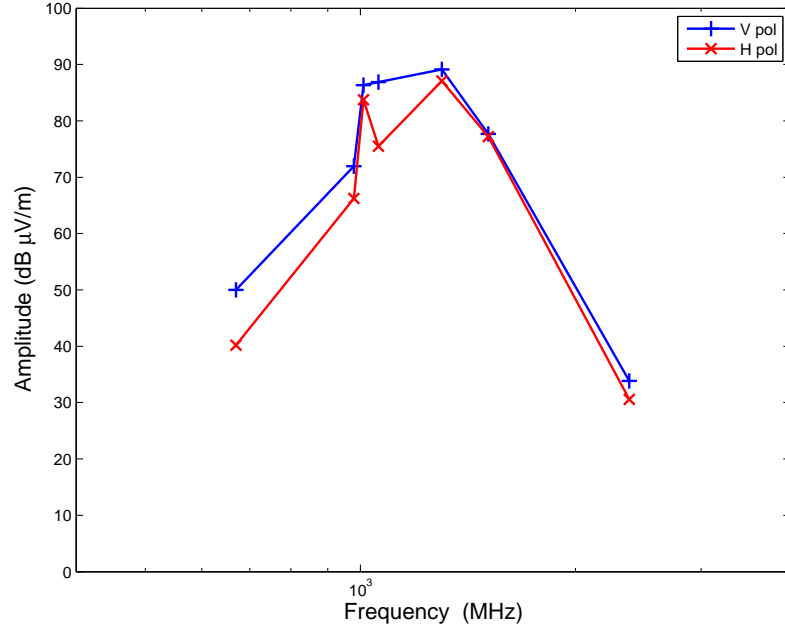


Figure 5.38: Electric field as a function of frequency of the hybrid element method analysis with the 2D magnetic field.

tively.

Table 5.2 shows the distributions of the plasma parameters used for the hybrid element method analysis of the SPT100 Hall thruster. These distributions are simplified versions of the previously used plasma model. Radial and axial magnetic field are used for this analysis.

5.3.2.1 Numerical Analysis Results

Figure 5.38 shows the radiated electric field considering the plasma dielectric constant. Both B_r and B_a were considered in the analysis. The frequencies appearing in the result are 670 MHz, 980 MHz, 1.01 GHz, 1.06

GHz, 1.3 GHz, 1.51 GHz and 2.38 GHz. The vertical polarization case is approximately 10 dB $\mu\text{V}/\text{m}$ greater than the horizontal one in below 1 GHz range. Two peaks are shown in the horizontal case between 1 GHz and 1.3 GHz. The vertical case shows one broad peak in the same range. Amplitudes of peaks in both cases are upto 90 dB $\mu\text{V}/\text{m}$. After 1.3 GHz, both polarization cases show very similar decreasing radiation pattern.

5.3.2.2 Comparison to Experiment

We compare the results of the hybrid element analysis to the experimental data [16]. Figure 5.39 shows comparison of the SPT100 simulation results with the 2D magnetic field distribution to the experiments. The results showed very similar radiation pattern in the frequency domain. The amplitudes of the peaks are about 30 dB $\mu\text{V}/\text{m}$ higher than the measurement. The horizontal polarization case caught the trend not only at the main peak of 1.3 GHz but also at a smaller peak of 1 GHz

We also compare the SPT100 results to the BPT-4000 experimental data [43]. Figures 5.40 and 5.41 show the comparison. The results show very good agreement with the measurement. The numerical results caught most of the radiation trends: sharp increasing from 900 MHz, a peak at 1 GHz and sharp decreasing. It shows about 20 dB $\mu\text{V}/\text{m}$ difference in the range between 1 GHz and 2 GHz.

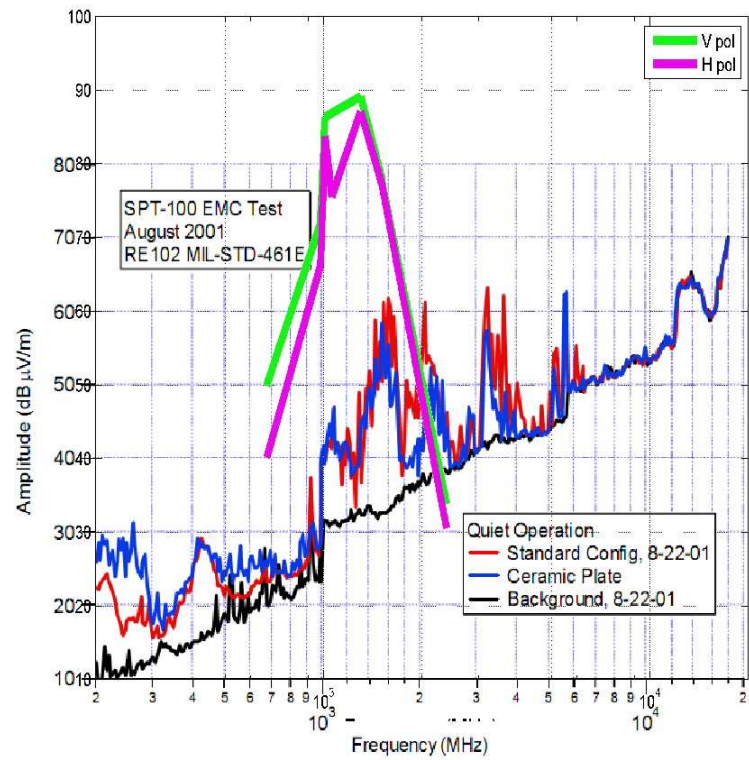


Figure 5.39: Comparison of the SPT100 hybrid element analysis result using the 2D magnetic field distribution to the experimental data.

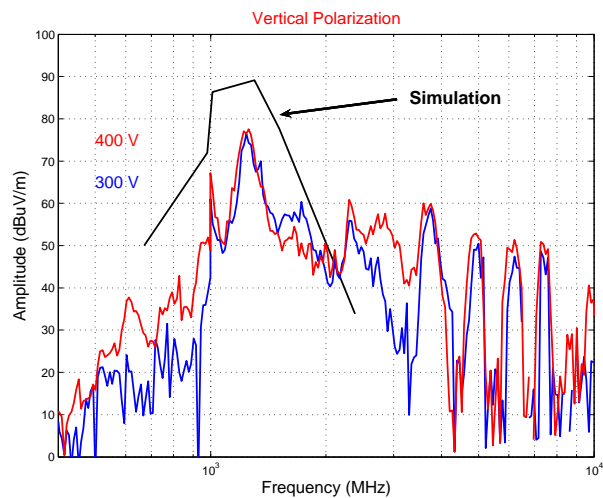


Figure 5.40: Comparison of the SPT100 hybrid element analysis result using the 2D magnetic field distribution to the BPT-4000 measured data (vertical polarization).

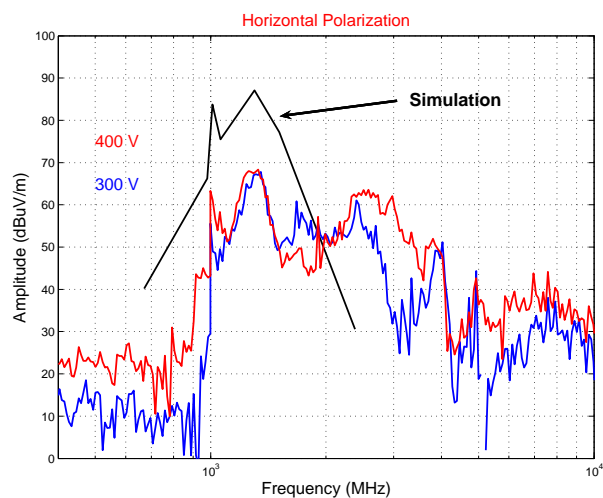


Figure 5.41: Comparison of the SPT100 hybrid element analysis result using the 2D magnetic field distribution to the BPT-4000 measured data (horizontal polarization).

Chapter 6

Discussion

6.1 Comparison of Results

We showed the results of the three analysis methods for the ECE radiation analysis of the Hall thruster. The three methods are the single particle approximation analysis, the particle-in-cell (PIC) analysis and the hybrid element analysis. In this section, we compare the three approaches to the experiments and to each other. The analysis results with the 2D magnetic field distribution are more realistic in all the approaches, so only the 2D results are compared in this section.

6.1.1 BPT-4000 Class

Figures 6.1 and 6.2 show the comparison of the approaches and the experiments in the vertical and horizontal polarizations, respectively. The target Hall thruster is a BPT-4000 class one. The single particle approximation analysis has no polarization data. The presented data of the single particle approximation analysis is all polarizations.

First, all of the numerical results show small differences between the vertical and horizontal polarizations. However, the experimental data appar-

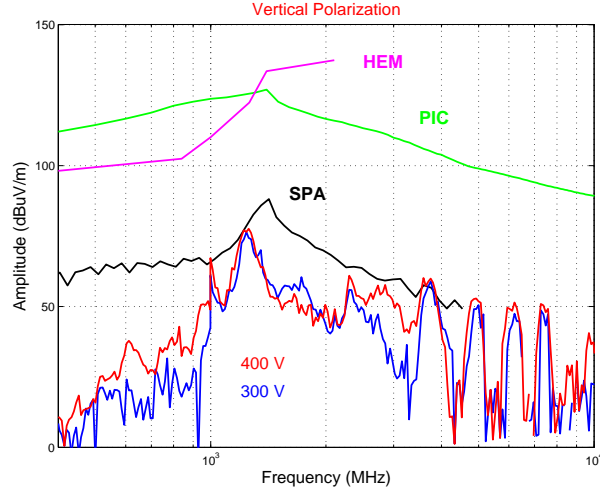


Figure 6.1: Comparison of the BPT-4000 experimental data to all three approaches: the single particle approximation analysis (SPA), the particle-in-cell analysis (PIC) and the hybrid element analysis (HEA). (vertical polarization).

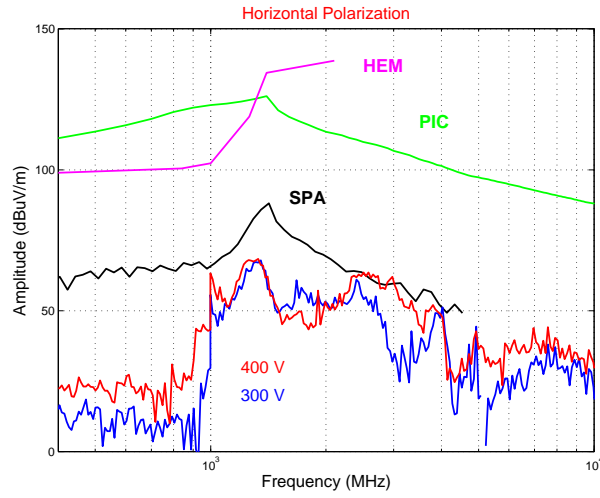


Figure 6.2: Comparison of the BPT-4000 experimental data to all three approaches: the single particle approximation analysis (SPA), the particle-in-cell analysis (PIC) and the hybrid element analysis (HEA). (horizontal polarization).

ently shows the difference in the polarizations.

All of the numerical results have the similar radiation trend to the experiments in the frequency domain. The radiation increases from the low frequency region, less than 1 GHz, to the main peak frequency. In this period, abruptly increasing points are shown in all cases in Figures 6.1 and 6.2 except the results of PIC analysis. The abruptly increasing point frequencies of the experiments, the single particle approximation analysis, and the hybrid element analysis are about 900 MHz, 1GHz, and 840 MHz, respectively. All the numerical methods and the experiments show the main peak frequencies around 1.3~1.4 GHz and similar radiation trends to each other.

The single particle approximation analysis shows 10 dB $\mu\text{V}/\text{m}$ higher amplitude at the peak than the experiments in the vertical polarization and 15 dB $\mu\text{V}/\text{m}$ higher amplitude of the peak in the horizontal one. In the higher frequency region than the main peak one, it keeps the difference of 10 dB $\mu\text{V}/\text{m}$ in the vertical polarization and that of 15 dB $\mu\text{V}/\text{m}$ in the horizontal one.

The PIC analysis shows about 100 dB $\mu\text{V}/\text{m}$ difference in the low frequency region, 50 dB $\mu\text{V}/\text{m}$ greater amplitude at the peak than the experiments in the vertical polarization, 60 dB $\mu\text{V}/\text{m}$ greater amplitude of the peak in the horizontal one and approximately 65 dB $\mu\text{V}/\text{m}$ greater amplitude in the high frequency region.

The hybrid element analysis shows about 70 dB $\mu\text{V}/\text{m}$ difference in

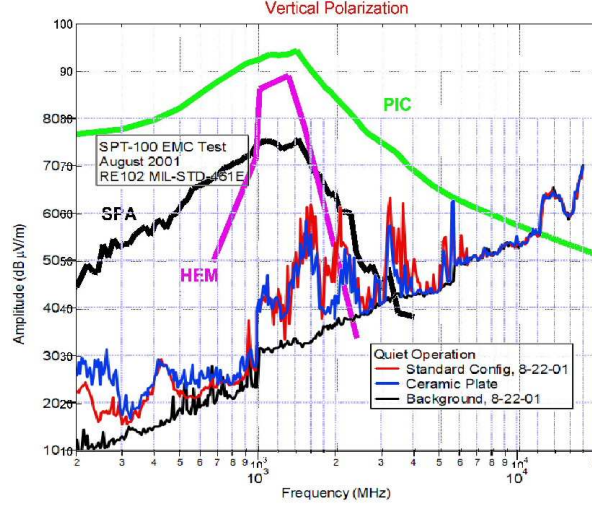


Figure 6.3: Comparison of the SPT100 experimental data to all three approaches: the single particle approximation analysis (SPA), the particle-in-cell analysis (PIC) and the hybrid element analysis (HEA). (vertical polarization).

the low frequency region, 55 dB $\mu\text{V}/\text{m}$ greater amplitude at the peak than the experiments in the vertical polarization and 70 dB $\mu\text{V}/\text{m}$ greater amplitude of the peak in the horizontal one. The hybrid element analysis does not show the results in the high frequency region. It showed only six frequencies, and the maximum frequency is 2.1 GHz.

6.1.2 SPT100 Class

Figures 6.3 and 6.4 show the comparison of the approaches and the experiments with the SPT100 class Hall thruster. As we mentioned, data from the single particle approximation analysis is all polarizations.

All of the numerical results except the single particle approximation one

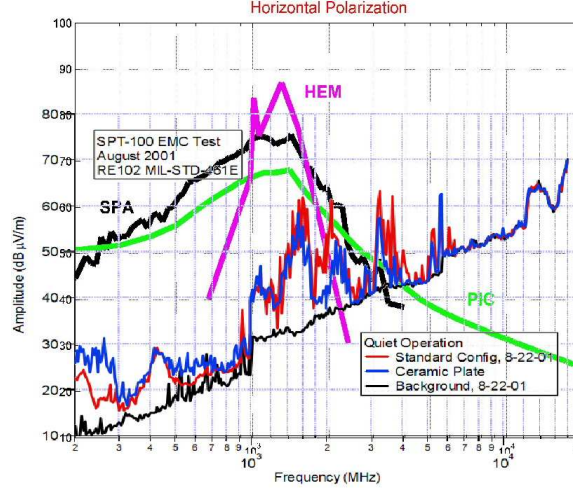


Figure 6.4: Comparison of the SPT100 experimental data to all three approaches: the single particle approximation analysis (SPA), the particle-in-cell analysis (PIC) and the hybrid element analysis (HEA). (horizontal polarization).

show the difference in the polarizations. However, the measurements show no polarization information. Results from the single particle approximation analysis and the PIC analysis show very similar radiation trend. The hybrid element analysis one has closer trend to the experiment. The peak frequencies of the approaches and experiment are between 1.3 GHz and 1.6 GHz.

The single particle approximation analysis shows 15 dB $\mu\text{V}/\text{m}$ higher amplitude at the peak than the experiment. In the higher frequency region than the main peak one, it keeps the difference of 15 dB $\mu\text{V}/\text{m}$. The PIC analysis shows about 50 dB $\mu\text{V}/\text{m}$ difference in the low frequency region, 30 dB $\mu\text{V}/\text{m}$ greater amplitude at the peak than the experiments in the vertical polarization and 7 dB $\mu\text{V}/\text{m}$ greater amplitude of the peak in the horizontal

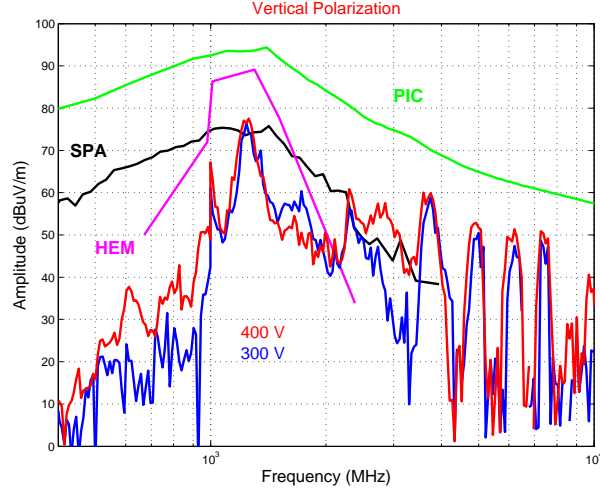


Figure 6.5: Comparison of the BPT-4000 experimental data to all three approaches: the single particle approximation analysis (SPA), the particle-in-cell analysis (PIC) and the hybrid element analysis (HEA). (vertical polarization).

one. The hybrid element analysis shows about $27 \text{ dB } \mu\text{V/m}$ greater amplitude at the peak than the experiments in the vertical polarization and $25 \text{ dB } \mu\text{V/m}$ greater amplitude of the peak in the horizontal one. After the peak, the hybrid element analysis shows rapid drops of the radiation.

We also compare the SPT100 results to the BPT-4000 experiment and show the comparison in Figures 6.5 and 6.6.

All of the numerical results except the single particle approximation one show the difference in the polarizations. This measurement also shows the polarization information. Results show very similar radiation trend each other. The hybrid element analysis one has closer trend to the experiment. The peak frequencies of the approaches and experiment are between 1.2 GHz

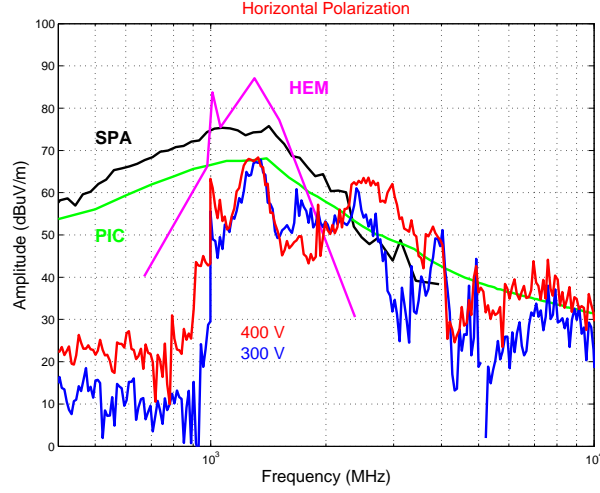


Figure 6.6: Comparison of the BPT-4000 experimental data to all three approaches: the single particle approximation analysis (SPA), the particle-in-cell analysis (PIC) and the hybrid element analysis (HEA). (horizontal polarization).

and 1.4 GHz.

The single particle approximation analysis shows the same amplitude at the peak as the experiment, and about 7 dB $\mu\text{V}/\text{m}$. In the higher frequency region than the main peak one, it keeps the difference of 15 dB $\mu\text{V}/\text{m}$. The PIC analysis shows about 50 dB $\mu\text{V}/\text{m}$ difference in the low frequency region, 30 dB $\mu\text{V}/\text{m}$ greater amplitude at the peak than the experiments in the vertical polarization and 7 dB $\mu\text{V}/\text{m}$ greater amplitude of the peak in the horizontal one. The hybrid element analysis shows about 27 dB $\mu\text{V}/\text{m}$ greater amplitude at the peak than the experiments in the vertical polarization and 25 dB $\mu\text{V}/\text{m}$ greater amplitude of the peak in the horizontal one. After the peak, the hybrid element analysis shows rapid drops of the radiation.

6.2 Differences between Numerical Results and Experiments

The single particle approximation analysis shows the closest results to the experiments, and the PIC and hybrid element analysis results show big offsets. There can be many possibilities for the differences between numerical analysis and experimental data.

The magnitude of the radiation is from the plasma parameters. These big offsets might be from our smooth and rough plasma models. Comparisons of SPT100 cases having better plasma parameter distributions showed better agreement with the experiments than BPT-4000 cases. Measurement data of the BPT4000 Hall thruster can improve this point. In the hybrid element analysis, we divided the plasma region into 4 and 3 along the axial and radial directions, respectively. Smaller mesh size can generate more broadened spectrum and less amplitude of the radiated field. However, finer mesh requires higher computation performance. Compensation of the offsets with the plasma parameter distributions might have limits.

Another thing is that we considered only the plasma region though the approaches and did not consider the structure components of the Hall thruster, i.e., inner and outer magnetic circuits. Hall thrusters have inner and outer magnetic circuits to generate the optimal magnetic field for the Hall thrusters. In most of Hall thrusters, this structure covers the outside of the acceleration region. It can cause the effects of shielding, reflection and diffraction on the radiation. If we can consider these effects, the radiation levels

of have to be much higher than the experiments. Therefore, the numerical analysis results considered no outer and inner magnetic circuits might show higher radiation levels. The shielding effect analysis considering the magnetic circuit structure requires the Hall thruster information about the structures and materials. Unfortunately, we could not access the information. The structure and material information of the Hall thruster can make the analysis of the ECE radiation more realistic.

One of the possibilities is the numerical or statistical noise in the PIC Monte Carlo method. It is known that the statistical noise of Monte Carlo methods decreases as $1/\sqrt{N}$, where N is the number of particles. When we have four times more particles for the analysis, we will get half of the statistical noise. The statistical noise leads to a systematical error in the electron cooling or heating [48, 67]. They also announced that the stability condition for the conventional PIC requires the resolution of the electron plasma frequency ω_{pe} [45]. If we increase the number of particles for this study and reduce the time step, then we may reduce the statistical noise.

6.3 Comparison of Three Numerical Approaches

Each analysis methods has its own advantages and disadvantages. Let us compare the computation time. All of the numerical analyses in this study were done on a 2 GHz Pentium M personal computer with 512 MB memory. The single particle approximation analysis took less than a minute, the PIC analysis took hours, and the hybrid element analysis took more than a week.

It is hard to say simply. If we increase the number of particles, then the PIC analysis will take more time. However, this is not only for the PIC analysis. If we increase the number of meshes, then the hybrid element analysis will need more time to solve the problem.

The single particle approximation analysis was easily implemented and showed the results quickly. The results also had reasonable spectrum ranges, up to 4.5 GHz in this study, for comparison to the experiments. It showed the closest results to the experiments. However, the radiation results were very low if we consider the shielding effect in the real system, and it did not show the polarization information of the radiation and assumed the radiation in free space.

The PIC analysis is from the definition of the radiation. We can adjust the frequency range with the sampling time and the total sampling period in the criteria of the Fourier transform and the stable electron motion in a magnetic field. It showed the polarization information of the radiation. The amplitude of the radiation in the frequency domain is much higher than the measurement data. However, it can be closer to the real system. We assumed in this analysis that the radiation is in free space.

The hybrid element analysis is the combined method of FEM and MoM. The hybrid element analysis showed the results considered the plasma as dielectrics. The radiation level is similar to the results of the PIC analysis. It showed very close shape of the radiation trend in the frequency domain. However, the frequency range is narrow, and the frequencies are sparse. It

required high computational costs to solve the problem. If we try more detail distributions to obtain finer and more detail results, it will require extremely longer time and more computational resources.

The three methods for the ECE radiation analysis of the Hall thruster are compensating their disadvantages. The single particle approximation analysis is for easy approaches, the computation time and reasonable frequency range. The PIC analysis is for the detail radiation information in the frequency domain, the computation time. The hybrid element analysis is for considering the plasma as dielectrics.

6.4 Harmonics

In the experiment data [43], we can recognize the harmonics especially in the vertical polarization case. Our numerical results, however, did not show the harmonics. Generally nonlinearity can cause harmonics. In the real world, possibilities can be on the gradient of magnetic fields mentioned in 2.1.4, non-Maxwellian tail distribution of electron energy, etc...

The gradient of magnetic fields can cause harmonics. We consider only the first gradient in (2.26), then we can see the second harmonics in (2.28). If magnetic fields have very complex distributions it can cause high order harmonics. Naturally, magnetic fields in Hall thrusters are smoothly curved. Therefore, the second harmonics can be from the gradient of magnetic field distributions in the Hall thrusters. However, clear harmonics up to 6th shown in the vertical polarization case of the experiment data [43]. It can be from

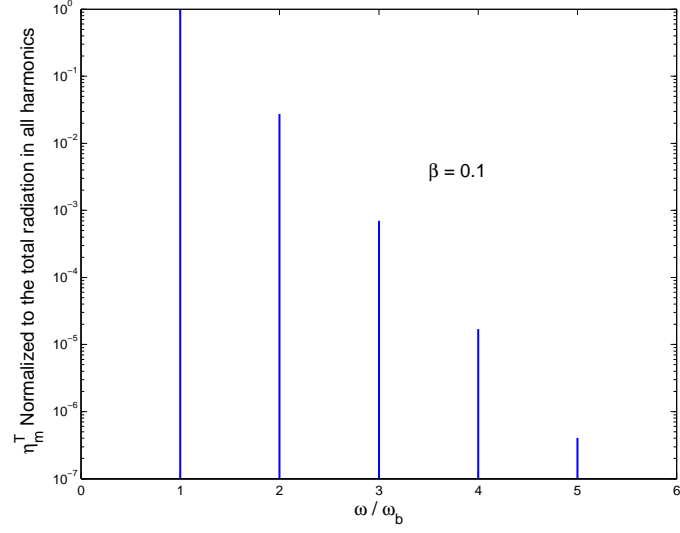


Figure 6.7: The spectrum of cyclotron radiation be a nearly nonrelativistic electron ($\beta_{\parallel}=0.1$) [6].

other reasons.

We assumed the Maxwellian distribution of electron energy. However, if it is not Maxwellian, especially at the tail distribution, then it can cause harmonics. We have mentioned the cyclotron radiation harmonics by nonrelativistic electrons in 2.2.2. Figure 6.7 shows the spectrum consists of a series of discrete lines of decreasing intensity. The lines are separated in frequency almost by the value ω_b .

From this, we can presume that there may be high energy electrons in BPT-4000, and SPT100 compared to BPT-4000 may have much less high energy electrons in the plasma channel region.

Chapter 7

Conclusion and Suggested Future Works

7.1 Conclusion

In this study, we developed three computational techniques for the ECE radiation analysis of the Hall thruster.

The first one is the single particle approximation analysis. This is the simplest one among the approaches. We modeled the plasma region of the Hall thruster with three parameters, the magnetic field, electron temperature, and electron density distributions. These parameters are constant in a cell. We calculated the radiation with the parameter distributions according to the observation angle. The frequency of a cell is determined by the magnetic field of the cell. This analysis is easy to approach and does not require a high computing performance. However, this analysis does not give detailed results. The radiated electric field is derived from the power, so there is no polarization information on the electric field. We moved onto a more sophisticated analysis.

The next approach is the Particle-In-Cell (PIC) analysis. PIC is for analysis of microscopic phenomena. Particle motions in the thruster channel region are simulated with the PIC method. We selected electrons from the Maxwell-Boltzmann distribution for the speed of electrons. The Monte Carlo

method was adopted in this selection. We solved the Lorentz force equation to get the motion data of the electrons and analyzed the radiated electric field with the particle motions. Then, we took the Fourier transform of the electric field to consider the radiation in the frequency domain. This approach is from fundamental definition, the radiation is from charge acceleration. It is a more realistic approach to the plasma. It uses the same parameter distributions, but the parameters in a cell are not constant any more because of adopting the Monte Carlo method. It also shows the polarization information of the radiation. However, we assume in this analysis that the radiation is in free space. The channel plasma is considered as current sources for radiation. The material constants of the plasma are considered as free space.

The last approach adopted is to consider the non free space and inhomogeneous media. The hybrid FEM/MoM (hybrid element method) [34, 39, 47, 88] was suggested to exploit advantages of finite element method (FEM) and method of moment (MoM) and to compensate their disadvantages. EMAP5 [25] was used to analyze the ECE radiation. We considered the plasma dielectric constants instead of free space. Simplified plasma parameter distributions were used because of the number of meshes used in the FEM analysis region. If we use finer meshes then we can get wider frequency ranges up to certain level. The amplitude of the radiation may also be spread to the newly occurred neighbor frequencies. The hybrid element analysis is an approach to analyze the ECE radiation of the Hall thruster with considering the plasma dielectric constants.

The results from this study include the following:

- Plasma parameter models were developed with data from literature.
- The single particle approximation analysis was developed, and the results of the analysis showed good agreement with the experimental data.
- It was verified that the radiation was ECE from the Hall thruster
- The PIC simulation for the ECE radiation of the Hall thruster was developed.
- The result showed the polarization information and radiation information from particular annular cell.
- We could predict the origin and characteristics of the ECE radiation and relationship between the ECE radiation and plasma parameters.
- The hybrid element analysis was developed to consider the plasma as inhomogeneous dielectric media.
- The result showed the pattern distortion in dielectrics with respect to the frequency and the difference on the radiation pattern between considering free space and dielectrics.
- The results of all computational techniques were compared to the experimental data, and the radiation trends were in good agreement.

7.2 Future Work

Suggested future work are discussed in this section.

- This work can be extended to predict the effect of the plume on the various subsystems and mitigate risk associated with the introduction of the Hall thruster.
- The radiation levels were much higher than the experimental data in both of the PIC and hybrid element analysis. This may be caused from the shielding effects of the inner and outer magnetic circuit structures. The structural and material information of the Hall thruster is required to analyze the shield effect. The closer results to the real world may be obtained.
- Small mesh size for the hybrid element analysis can be another challenge. More detail results with the plasma dielectric constants considered can be obtained. It requires very powerful computation performances.
- Using optimization algorithms, inverse problems to find plasma parameters with the measured radiation data can be tried.
- In the hybrid element analysis, the plasma is considered as isotropic. Magnetized plasmas are anisotropic. Considering anisotropy of the plasma may obtain more realistic results. New version of FEM part of the hybrid element analysis is required.

Appendices

Appendix A

Fourier Transform

A.1 Continuous-Time time Fourier Series

Any periodic waveform, $f(t)$, can be represented as the sum of an infinite number of sinusoidal and cosinusoidal terms with a constant term [84]. This representation is the Fourier series given by

$$f(t) = a_0 + \sum_{n=1}^{\infty} a_n \cos(n\omega t) + \sum_{n=1}^{\infty} b_n \sin(n\omega t) \quad (\text{A.1})$$

where t is time, $f(t)$ is the waveform, $\omega = 2\pi/T_p$ is the fundamental angular frequency, T_p is the repetition period of the waveform, a_0 is a constant equal to the time average of $f(t)$ taken over one period, which is given by

$$a_0 = \frac{1}{T_p} \int_{-T_p/2}^{T_p/2} f(t) dt \quad (\text{A.2})$$

and a_n and b_n are the magnitude of the n th harmonics of ω , given by

$$a_n = \frac{2}{T_p} \int_{-T_p/2}^{T_p/2} f(t) \cos(n\omega t) dt \quad (\text{A.3})$$

$$b_n = \frac{2}{T_p} \int_{-T_p/2}^{T_p/2} f(t) \sin(n\omega t) dt \quad (\text{A.4})$$

The series may also be written by using exponential notation, which then becomes

$$f(t) = \sum_{-\infty}^{\infty} d_n e^{jn\omega t} \quad (\text{A.5})$$

where

$$d_n = \frac{1}{T_p} \int_{-T_p/2}^{T_p/2} f(t) e^{-jn\omega t} dt \quad (\text{A.6})$$

A.2 Continuous-Time Fourier Transform

The Fourier series approach has to be modified when the waveform is not periodic. An aperiodic waveform can be obtained from the periodic waveform by increasing the period T_p to be infinite [35]. As T_p is increased the spacing between the harmonic components, $1/T_p = \omega/2\pi$, decreases to $d\omega/2\pi$, eventually becoming zero. This corresponds to a change from the discrete frequency $n\omega$ to the continuous frequency ω , and the amplitude and phase spectra become continuous, $d_n \rightarrow d(\omega)$. With these modifications, (A.6) becomes

$$d(\omega) = \frac{1}{T_p} \int_{-\infty}^{\infty} f(t) e^{-j\omega t} dt \quad (\text{A.7})$$

Therefore using the envelope $F(\omega)$ of $T_p d(\omega)$ (A.7) gives

$$F(\omega) = d(\omega) T_p = \int_{-\infty}^{\infty} f(t) e^{-j\omega t} dt \quad (\text{A.8})$$

Equation (A.8) is referred to as the Fourier integral or Fourier transform of $f(t)$.

A.3 Discrete-Time Fourier Transform

In practice the Fourier components of data are usually obtained by digital computation rather than by analog processing [35]. Consider a general

aperiodic sequence $x[n]$ which is of finite duration. That is, for some integer N_1 , $x[n] = 0$ if $|n| > N_1$. From this aperiodic signal we can construct a periodic sequence $\tilde{x}[n]$. $\tilde{x}[n]$ is one period. As we choose the period N to be infinity, $\tilde{x}[n]$ is identical to $x[n]$ for any finite value of n [84].

$$\tilde{x}[n] = \sum_{k=-N/2}^{N/2} a_k e^{jk(2\pi/N)n} \quad (\text{A.9})$$

$$a_k = \frac{1}{N} \sum_{n=-N/2}^{N/2} \tilde{x}[n] e^{-jk(2\pi/N)n} \quad (\text{A.10})$$

Since $x[n] = \tilde{x}[n]$ over a period that includes the interval $|n| \leq N_1$, we can choose the interval of summation in (A.10) to be this, so that $\tilde{x}[n]$ can be replaced by $x[n]$ in the summation. Therefore,

$$a_k = \frac{1}{N} \sum_{n=-N/2}^{N/2} x[n] e^{-jk(2\pi/N)n} \quad (\text{A.11})$$

where we have used the fact that $x[n]$ is zero outside the interval $|n| \leq N_1$.

Defining the envelope $X(\Omega)$ of $N a_k$ as

$$X(\Omega) = \sum_{n=-N/2}^{N/2} x[n] e^{-j\Omega n} \quad (\text{A.12})$$

where Ω is $2\pi k/N$. $X(\Omega)$ is referred to as the discrete-time Fourier transform (DFT) of $x[n]$. The coefficients a_k are given by

$$a_k = \frac{1}{N} X(k\Omega_0) \quad (\text{A.13})$$

where Ω_0 is the sample spacing $2\pi/N$. Thus, the coefficients a_k are proportional to equally spaced samples of this envelope function. Combining (A.9)

and (A.13) and replacing $\tilde{x}[n]$ by $x[n]$ yield

$$x[n] = \sum_{k=-N/2}^{N/2} \frac{1}{N} X(k\Omega_0) e^{jk\Omega_0 n} \quad (\text{A.14})$$

Equation (A.14) is referred to as the inverse discrete-time Fourier transform. An important feature of the DFT is that there is an extremely fast algorithm, called the fast Fourier transform (FFT) [84]. The DFT has computational redundancy. This redundancy can be used to reduce the number of different calculations necessary [35]. The FFT implements this.

Appendix B

The Monte Carlo Method

The Monte Carlo method is named after the city in the Monaco principality, because of a roulette, a simple random number generator.

Enrico Fermi in the 1930's used Monte Carlo in the calculation of neutron diffusion, and later designed the Fermiac, a Monte Carlo mechanical device used in the calculation of criticality in nuclear reactors [53]. The real use of Monte Carlo methods as a research tool stems from work on the atomic bomb during the second world war. A formal foundation for the Monte Carlo method was developed by von Neumann, who established the mathematical basis for probability density functions (PDFs), inverse cumulative distribution functions (CDFs), and pseudorandom number generators [24]. The applications, which arose mostly from the Manhattan Project, included design of shielding for reactors and a direct simulation of the probabilistic problems concerned with random neutron diffusion in fissile material. Around 1948 Fermi, Metropolis, and Ulam obtained Monte Carlo estimates for the eigenvalues of Schrödinger equation. In the late 1950's and 1960's, the method was tested in a variety of engineering fields. Many complex problems remained intractable through the seventies. With the advent of high-speed supercomputers, the field has

received increased attention, particularly with parallel algorithms which have much higher execution rates.

It should be kept in mind though that this general description of Monte Carlo methods may not directly apply to some applications. It is natural to think that Monte Carlo methods are used to simulate random or stochastic processes, since these can be described by PDFs. However, this coupling is actually too restrictive because many Monte Carlo applications have no apparent stochastic content, such as the evaluation of a definite integral or the inversion of a system of linear equations. However, in these cases and others, we can pose the desired solution in terms of PDFs, and while this transformation may seem artificial, this step allows the system to be treated as a stochastic process for the purpose of simulation and hence Monte Carlo methods can be applied to simulate the system.

B.1 Random Variables

The concept of a random variable, a key definition in probability and statistics and for statistical simulations in general, is defined as a real number x that is assigned to an event. It is random because the event is random, and it is variable because the assignment of the value may vary over the real axis. Random variables are useful because they allow the quantification of random processes, and they facilitate numerical manipulations, such as mean and standard deviation.

The probability of getting exactly a specific value in a continuous range

is zero, because there are infinite numbers of values. However, we can talk about the probability of a random variable taking on a value within a given interval. To do this, we define a probability density function, PDF.

B.2 Probability Density Function

The PDF $f(x)$ is the probability that the random variable is in the interval $(x, x + dx)$, given by

$$P(x \leq x' \leq x + dx) = f(x)dx \quad (\text{B.1})$$

Since $f(x)dx$ is unitless, probability, then $f(x)$ has units of inverse random variable units.

We can also determine the probability of finding the random variable somewhere in the finite interval $[a, b]$, given by

$$P(a \leq x \leq b) = \int_a^b f(x')dx' \quad (\text{B.2})$$

which is the area under the curve $f(x)$ from $x = a$ to $x = b$.

Since $f(x)$ is a probability density, it must be positive for all values of the random variable x . The probability of finding the random variable somewhere on the real axis must be unity. These two conditions are the only necessary conditions for $f(x)$ to be an authentic PDF.

$$f(x) \geq 0, \quad -\infty < x < \infty \quad (\text{B.3})$$

$$\int_{-\infty}^{\infty} f(x')dx' = 1 \quad (\text{B.4})$$

By posing a particular application in terms of functions that obey these conditions, one can treat them as PDFs and employ the Monte Carlo simulation to solve the original application.

B.3 Cumulative Distribution Function

Now, we define an important quantity that is known as the cumulative distribution function, CDF. The cumulative distribution function gives the probability that the random number x' is less than or equal to x , and is given by

$$F(x) = \int_{-\infty}^x f(x') dx' \quad (\text{B.5})$$

Since $f(x) \geq 0$, and the integral of $f(x)$ is normalized to unity, $F(x)$ obeys the following conditions.

- $F(x)$ is monotonically increasing
- $F(-\infty) = 0$
- $F(+\infty) = 1$

Since $F(x)$ is the indefinite integral of $f(x)$, $f(x) = F'(x)$.

B.4 Transformation of PDFs

First of all, let us define a new variable $y = y(x)$ to find the PDF $g(y)$ that describes the probability that the random variable y occurs. There must be a 1-to-1 relationship between x and y in order to be able to state that a

given value of x corresponds to a value of y . By definition of the PDFs $f(x)$ and $g(y)$,

$$f(x)dx = P(x \leq x' \leq x + dx) \quad (\text{B.6})$$

$$g(y)dy = P(y \leq y' \leq y + dy) \quad (\text{B.7})$$

The physical transformation implies that these probabilities must be equal. Equality of these differential probabilities yields

$$f(x)dx = g(y)dy \quad (\text{B.8})$$

The fact that $g(y)$ must be positive by definition of probability leads to the following general expression.

$$g(y) = \frac{f(x)}{|dy/dx|} \quad (\text{B.9})$$

One of the most important transformations occurs when $y(x)$ is the cumulative distribution function.

$$y(x) = F(x) \equiv \int_{-\infty}^x f(x')dx' \quad (\text{B.10})$$

In this case, we have $dy/dx = f(x)$, and the PDF for the transformation is given by

$$g(y) = 1, \quad 0 \leq y \leq 1 \quad (\text{B.11})$$

In other words, the CDF is always uniformly distributed on $[0,1]$ independently of the PDF $f(x)$.

B.5 Sampling Using Inversion of the CDF

In 1947 von Neumann suggested a simple but elegant sampling rule in a letter to Ulam [24]. This sampling rule starts from (B.11), which shows the CDF is uniformly distributed on $[0,1]$. Therefore, we simply use a random number generator to generate a sample ξ from the CDF $F(x)$. The value of x is determined by inversion, $x = F^{-1}(\xi)$. It is sometimes called “Golden Rule for Sampling”.

Appendix C

Equivalence / Huygens' Principle

The equivalence principle is a principle by which actual sources, such as an antenna and transmitter, are replaced by equivalent sources [3]. The fictitious sources are said to be equivalent within a region because they produce within that region the same fields as the actual sources.

The equivalence principle is a more rigorous formulation of Huygens' principle, which states that each point on the wavefront of a disturbance can be considered to be a new source of a secondary spherical disturbance, and the wavefront at a later instant can be found by constructing the envelope of the second wavelets [28].

By the equivalence principle, the fields outside an imaginary closed surface are obtained by placing, over the closed surface, suitable electric and magnetic current densities that satisfy the boundary conditions. The current densities are selected to satisfy conditions that the fields inside the closed surface are zero and outside are equal to the radiation produced by the actual sources.

The surface equivalence theorem is based on the uniqueness theorem, which states that [3] “a field in a lossy region is uniquely specified by the

sources within the region plus the tangential components of the electric field over the boundary, or the tangential components of the magnetic field over the boundary, or the former over part of the boundary and the latter over the rest of the boundary.”

An equivalent problem of Figure C.1 a) is shown in Figure C.1 b). The original sources J_1 and M_1 are removed, and we assume that there exist fields E and H inside of S and fields E_1 and H_1 outside of S . For these, they must satisfy the boundary conditions on the tangential electric and magnetic field components. Since the fields E , H within S can be anything, it can be assumed that they are zero. Thus on the imaginary surface S there must exist the equivalent sources [4],

$$J_S = \hat{n} \times (H_1 - H) |_{H=0} = \hat{n} \times H_1 \quad (\text{C.1})$$

$$M_S = -\hat{n} \times (E_1 - E) |_{E=0} = -\hat{n} \times E_1 \quad (\text{C.2})$$

Since the value of the $E = H = 0$ within S cannot be disturbed even if the medium propertied in S are changed, let us assume that it is replaced by free space, ϵ_0 and μ_0 . The replacement of free space makes the problem of Figure C.1 a) a simple radiation problem of the surface equivalent sources in free space.

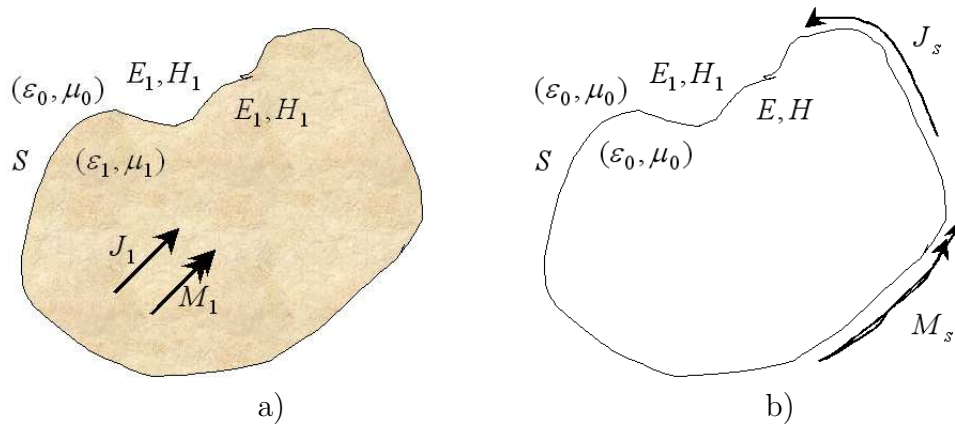


Figure C.1: a) Actual and b) equivalent problem models [4].

Bibliography

- [1] *Department of Defense interface standard*, 1999.
- [2] Y. Ji M. Ali and T. H. Hubing. EMC applications of the EMAP5 hybrid FEM/MOM code. In *Proc. 1998 IEEE International Symposium on Electromagnetic Compatibility*, pages 543–546, Denver, CO, Aug 1998.
- [3] Constantine A. Balanis. *Advanced engineering electromagnetics*. John Wiley & Sons, Inc., New York, 1989.
- [4] Constantine A. Balanis. *Antenna theory: analysis and design*. John Wiley & Sons, Inc., New York, 1997.
- [5] Stephan Barensky. Electric propulsion in space is smart! *Snecma magazine*, pages 20–21, June 1998.
- [6] G. Bekefi. *Radiation Processes In Plasma*. John Wiley & Sons, Inc., New York, 1966.
- [7] G. Bekefi and A. H. Barrett. *Electromagnetic Vibrations, Waves, And Radiation*. The MIT Press, Cambridge, 1977.
- [8] C. K. Birdsall. Particle-In-Cell charged-particles simulations, plus Monte Carlo collisions with neutral atoms, MCC. *IEEE Trans. Plasma Sci.*, 19(2):65–85, April 1991.

- [9] A. M. Bishaev and V. Kim. Local plasma properties in a Hall-current accelerator with an extended acceleration zone. *Sov. Phys. Tech. Phys.*, 23(9):1055–1057, September 1978.
- [10] John Blandino. Electric propulsion. *Aerospace America*, pages 60–61, December 2003.
- [11] L. Garrigues I. D. Boyd J. P. Boeuf. Computation of Hall thruster performance. In *26th International Electric Propulsion Conference*, number IEPC-99-098, Kitakyushu, Japan, October 1999.
- [12] M. Touzeau M. Prioul S. Roche N Gascon C. Perot F. Darnon S. Bechu C. Philippe-Kadlec L. Magne P. Lasgorceix D. Pagnon A. Bouchoule and M. Dudeck. Plasma diagnostic systems for Hall-effect plasma thrusters. *Plasma Phys. Control. Fusion*, 42:B323–B339, 2000.
- [13] J. P. Bouef and L. Garigues. Low frequency oscillations in a stationary plasma thruster. *J. Appl. Phys.*, 84(7):3541–3554, October 1998.
- [14] I. D. Boyd. Hall thruster far field plume modeling and comparison to Express flight data. In *40th AIAA Aerospace Science Meeting & Exhibit*, number AIAA 2002-487, Reno, NV, January 2002.
- [15] S. I. Braginskii. In *Reviews of plasma physics*, volume 1, New York, 1965. Consultants Bureau.
- [16] W. Hreha R. Singh S. L. Liang D. Burr and M. Day. SPT interference assessment in communication satellites. In *22nd International Communi-*

- cations Satellite Systems Conference & Exhibit*, number AIAA 2004-3216, Monterey, California, May 2004.
- [17] F. Taccogna S. Longo M. Capitelli. Very-near-field plume simulation of a stationary plasma thruster. *Eur. Phys. J. Appl. Phys.*, 28:113–122, 2004.
 - [18] S. R. Hunter J. G. Carter and L. G. Christophorou. Low-energy electron drift and scattering in krypton and xenon. *Phys. Rev. A*, 38(11):5539–5551, December 1988.
 - [19] W. A Hargus Jr. C. S. Charles. Near exit plane velocity field of 200W Hall thruster. In *39th AIAA/ASME/SAE/ASEE Joint Propulsion Conference*, number AIAA 2003-5154, Huntsville, Alabama, July 2003.
 - [20] F. F. Chen. *Introduction to Plasma Physics and Controlled Fusion Vol.1: Plasma Physics*. Plenum Press, New York, 1984.
 - [21] E. Y. Choueiri. Plasma oscillations in Hall thruster. *Phys. Plasma*, 8(4):1411–1426, April 2001.
 - [22] V. Latocha L. Garrigues P. Degond and J. P. Boeuf. Numerical simulation of electron transport in the channel region of a stationary plasma thrusters. *Plasma Sources Sci. Technol.*, 11:104–114, 2002.
 - [23] I. D. Boyd R. A. Dressler. Far field modeling of the plasma plume of a Hall thruster. *J. Appl. Phys.*, 92(4):1764–1774, August 2002.

- [24] Roger Eckhardt. Stan Ulam, John Von Neumann, and the Monte Carlo method. Technical Report 15, Los Alamos Science, 1987.
- [25] <http://www.emclab.umn.edu/emap5/>.
- [26] Y. V. Esipchuk and G. N. Tilinin. Drift instability in a Hall-current plasma accelerator. *Sov. Phys. Tech. Phys.*, 21(4):417–423, April 1976.
- [27] Jeff D. Filliben. Electric thruster systems. Technical Report CPTR 97-65, CPIA Technology Reviews, 1997.
- [28] Joseph W. Goodman. *Introduction to Fourier optics*. McGraw-Hill, New York, 1996.
- [29] J. M. Haas and A. D. Gallimore. Considerations on the role of the Hall current in a laboratory-model thruster. *IEEE Trans. Plasma Sci.*, 30(2):687–697, April 2002.
- [30] J. M. Fife W. A. Hargus Jr. D. A. Jaworske C. Sarmiento L. Mason R. Jankovsky J. Haas and A. Gallimore. Spacecraft interaction test results of the high performance Hall system SPT-140. In *36th AIAA/ASME/SAE/ASEE Joint Propulsion Conference*, number AIAA 2000-3521, Huntsville, Alabama, July 2003.
- [31] J. T. Loane J. W. Meyer G. A. Hallock and J. C. Wiley. Analysis of communication signal modulation induced by periodic Hall thruster plume instabilities. In *27th International Electric Propulsion Conference*, number IEPC-01-058, Pasadena, CA, October 2001.

- [32] M. Kim G. A. Hallock and J. C. Wiley. ECE radiation analysis of the Hall thruster. In *45th Annual Meeting of the Division of Plasma Physics*, Albuquerque, NM, October 2003.
- [33] M. A. Heald and C. B. Wharton. *Plasma Diagnostics with Microwaves*. John Wiley & Sons, Inc., New York, 1965.
- [34] M. Ali T. H. Hubing and J. Drewniak. A hybrid FEM/MOM technique for electromagnetic scattering and radiation from dielectric objects with attached wires. *IEEE Trans. Electromagn. Compat.*, EMC-39(4):304–314, November 1997.
- [35] E. C. Ifeachor and B. W. Jervis. *Digital Signal Processing*. John Wiley & Sons, Inc., New York, 1973.
- [36] C. Nickel K. Imre D. F. Register J and S. Trajmar. Total electron scattering cross section: I. He, Ne, Ar, Xe. *J. Phys. B: At. Mol. Phys.*, 18:125–133, 1985.
- [37] D. T. Jacobson and D. H. Manzella. 50 kW class krypton Hall thruster performance. In *39th AIAA/ASME/SAE/ASEE Joint Propulsion Conference*, number AIAA 2003-4550, Huntsville, Alabama, July 2003.
- [38] Robert G. Jahn and Edgar Y. Choueiri. *Encyclopedia of Physical Science and Technology*, volume 5. Academic Press, 3rd edition, 2002.
- [39] Y. Ji and T. Hubing. EMAP5: A 3d hybrid FEM/MOM code. *J. Appl. Computational Electromagn. Society*, 15(1):1–12, March 2000.

- [40] B. E. Beal A. D. Gallimore W. A. Hargus Jr. Preliminary plume characterization of a low-power Hall thruster cluster. In 38th *AIAA/ASME/SAE/ASEE Joint Propulsion Conference*, number AIAA 2002-4251, Indianapolis, IN, July 2002.
- [41] B. E. Beal A. D. Gallimore W. A. Hargus Jr. The effects of cathode configuration on Hall thruster cluster plume properties. In 41th *AIAA/ASME/SAE/ASEE Joint Propulsion Conference*, number AIAA 2005-3678, Tucson, AZ, July 2005.
- [42] S. Oleson I. Katz. Electric propulsion for project Prometheus. In 39th *AIAA/ASME/SAE/ASEE Joint Propulsion Conference*, number AIAA 2003-5279, Huntsville, Alabama, July 2003.
- [43] E. J. Beiting J. E. Pollard V. Khayms and L. Werthman. Electromagnetic emissions to 60Ghz from a BPT-4000 EMD Hall thruster. In 28th *International Electric Propulsion Conference*, number IEPC-03-129, Toulouse, France, March 2003.
- [44] M. A. Lieberman and A. J. Lichtenberg. *Principle of Plasma Discharges and Materials Processing*. John Wiley & Sons, Inc., New York, 1994.
- [45] V Vahedi G Dipeso C K Birdsall M A Lieberman and T D Rognlien. Capacitive RF discharges modelled by paricle-in-cell Monte Carlo simulation. i: analysis of numerical techniques. *Plasma Source Sci. Technol.*, 2:261–272, 1993.

- [46] G. A. Hallock J. C. Wiley A. Khanna E. A. Spencer J. W. Meyer J. T. Loane. Impact analysis of Hall thruster on satellite communication. *J. Spacecraft and Rockets*, 39(1):115–124, January 2002.
- [47] K. D. Paulsen D. R. Lynch and J. W. Strohbehn. Three-dimensional finite, boundary, and hybrid element solutions of the Maxwells equations for lossy dielectric media. *IEEE Trans. on Microwave Theory and Tech.*, 36(4):682–693, April 1988.
- [48] H. C. Kim O. Manuilenko and J. K. Lee. Particle-In-Cell Monte-Carlo simulation of capacitive RF discharges: Comparison with experimental data. *Japanese J. Appl. Phys.*, 44(4A):1957–1958, 2005.
- [49] M. Martinez-Sanchez and J. E. Pollard. Spacecraft electric propulsion – an overview. *J. Propulsion Power*, 14(5):688–699, September-October 1998.
- [50] S. Y. Cheng M. Martinez-Sanchez. Simulations for a shuttle-based Hall thruster plume experiment. In *27th International Electric Propulsion Conference*, number IEPC-01-054, Pasadena, CA, October 2001.
- [51] Lee S. Mason and Steven R. Oleson. Spacecraft impacts with advanced power and electric propulsion. Technical Report NASA/TM-2000-209912, NASA Technical Memorandum, 2000.
- [52] R. P. McEachran and A. D. Stauffer. Relative low-energy elastic and momentum transfer cross section for electron scattering from xenon. *J.*

- Phys. B: At. Mol. Phys.*, 20:3483–3486, 1988.
- [53] N Metropolis. The beginning of the Monte Carlo method. Technical Report 15, Los Alamos Science, 1987.
 - [54] M. Mitchner and C. H. Kruger. *Partially Ionized Gases*. John Wiley & Sons, Inc., New York, 1973.
 - [55] A. I. Morozov and V. V. Savelyev. Fundamentals of stationary plasma thruster theory. In *Reviews of plasma physics*, volume 21, New York, 2000. Consultants Bureau.
 - [56] A. I. Morozov and L. S. Solov’ev. Steady-state plasma flow in a magnetic field. In *Reviews of plasma physics*, volume 8, New York, 1980. Consultants Bureau.
 - [57] A. I. Morozov Y. V. Esipchuk A. M. Kapulkin V. A. Nevrovskii and V. A. Smirnov. Effect of the magnetic field on a closed-electron-drift accelerator. *Sov. Phys. Tech. Phys.*, 17(3):482–487, September 1972.
 - [58] W. K. H. Panofsky and M. Phillips. *Classical Electricity and Magnetism*. Addison-Wesley Publishing Company, Inc., Cambridge, MA, 1955.
 - [59] M. Celik M. Santi S. Y. Cheng M. Martinez-Sanchez J. Peraire. Hybrid-PIC simulation of a Hall thruster plume on an unstructured grid with dsmc collisions. In *28th International Electric Propulsion Conference*, number IEPC-03-134, Toulouse, France, March 2003.

- [60] R. R. Hofer P. Y. Peterson and A. D. Gallimore. A high specific impulse two-stage Hall thruster with plasma lens focusing. In *27th International Electric Propulsion Conference*, number IEPC-01-036, Pasadena, CA, October 2001.
- [61] N. Sitnikova D. Volkov I. Maximov V. Petrusevich and D. Allen. Hall effect thruster interactions data from the Russian Express-A2 and Express-A3 satellites. Technical Report NASA/CR-2003-212005, NASA Contractor Report, 2003.
- [62] http://commons.wikipedia.org/wiki/Image:SNECMA_PPS_1350_Ion_Rocket_engine.jpg.
- [63] Von C. Ramsauer. Über den wirkungsquerschnitt der gasmoleküle gegenüber langsamen elektronen. ii. fortsetzung und schluß. *Ann. Phys.*, 72:345–352, 1923.
- [64] Von C. Ramsauer and R. Kollath. Über den wirkungsquerschnitt der edelgas-moleküle gegenüber elektronen unterhalb 1 volt. *Ann. Phys.*, 3:536–564, 1929.
- [65] S. Roy and B. P. Pandey. Numerical investigation of a Hall thruster plasma. *Phys. Plasma*, 9(9):4052–4060, September 2002.
- [66] D. Manzella C. Sarmiento J. Sankovic and T. Haag. Performance evaluation of the SPT-140. Technical Report NASA/TM-97-206301, NASA Technical Memorandum, 1997.

- [67] I V Schweigert V A Schweigert. Combined PIC-MCC approach for fast simulation of a radio frequency discharge at a low gas pressure. *Plasma Source Sci. Technol.*, 12:315–320, 2004.
- [68] S.Galitsky. Electric propulsion in Russia. *News from Moscow*, (26):9–13, 2000.
- [69] A. I. Morozov Y. V. Esipchuk G. N. Tilinin A. V. Trofimov Y. A. Sharov and G. A. Shchepkin. Plasma accelerator with closed electron drift and extended acceleration zone. *Sov. Phys. Tech. Phys.*, 17(1):38–45, July 1972.
- [70] T. Koizumi E. Shiragawa and I. Ogawa. Momentum transfer cross section for low-energy electrons in krypton xenon from characteristic energies. *J. Phys. B: At. Mol. Phys.*, 19:2331–2342, 1986.
- [71] L. T. Sinfailam. Relativistic effects in electron scattering by atoms iii. elastic scattering by krypton, xenon and radon. *J. Phys. B: At. Mol. Phys.*, 15:119–142, 1982.
- [72] M. S. Dababneh W. E. Kauppila J. P. Downing F. Larerrier V. Pol J. H. Smart and T. S. Stein. Measurements of total scattering cross sections for low-energy positrons and electrons colliding with krypton and xenon. *Phys. Rev. A*, 22(5):1872–1877, November 1980.
- [73] M. S. Dababneh Y. F. Hsieh W. E. Kauppila V. Pol J. H. Smart and T. S. Stein. Total-scattering cross-section measurements for intermediate-

- energy positrons and electrons colliding with Kr and Xe. *Phys. Rev. A*, 26(3):1252–1259, September 1982.
- [74] <http://www.esa.int/esaMI/SMART-1/>.
- [75] <http://encyclopedia.thefreedictionary.com>.
- [76] G. N. Tilinin. High-frequency plasma waves in a hall accelerator with an extended acceleration zone. *Sov. Phys. Tech. Phys.*, 22(8):974–978, August 1977.
- [77] Y. V. Esipchuk A. I. Morozov G. N. Tilinin and A. V. Trofimov. Plasma oscillations in closed-drift accelerators with an extended acceleration zone. *Sov. Phys. Tech. Phys.*, 18(7):928–932, January 1974.
- [78] W. H. Press S. A. Teukolsky W. T. Vetterling and B. P. Flannery. *Numerical Recipes in C*. Cambridge University press, Cambridge, MA, 1992.
- [79] D. F. Register L. Vuskovic and S. Trajmar. Elastic electron scattering cross section for xe in the 1-1000 eV impact energy region. *J. Phys. B: At. Mol. Phys.*, 19:1685–1697, 1986.
- [80] R. W. Wagenaar and F. J. de Heer. Total cross section for electron scattering from Ar, Kr and Xe. *J. Phys. B: At. Mol. Phys.*, 18:2021–2036, 1985.
- [81] M. Xu H. Wang and T. H. Hubing. Application of the cavity model to lossy power-return plane structures in printed circuit boards. *IEEE Trans. Adv. Packag.*, 26(1):73–80, February 2003.

- [82] G. D. Racca G. P. Whitcomb and B. H. Foing. The SMART-1 mission. *ESA Bulletin*, 95:72–81, August 1998.
- [83] G. A. Hallock J. C. Wiley and E. A. Spencer. Development and application of the beamserver code for plume impact analysis on satellite communication. In *37th AIAA/ASME/SAE/ASEE Joint Propulsion Conference*, number AIAA 2001-3354, Salt Lake City, UT, July 2001.
- [84] A. V. Oppenheim A. S. Willsky and S. Hamid. *Signals and Systems 2ed*. Prentice-Hall, Englewood Cliffs, N.J., 1997.
- [85] M. Xu and T. H. Hubing. The development of a closed-form expression for the input impedance of power-return plane structures. *IEEE Trans. Electromagn. Compat.*, 45(3):478–485, August 2003.
- [86] T. Hubing Y. Ji and H. Wang. Techniques for optimizing FEM/MOM codes. In *Proc. 16th Annual Review of Progress in Applied Computational Electromagnetics*, pages 444–451, Monterey, CA, March 2000.
- [87] D. Manzella J. Yim and I. Boyd. Predicting Hall thruster operational lifetime. In *40th AIAA/ASME/SAE/ASEE Joint Propulsion Conference*, number AIAA 2004-3953, Fort Lauderdale, Florida, July 2004.
- [88] X. Yuan. Three-dimensional electromagnetic scattering from inhomogeneous objects by the hybrid moment and finite element method. *IEEE Trans. on Microwave Theory and Tech.*, 38(4):1053–1058, August 1990.

Vita

Minkyu Kim was born in Seoul, Korea in 1971. He received his Bachelor of Science degree from Chung-Ang University, Seoul, Korea, in 1994 and his Master of Science degree from Seoul National University, Seoul, Korea, in 1997, both in electrical engineering. He was with Samsung Electronics from 1997 to 2002, and worked in the areas of processing plasmas, plasma physics, and motor & robot control systems. He started Ph.D. studies at the University of Texas, Austin, TX in 2002 and received his Ph.D degree in 2007. Then he joined ASML.

His research interests include plasma physics, processing plasmas, streamer analysis, optics, micro lithography and electromagnetic waves and also include control, motor design & analysis and electromagnetics.

Permanent address: 11160 Jollyville Rd #1402
Austin, Texas 78759

This dissertation was typeset with L^AT_EX[†] by the author.

[†]L^AT_EX is a document preparation system developed by Leslie Lamport as a special version of Donald Knuth's T_EX Program.